Magnetic Particle Imaging Modeling and Solving a Dynamic Inverse Problem

Dissertation with the aim of achieving a doctoral degree at the Faculty of Mathematics, Informatics and Natural Sciences

Department of Mathematics
of Universität Hamburg

submitted by

Christiane Schmidt

Hamburg
2022

Accepted as dissertation by the Department of Mathematics of Universität Hamburg based on the evaluations by:

Prof. Dr. Christina Brandt (Universität Hamburg)
Prof. Dr.-Ing. Tobias Knopp (Hamburg University of Technology)

Date of the oral defense: October 26th, 2022

Abstract

Magnetic particle imaging (MPI) is a functional, tracer-based medical imaging technique, which measures the non-linear response of magnetic nanoparticles to a dynamic magnetic field. The visualization of tracer dynamics with high temporal resolution is of particular interest in many applications, e.g. cardiovascular interventions or blood flow measurements.

While MPI offers a very high spatial and temporal resolution, the size of its field-of-view is limited by physiological constraints. Multi-patch scans, sequentially scanning smaller subvolumes, so-called patches, allow to increase the total field-of-view. The forward operator, or system matrix, required for image reconstruction can be determined by calibration scans or physical models. Neither measured system matrices nor the standard forward models in MPI account for changes in the tracer concentration during a single scanning cycle. As a result, to date, non-periodic dynamic tracer distributions are mostly reconstructed as a time-series of frames under the assumption of nearly static behavior during the scan of each frame. While being a feasible approach for limited velocities, the reduced temporal resolution and data gaps in multi-patch sequences and the ignorance of dynamics in the forward operators cause motion and displacement artifacts in the case of strong dynamics.

In this thesis, we introduce a reconstruction method for dynamic tracer distributions based on a dynamic forward model and a spline representation of the concentration. First, we present the dynamic MPI model and analyze its influence on the measurements and reconstructions with and without noise compared to the static model. Second, we establish the dynamic reconstruction approach for non-periodic motion in multi-patch sequences. Third, the new method is evaluated on the basis of synthetic single- and multi-patch data showing that the dynamic model enables for the reconstruction of fast tracer dynamics from a few

frames and the spline approach approximates the missing data, which reduces multi-patch artifacts. Even in the absence of a specific motion model, a reduction of motion and multi-patch artifacts for fast dynamic tracer distributions is achieved.

Kurzfassung

Magnetic Particle Imaging (MPI) ist ein funktionelles bildgebendes Verfahren in der Medizin, das auf einem Kontrastmittel aus magnetischen Nanopartikeln beruht. Das gemessene Signal entsteht durch das nicht-lineare Verhalten der Nanopartikel in Gegenwart eines dynamischen Magetfeldes. Eine zeitlich hochaufgelöste bildliche Darstellung der Kontrastmittelverteilung ist für viele Anwendungen von großem Interesse, z.B. bei Blutflussmessungen oder kardiovaskulären Eingriffen.
MPI weist zwar eine sehr hohe räumliche und zeitliche Auflösung aufweist, jedoch ist die Größe des abtastbaren Bereichs durch physiologisch bedingte Grenzwerte limitiert. Eine Vergrößerung dieses Bereichs kann durch Multi-Patch Scans, bei denen nacheinander kleinere Teilvolumina, sogenannte Patches, gescannt werden, erzielt werden. Für die Bildrekonstruktion wird in der Regel ein Vorwärtsoperator oder eine Systemmatrix benötigt. Diese kann durch Kalibrierungsmessungen oder physikalische Modelle bestimmt werden. Allerdings werden Bewegungen während der Messung weder von gemessenen Systemmatrizen noch vom Standardmodell für MPI berücksichtigt. Daher werden dynamische Kontrastmittelverteilungen momentan hauptsächlich in Form von Zeitreihen einzelner Bilder rekonstruiert, wobei ein statisches Verhalten während der Messung jedes Bildes angenommen wird. Ist dieser Ansatz für geringe Geschwindigkeiten akzeptabel, so führen sowohl die veringerte zeitliche Auflösung und Datenlücken bei Multi-Patch Messungen als auch die Vernachlässigung der Bewegung im Vorwärtsoperator zu Bewegungs- und Verschiebungsartefakten im Fall von schnellen Konzentrationsänderungen.
In dieser Arbeit geht es um eine neue Rekonstruktionsmethode für dynamische Kontrastmittelverteilungen, die auf einem dynamischen Vorwärtsmodell und einer Spline-Repräsentation der Partikelkonzentration basiert. Zunächst stellen wir das dynamische MPI-Modell vor und analysieren dessen Einfluss auf Messungen und

Rekonstruktionen mit und ohne Rauschen im Vergleich zum statischen Modell. Danach wird die dynamische Rekonstruktionsmethode für nicht-periodische Bewegungen in Multi-Patch Sequenzen eingeführt. Mit Hilfe synthetischer Single- und Multi-Patch Daten wird gezeigt, dass durch das dynamische Modell eine Rekonstruktion schneller Bewegungen aus wenigen Scanzyklen möglich wird. Darüber hinaus werden die fehlenden Daten in Multi-Patch Scans durch den Spline-Ansatz approximiert, wodurch Verschiebungsartefakte reduziert werden. Auch ohne ein spezifisches Bewegungsmodell wird eine Reduzierung von Bewegungs- und Multi-Patch Artefakten für schnelle dynamische Kontrastmittelverteilungen erreicht.

Danksagung

Zuallererst geht mein Dank an Christina Brandt. Danke für die Chance zu promovieren und dass ich deine erste Doktorandin sein durfte. Du warst immer da, für Rat, die Organisation von Reisen und Unterhaltung. Du hast dich stets gut um deine wachsende Arbeitsgruppe gekümmert und dich für uns eingesetzt.
Danke an meinen Panel Chair Tobias Knopp für die Begutachtung der Dissertation, wertvollen Input im Laufe der Jahre und die Nutzung der Ressourcen des IBI. Dank geht in dem Zusammenhang auch an Patryk und Marija für die freundliche Unterstützung bei der Beschaffung von Messdaten.
Außerdem vielen Dank an Armin Iske, für die Integration unserer Arbeitsgruppe und dass du auch immer mit Rat und Tat zur Stelle warst.
Danke an meine Familie, die mir meine Ausbildung ermöglicht und mich während meiner diversen Umzüge unterstützt hat.
Besonderer Dank geht an Lena, Stephanie und Tram für das Korrekturlesen meiner Dissertation und die nicht zu unterschätzende emotionale Unterstützung! Darüber hinaus bin ich sehr dankbar für all die unterhaltsamen Stunden mit euch, den anderen Kollegen und dem Student Chapter beim Mittagessen, unzähligen Kaffeepausen, Lockdown-Skype-Runden, Klausurkorrekturen und allen sonstigen Aktivitäten.
Und zu guter Letzt ein großes Dankeschön an meine Freunde! Ihr habt an mich geglaubt und mich mit euren Erfahrungen, Optimismus, Zuhören und ganz viel Ablenkung in allen Phasen unterstützt!

Contents

1. Introduction

Non-invasive medical imaging has become an integral part of modern medicine. From the discovery of X-rays by Wilhelm C. Röntgen in 1895 to the invention of modern tomographic imaging methods like computed tomography (CT) by Allan M. Cormack and Godfrey N. Hounsfield in the 1970s, medical imaging has continued to develop significantly to this day. The number of imaging diagnostics performed in German hospitals was increasing every year until the beginning of the Covid-19 pandemic in 2020 (see Figure 1.1a). In 2019 alone, 13,703,689 imaging procedures were applied in German hospitals. Technologies like CT, magnetic resonance imaging (MRI), ultrasound, single-photon emission computed tomography (SPECT), positron emission tomography (PET) or classic X-ray cover a broad range of diagnostic purposes and are used up to 6.56 million times per year (see Figure 1.1b) [74]. Each of them has its advantages and disadvantages. Features like resolution, sensitivity, speed, cost, usability and amount of radiation decide whether, how often and under which indications it can be applied. Hence, they determine the range of patients in which it can be used for therapeutic or diagnostic purposes.

To further expand the possibilities of medical imaging, new modalities are still being developed. Magnetic particle imaging (MPI) is a rather young technology which was invented by Jürgen Weizenecker and Bernhard Gleich in 2005 [28]. Like SPECT and PET, MPI is tracer-based, meaning that the measured signal stems from the tracer material. The tracer can be injected into the blood stream or target organs of interest. The identification of the tracer distribution (over time) allows to visualize physiological processes. While SPECT and PET detect radioactive decay events, MPI is non-ionizing. Its tracer material consists of magnetic nanoparticles (MNPs) that are exposed to dynamic magnetic fields. As with MRI, magnetic fields are not harmful to the human organism within certain

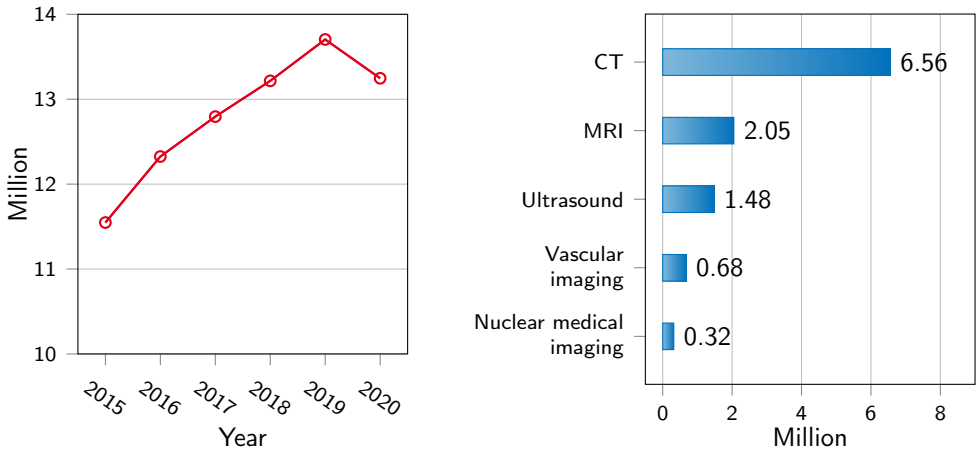

(a) Diagnostic medical imaging (b) Selection of frequently applied modalities in 2019

Figure 1.1.: Numbers of inpatient medical imaging procedures in German hospitals [74].

limits. MPI takes the non-ionizing property of MRI and the functional imaging property of PET and SPECT together with a high spatial and temporal resolution. This makes MPI a very attractive method for real-time imaging of highly dynamic processes.

Although magnetic particle imaging is still in a preclinical state, its potential applications are numerous. Examples are physiological diagnostics like acute stroke detection [55], blood flow measurements [43], visualization of blood flow [87] or localization of medical instruments in vascular interventions [37]. Given that cardiovascular diseases were the leading cause of death in Germany in 2020 [75], MPI has enormous potential to meet the need for fast, safe and precise diagnostic tools.

Image reconstruction usually states an ill-posed inverse problem. Novel imaging methods require finding suitable optimization and regularization techniques. To date, the standard method for static MPI reconstruction is the Kaczmarz method with Tikhonov regularization [50, 87]. Especially for functional imaging, reconstruction of dynamic tracer distributions is of high interest. Measurements from dynamic concentrations can be considered a time-series of measurements that

can be reconstructed with static methods. Alternatively, more complex methods taking the dynamics during the measurement into account have been developed. Having already been investigated for other imaging modalities, dynamic image reconstruction has now become a research direction for MPI as well. In dynamic image reconstruction the ill-posedness becomes more severe due to the increased degrees of freedom. For that reason, the existing approaches to dynamic MPI reconstruction focus on special cases like periodic motion [25], limited velocities or rigid motion [23].

In this thesis, we investigate possibilities to improve image reconstruction of dynamic tracer distributions in magnetic particle imaging. First, we introduce a general model that allows to represent measurements from dynamic tracer distributions. Second, we examine the data structure of dynamic multi-patch MPI sequences and third, we combine these findings to develop a new dynamic reconstruction method for dynamic MPI measurements with arbitrary motion.
In Chapter 2, we give an introduction into the basics of inverse problems and dynamic inverse problems which provide the theoretical basis for the reconstruction problems later in this work.
Chapter 3 summarizes the basic theory of magnetic particle imaging beginning with the physics of signal generation in Section 3.1, continuing with standard methods for image reconstruction in Section 3.2 and presenting a selection of special measurement setups which are relevant for this thesis in Section 3.3.
Chapter 4 deals with MPI forward models. In Sections 4.1 and 4.2, we present forward models for dynamic tracer distributions. The new models show an additional second term compared to the standard model. In Section 4.3, we examine the influence of the second term on the signal.
In Chapter 5, a novel reconstruction method for dynamic concentrations based on the dynamic model and spline curves is introduced. Beginning with a discussion of the challenges of reconstructing multi-patch data in Section 5.1, a suitable concentration model is presented in Section 5.2, followed by basics of spline theory in Section 5.3 and suitable configurations for dynamic concentration models in Section 5.4.
The reconstruction method is evaluated on phantoms of different levels of com-

plexity in Chapter 6. We used computational phantoms with very simple spatial setups in Section 6.1 to further investigate the influence of the second term in the dynamic model as well as the influence of noise on the reconstructions. In Section 6.2, more complex computational phantoms are studied to evaluate the reconstruction quality of the dynamic reconstruction method compared to Kaczmarz reconstructions. We close with a conclusion and discussion of the results in Chapter 7.

2. Inverse Problems

The term *inverse problem* refers to a mathematical or scientific problem. It describes the task of deducing the cause of an observed impact. It is the opposite of a direct or *forward problem* where the impact of a cause is determined.
Inverse problems appear frequently in various fields of science and industry where system parameters cannot be observed directly. Applications range from seismic imaging and astronomy to machine learning tasks like classification or natural language processing as well as all kinds of tomographic imaging including non-destructive testing and medical applications. A classic example is computed tomography. A CT image depicts attenuation coefficients which vary for different organs or materials. In order to get an image of a slice of the human body, the slice is exposed to X-rays from a set of angles. A detector measures the attenuated radiation for each angle. These measurements are called sinogram. Deducing the attenuation coefficients on the inside of the slice from the sinogram corresponds to solving an inverse problem [17].
There are ill-posed and well-posed inverse problems, whereas the majority is ill-posed, meaning that a solution might not exist, is not unique or that the solution is very sensitive to measurement noise. Thus, ill-posed problems are usually not trivial to solve and require methods, such as regularization, tailored to the specific problem in order to achieve a stable solution.
We will get into the basic theory of inverse problems in Section 2.1. In contrast to static inverse problems that have been researched extensively, *dynamic inverse problems* have not been covered deeply in the literature until today. This topic will be discussed in Section 2.2.

2.1. Fundamentals of Inverse Problems

This section deals with basic theory of inverse problems which will be used in the remainder of this work. For further details we refer to [66]. Section 2.1.1 introduces the most relevant terms while Section 2.1.2 presents solution strategies for (ill-posed) inverse problems.

2.1.1. Definition and Properties

We start with the mathematical description of an inverse problem.

Definition 2.1 (Inverse Problem)**.** *Given two Hilbert spaces X and Y, let $A : X \to Y$ be a continuous map between the two spaces. Considering X the space of parameters (causes) and Y the space of observable data (impacts), computing data*

$$y = Ax$$

*from given parameters $x \in X$ is called a **forward problem**. Determining a parameter $x \in X$ from given data $y \in Y$ with*

$$Ax = y$$

*is called **inverse problem** with **forward operator** A.*

For many practical inverse problems it is quite challenging to determine a unique parameter x solving $Ax = y$, e.g. if the measuring system is highly sensitive to noise. A categorization of inverse problems into ill- and well-posed problems was introduced by Hadamard in 1932.

Definition 2.2 (Ill-posedness [35]). *Let a map $A : X \to Y$ between two normed spaces X and Y. The problem (A, X, Y) is called* ***well-posed*** *if the following conditions are fulfilled:*

1. *(Existence) For every $y \in Y$ exists a solution $x \in X$, such that $Ax = y$.*
2. *(Uniqueness) The solution $x \in X$ is unique.*
3. *(Stability) The inverse map $A^{-1} : Y \to X$ is continuous, i.e. the solution x depends continuously on the data y.*

If one of the three conditions is not fulfilled, the problem is called ***ill-posed****.*

A unique solution can be determined with the help of the normal equation and the Moore-Penrose inverse.

Theorem 2.3 (Normal Equation). *Let $y \in Y$ and A a continuous linear map between X and Y and P an orthogonal projection, the following statements are equivalent.*

1. *$x \in X$ fulfills $Ax = P_{\overline{\mathrm{ran}(A)}} y$.*
2. *$x \in X$ minimizes the residuum: $\|Ax - y\|_Y \leq \|A\varphi - y\|_Y$ for all $\varphi \in X$.*
3. *$x \in X$ solves the* ***normal equation*** *$A^*Ax = A^*y$.*

A proof is provided in Appendix A. The set of solutions to the normal equation is denoted by $\mathbb{L}(y) = \{x \in X \mid A^*Ax = A^*y\}$.

Definition 2.4 (Moore-Penrose-Inverse)**.** *Let* $A^+ : \mathrm{dom}(A^+) \subset Y \to X$ *with* $\mathrm{dom}(A^+) = \mathrm{ran}(A) \oplus \mathrm{ran}(A)^\perp$ *be a map of every* $x \in \mathrm{dom}(A^+)$ *to a unique* x^+ *being the element of minimal norm of* $\mathbb{L}(y)$*.* A^+ *is then called* ***Moore-Penrose-Inverse*** *of* A*. Element* $x^+ = A^+ y$ *is the* ***Minimum-Norm-Solution*** *of* $Ax = y$*.*

After defining an ill-posed inverse problem and a unique solution the next section will present the theory to find such a solution.

2.1.2. Solution Strategies

Most ill-posed problems violate the stability condition in Definition 2.2, such that a measurement sequence $\lim_{n\to\infty} y_n \to y$ does not necessarily imply $\lim_{n\to\infty} x_n \to x$. Furthermore, in practice, measurement data y^ε is usually corrupted by noise, i.e. $\|y - y^\varepsilon\|_Y \leq \varepsilon$.
An ill-posed problem cannot be solved directly via the inverse operator, as small perturbations in the measurement data might imply large errors in the reconstructed data. Regularization methods allow to overcome this problem and find an approximation to the minimum norm solution based on noisy data.

Definition 2.5 (Regularization)**.** *Let* A *a continuous linear map between* X *and* Y *and* $\{\mathcal{R}_t\}_{t>0}$ *a family of continuous maps from* Y *to* X *with* $\mathcal{R}_t 0 = 0$*. Given a map* $\gamma : (0,\infty) \times Y \to (0,\infty)$ *with*

$$\sup\left\{\|A^+ y - \mathcal{R}_{\gamma(\varepsilon,y^\varepsilon)} y^\varepsilon\|_X \mid y^\varepsilon \in Y,\ \|y - y^\varepsilon\|_Y \leq \varepsilon\right\} \to 0 \quad \text{for } \varepsilon \to 0\,,$$

for all $y \in \mathrm{ran}(A)$*,* $(\{\mathcal{R}_t\}_{t>0}, \gamma)$ *is called* ***regularization (method)*** *for* A^+ *with* ***regularization parameter*** $\gamma := \gamma(\varepsilon, y^\varepsilon)$*.*

One of the most common methods is *Tikhonov regularization.*

Definition 2.6 (Tikhonov regularization)**.** *Given a regularization parameter $\gamma > 0$, a Banach space Z and an map $B : X \mapsto Z$ which is continuously invertible on* $\mathrm{ran}(B)$*, the regularized normal equation*

$$(A^*A + \gamma B^*B)x = A^*y$$

has a unique solution $x_\gamma \in X$ which depends continuously on the measurement $y \in Y$. The solution is also the minimizer of the Tikhonov functional

$$J_{\gamma,y}(x) = \underbrace{\|Ax - y\|_Y^2}_{\text{fidelity}} + \gamma \underbrace{\|Bx\|_Z^2}_{\text{regularization}} . \tag{2.1}$$

(cf. Theorem A.1 for a proof). The functional consists of a fidelity term which punishes deviations from the measurement and a regularization term which allows to incorporate prior knowledge about the solution and penalize deviations from features like sparcity, limited curvature etc.

The Tikhonov functional can be minimized with any suitable optimization algorithm depending on the chosen norms. Possible algorithms are gradient descent, newton or quasi-newton method, conjugate gradient descent, stochastic gradient descent, proximal gradient methods or the Kaczmarz algorithm which will be presented in Section 3.2. The two terms of the functional can also be stacked to achieve the following simpler least squares form

$$J_{\gamma,y}(x) = \left\| \underbrace{\begin{pmatrix} A \\ \sqrt{\gamma}B \end{pmatrix}}_{=\tilde{A}} x - \underbrace{\begin{pmatrix} y \\ 0 \end{pmatrix}}_{=\tilde{y}} \right\|^2 = \|\tilde{A}x - \tilde{y}\|^2 . \tag{2.2}$$

Using an iterative method to solve the normal equation, the maximum iteration number forms a regularization parameter, as well [66]. The functional B and the spaces X and Y need to be chosen according to the given problem. Another aspect of solving inverse problems is the determination of an optimal regularization parameter that minimizes the reconstruction error. The reconstruction error of

$\mathcal{R}_\gamma$ can be decomposed into approximation and data error

$$\underbrace{\|A^+ y - \mathcal{R}_\gamma y^\varepsilon\|_X}_{\text{reconstruction error}} \leq \underbrace{\|A^+ y - \mathcal{R}_\gamma y\|_X}_{\text{approximation error}} + \underbrace{\|\mathcal{R}_\gamma (y - y^\varepsilon)\|_X}_{\text{data error}} .$$

The two errors behave in opposite ways in the limits of γ, meaning that the regularization parameter decides whether the solution fits closer to the measured data or the regularization condition. In order to find the optimal parameter for minimizing the reconstruction error, the two errors have to be balanced. There are different methods to determine the regularization parameter for a given problem, like L-curve or discrepancy principle [66]. In practice however they are not always feasible e.g. because they require many evaluations of the target function which might be too expensive. As a result, the regularization parameter is sometimes determined by visual inspection.

2.2. Dynamic Inverse Problems

While there is a broad range of literature about solving static inverse problems in various applications, Schmitt and Louis were one of the first introducing dynamic inverse problems in 2002 [69]. They considered inverse problems where the measured object evolves over time during the measurement process which are specified in the following definition.

Definition 2.7 (Dynamic inverse problem)**.** *Given two Hilbert spaces X and Y and discrete time sampling points $(t_i)_{i=1}^{n_T} \in [0, T]$, let $A_i := A(t_i, \cdot) : X \to Y$ be a continuous map between the two spaces. Determining a parameter $x_i := x(t_i, \cdot) \in X$ from given data $y_i := y(t_i, \cdot) \in Y$ with*

$$A_i x_i = y_i \tag{2.3}$$

*for all time points t_i is called **dynamic inverse problem**.*

The forward operator A does not necessarily depend on time, while in some applications it may be intrinsically time dependent, e.g. in MPI which will be

introduced in Chapter 3.
Dynamic inverse problems can be found in many imaging applications. Most functional imaging methods like PET, SPECT and MPI can be considered dynamic inverse problems since their signal stems from liquid tracer materials that can move through the blood stream, accumulate or decay. Furthermore, there is also 4D-CT and the effects caused by motion during the measurement process. In a medical context, these motion artifacts mainly originate from respiratory or cardiac motion.
Additionally to the fact, that image reconstruction in these modalities is already an ill-posed inverse problem, measurements of a spatiotemporal image will usually be strongly under-sampled. Therefore, the reconstruction of a dynamic image from a time-series of measurements is an ill-posed problem. Time discrete setups obviously allow for independent reconstructions of each time step. However, prior knowledge about the image or the underlying motion can improve image quality and computation costs. Thus, proper descriptions of the dynamics are an important aspect of dynamic reconstruction approaches. A literature overview on dynamic inverse problems from 2018 can be found in [72]. Furthermore, there is a survey on variational methods for image reconstruction in dynamic inverse problems from 2021 [39]. The authors classify solution strategies for dynamic inverse problems into reconstruction methods without explicit temporal models, methods with motion models, methods based on deformable templates and data driven approaches based on machine learning.
Solving a time continuous dynamic inverse problem

$$A\left(t, x(t,\cdot)\right) = y(t,\cdot) \qquad \text{for } T \in [0,T], \tag{2.4}$$

with continous map $A(t,\cdot) : X \to Y$, $x(t,\cdot) \in X$ and $y(t,\cdot) \in Y$, without known temporal model that connects data and images requires regularization. One approach is minimizing

$$\int_0^T L\left(A(t,x(t,\cdot)), y(t,\cdot)\right) + \gamma_s \mathcal{R}_s\left(x(t,\cdot)\right) + \gamma_t \mathcal{R}_t\left(\partial_t x(t,\cdot)\right) \mathrm{d}t$$

with respect to x, with L being a data fidelity term, $\mathcal{R}_s$ being a spatial regular-

ization, $\mathcal{R}_t$ being a temporal regularization and γ_s and γ_t the respective regularization parameters. While for the spatial regularization there is a broad range of literature usually chosen as some energy functional, like the L^2 or L^1 norm of the spatial gradient, there is much less theory on proper temporal regularization methods. Simple penalties on the temporal variation like

$$\mathcal{R}_t(\partial_t x_i) = \frac{\|x_{i+1} - x_i\|^2}{(t_{i+1} - t_i)^2}$$

were proposed by Schmitt and Louis, but might damp dynamics to much. They become aware of the computational difficulties due to the high number of degrees of freedom and develop algorithms based on the Kronecker product but without a temporal model [69, 70]. Other approaches use sparsifying transforms. In [15], an image time series is reconstructed from sparse non-periodic dynamic CT data. The ill-posedness due to the sparsity of the data and the underlying motion is regularized with 3D shearlets, an extension of wavelets, that describe 2D images over time. Gravier et al. deal with the reconstruction of time activity curves from gated cardiac SPECT data [33]. The dynamic tracer distribution is modeled with cubic spline curves, an idea which we pick up in Section 5.1. Also the authors of [18] aim to reconstruct time activity curves from dynamic SPECT measurements. Infimal convolution of Bregman distances is used to enforce alignment of edges in sequential frames, while they do not use a temporal model but a sparse concentration representation. Methods without known temporal model can be applied to a broad range of problems, but their solution remains a challenge. Thus, for dynamic inverse problems whose underlying motion can be modeled, solution strategies will often benefit from incorporating this prior knowledge.
If there is the option to model the temporal evolution of the ground truth one can expand (2.4) to

$$\begin{aligned} A\left(t, x(t,\cdot)\right) &= y(t,\cdot) \\ \text{s.t. } \Psi(t, x(t,\cdot)) &= 0 \end{aligned}$$

with $\Psi : [0,T] \times X \to X$ being a motion model for x. If Ψ depends only on a time dependent parameter, it will probably be easier to solve, reducing the

degrees of freedom and acting as a regularization. Usually an additional spatial regularization will be necessary nevertheless. An example of a motion model with high relevance in dynamic image reconstruction is the optical flow constraint

$$\frac{\partial x}{\partial t} + \nabla x^\top v = 0$$

with velocity field v, which promotes constancy of brightness in consecutive image frames. The dynamic image is often reconstructed jointly with its velocity field. E.g. Burger et al. reconstruct an image time series from sparse dynamic CT data using a joint image and motion reconstruction method based on optical flow [16]. Another approach is the dynamic reconstruction based on deformable templates. Similar to the preceding idea, the dynamics in an image are modeled as deformations of initial image x_0 at time point t such that (2.4) changes to solving

$$A\left(t, \Phi(\lambda_t, x_0)\right) = (t, \cdot)$$

for $x_0 \in X$ and temporally dependent parameter λ_t. Also in this case additional spatial and temporal regularizers might be required. For discrete problems the theory of image registration can be applied such that the deformation parameters for each time step are reconstructed jointly with the initial template. An example for dynamic, template-based reconstruction can be found in [38]. The author reconstructs static images from dynamic CT measurements by motion estimation based on estimating contour deformations and motion compensating filtered back projection. Blanke et al. interpret dynamic inverse problems as problems with inexact forward operators and develop a motion compensation approach based on sequential subspace optimization and the Kaczmarz algorithm [7]. While the temporal evolution is initially modeled with deformable templates, their method does not explicitly compute deformation fields.

Since solving dynamic inverse problems turns out to be so challenging due to the enormous degrees of freedom, a potential non-convexity of the problem and high computation costs, a natural step is to use the nowadays ubiquitous learning methods. Methods like deep learning are quite flexible, can be applied to problems which are difficult to model and after the training phase are rather cheap to apply. Without an explicit temporal model, data driven methods can be used

to determine a post processing operator, applied to a reconstruction operator e.g. based on a known forward model. If a suitable motion model is available learning methods can be used to speed up the reconstruction process e.g. by learning motion fields from given time series $x(t, \cdot)$. Data driven methods can be used to determine the temporal evolution of a deformation parameter or to learn the class of deformations. Also regularizations for the deformation can be estimated.
In the context of medical imaging another problem arises. Supervised learning methods require a vast amount of training data. Medical data sets are rare as they are strongly protected and not publicly available. This makes setting up reliable machine learning systems in this field very challenging.
The referenced articles emphasize the progress that has been made in the research field of dynamic inverse problems. Nevertheless, depending on the chosen application the setups are varying, e.g. signal-to-noise ratio (SNR), the data structure or the time dependence of the forward operators, such that a general solution approach does not exist. We will continue with an introduction to magnetic particle imaging physics and modeling. An overview of recent articles on dynamic inverse problems in MPI will be given Section 3.3.

3. Magnetic Particle Imaging

Magnetic particle imaging is a tracer-based medical imaging modality for physiological examinations. The measured signal is generated by the magnetic tracer material (Figure 3.1a). Hence, there is no signal from surrounding organs. To add

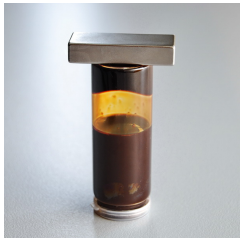

(a) Magnetic nanoparticles [71]

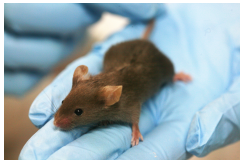

(b) Lab mouse [65]

(c) Preclinical MPI scanner at the University Medical Center Hamburg-Eppendorf (UKE) [58]

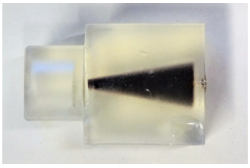

(d) Cone-shaped phantom filled with tracer material [58]

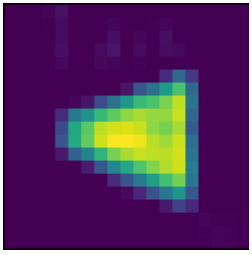

(e) Reconstruction of the cone phantom [58]

Figure 3.1.: Currently magnetic particle imaging allows to visualize the multidimensional distribution of magnetic nanoparticles on the inside of phantoms or small animals.

morphological context, MPI images can be combined with CT or MRI images. Its high spatial and temporal resolution make MPI a very attractive method for

real-time imaging of highly dynamic processes.
To date, MPI is in the preclinical research phase and the scanner size is still limited. Thus, its field of application is currently limited to examinations of test objects, so called phantoms, tissue or small animals like mice (Figure 3.1b). While scaling the standard setup to human size remains a challenge [62], there is a human-sized MPI brain imager [32]. Nevertheless, approval for clinical applications is still pending. Figure 3.1c shows the preclinical MPI scanner (Bruker, Ettlingen, Germany) at the University Medical Center Hamburg-Eppendorf. Reconstructed MPI images visualize the particle concentration of the tracer in space (and time). An example phantom, a 3D printed cone-shaped phantom filled with magnetic nanoparticles, is depicted in Figure 3.1d. The respective reconstruction from the openMPI data set [58] can bee seen in Figure 3.1e.
Although MPI has not entered the clinical research phase yet, its potential applications are numerous, e.g. targeted imaging of tumor cells [82], imaging of instruments during interventions [36, 37] and vascular examinations. This includes imaging of stenosis [83], aneurysms [73], internal bleeding [88], brain perfusion [32], stroke detection [55] and blood flow measurements [43]. Another promising application is interventional MPI. Magnetic fields are used to steer catheters [2, 64] or to heat targeted tissue in hyperthermia therapy [5, 59]. An extensive overview on the range of applications can be found in [49].
In the remainder of this chapter we will explain the basic physics of magnetic particle imaging, the mathematics of image reconstruction in MPI and a few measurement setups which are relevant for the remaining chapters.

3.1. Signal Generation

Magnetic particle imaging being tracer-based means that the measured signal is generated by the tracer material and not by applied radiation or the object under consideration. The non-linear magnetization response of magnetic particles exposed to a dynamic magnetic field induces a current in the receive coils of the MPI scanner. Specific excitation fields allow to map the measured voltages to the multi-dimensional tracer distribution. The physical and technical fundamentals of the signal generation and acquisition are explained in the following sections.

3.1.1. Magnetic Particles

The tracer material in MPI is required to be sensitive to dynamic magnetic fields, liquid and safe for medical use. In 2002, Schering introduced an MRI contrast agent for liver diagnostics, called Resovist, containing superparamagnetic iron oxide nanoparticles (SPIONs) that was used in the first MPI experiments [21, 28]. The magnetic nanoparticles (MNPs) consist of a magnetic iron oxide core and a sufficiently thick coating to prevent agglomeration of particles. Furthermore, they are superparamagnetic, meaning that while an external magnetic field is applied, they behave like tiny magnets with each particle having its own magnetic moment which is larger than the atomic moment. After the applied magnetic field is removed, there is no remanent magnetization [6].
The particles' diameter in the nanometer range facilitates their use as a tracer which can be injected into a living organism. Due to their size, a single particle cannot be located but the concentration of the particles within a volume can be detected and visualized.

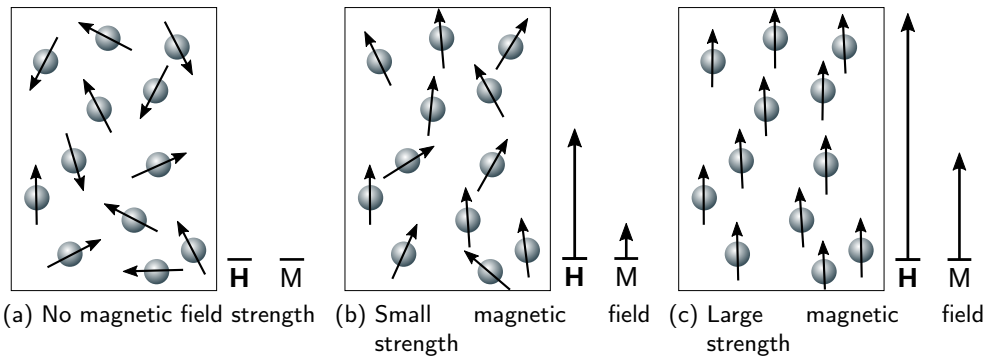

Figure 3.2.: Superparamagnetic nanoparticles in a magnetic field. With increasing field strength $\mathbf{H} := \|H\|$ the magnetic moments of more particles align with the applied magnetic field. As a result the magnetization M within the depicted volume increases.

The magnetic moments of superparamagnetic particles point in random directions when there is no external magnetic field applied, see Figure 3.2a. Depending

on the magnetic field strength, a higher fraction of particles will align with the direction of an external magnetic field. As a result the magnetization of the volume of particles will increase. This behavior is illustrated in Figure 3.2.
The exact behavior of the SPIONs can be described by different magnetization models. A simple and popular model is the Langevin or equilibrium model. The Langevin function

$$\mathcal{L}_{\alpha,\beta}(z) = \alpha \coth(\alpha\beta z) - \frac{1}{\beta z} \qquad \text{with } \alpha = M_c V_c,\ \beta = (k_B T_0)^{-1}$$

describes the magnetization as a function of the magnetic field strength z and

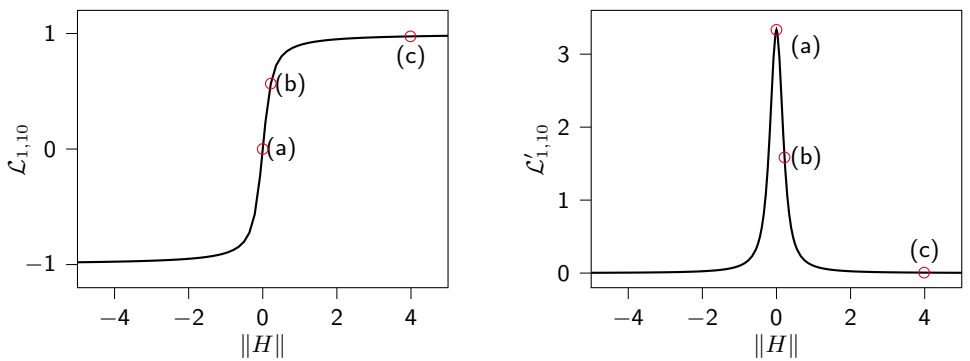

(a) Function (b) Derivative

Figure 3.3.: The Langevin model for the magnetization of a paramagnetic particle. Red circles mark the magnetization states shown in Figure 3.2.

particle dependent parameters α and β. While α is determined by th product of the saturation magnetization of the core material M_c and the core volume V_c, β depends inversely on the Boltzmann constant k_B and temperature T_0. The Langevin function and its derivative are shown in Figure 3.3 for exemplary values of α and β. The three magnetization states from Figure 3.2 are also marked in Figure 3.3. A nonlinear behavior of the magnetization can be observed. The magnetization change is strongest for small field strengths and saturates for large ones. The mean magnetic moment for a given tracer material in a magnetic field

H at position r and time point t

$$\bar{m}(r,t) = \mathcal{L}_{\alpha,\beta}\big(\|H(r,t)\|\big)\frac{H(r,t)}{\|H(r,t)\|} \tag{3.1}$$

is described by a vector in the direction of the magnetic field and with the length proportional to the value of the Langevin function for the magnetic field strength. Thus, the product of the mean magnetic moment and the particle concentration c yields the magnitude of the magnetization

$$M(r,t) = c(r)\bar{m}(r,t)\,. \tag{3.2}$$

The Langevin model assumes that the particles are in thermal equilibrium and the applied magnetic fields are static. This strong simplification and the negligence of magnetic relaxation effects give rise to modeling errors. Therefore, more complex models were studied by Kluth [47] and Weizenecker [85]. In [44], magnetization models for single domain particles, i.e. particles so small that their magnetic domain is composed of a single domain, with uniaxial anisotropy are presented. The article covers two types of relaxation. A magnetic nanoparticle can change the direction of its magnetic moment by an internal rotation, called Néel relaxation, or the rotation of the whole particle, called Brownian rotation. The authors of [47] discovered that their models are able to model the correct relaxation behavior of the particles much better than the equilibrium model. Nevertheless, the Langevin model is used throughout this work due to its simplicity, while incorporating the more advanced model into the approaches presented in this work seems practicable and might be realized in the future.

3.1.2. Spatial Signal Encoding

Spatiotemporal encoding of the signal is of high importance in each imaging modality. It enables us to decode the spatial origin of the signal from a measured time signal and thus links measurements and positions.
An MPI scanner has several coils to generate dynamic magnetic fields. The number of coils and shape of the magnetic fields depend on the scanner type. We start with the description of a scanner with ideal magnetic fields. MPI signal

generation is realized by the spatiotemporally inhomogeneous magnetic field

$$H(r,t) = H_S(r) + H_D(t) \qquad \in L^2(\Omega \times \mathbb{R}^+, \mathbb{R}^3)\,.$$

It is an overlay of the static linear gradient field H_S, named selection field, and the dynamic drive field H_D. The field-of-view (FOV) is denoted by $\Omega \subset \mathbb{R}^3$. The selection field is inhomogeneous in space and has a region of vanishing field strength. The shape of this region depends on the scanner setup. There are field-free line (FFL) and field-free point (FFP) scanners. In this work we restrict ourselves to the more common FFP scanner. The selection field

$$H_S(r) = \begin{pmatrix} g_x & 0 & 0 \\ 0 & g_y & 0 \\ 0 & 0 & g_z \end{pmatrix} r, \qquad r \in \Omega \subset \mathbb{R}^3\,,$$

with g_x, g_y, $g_z \in \mathbb{R}$ is zero at $r = [0,0,0]^\top$ and increases linearly to the periphery which can be seen in Figure 3.4a. According to the equilibrium model, the magnetization of particles is sensitive to low magnetic field strengths and saturated at high field strength. Thus, if the FFP moves to a new position, the field strength at the new position drops and the particle magnetization changes rapidly, which induces a voltage in a measurement coil. Such a shift of the FFP can be achieved by adding another magnetic field, the drive field. The setup of this field depends on the intended FFP trajectory. A common choice is the Lissajous trajectory (see Figure 3.4b). The drive field

$$H_D(t) = \begin{pmatrix} a_x \sin(2\pi f_x t + \varphi_x) \\ a_y \sin(2\pi f_y t + \varphi_y) \\ a_z \sin(2\pi f_z t + \varphi_z) \end{pmatrix},$$

of this trajectory is a temporally sinusoidal 3-dimensional field and has three parameters per dimension. The amplitudes a_x, a_y, $a_z \in \mathbb{R}$ determine the size of the covered area, the frequencies f_x, f_y, $f_z \in \mathbb{R}$ define the density and the phase shifts φ_x, φ_y, $\varphi_z \in \mathbb{R}$ set the starting point of the scan trajectory.
Adding the two fields and choosing the parameters appropriately, the FFP is

traveling through the volume on a grid-like closed curve which can bee seen in Figure 3.4b.

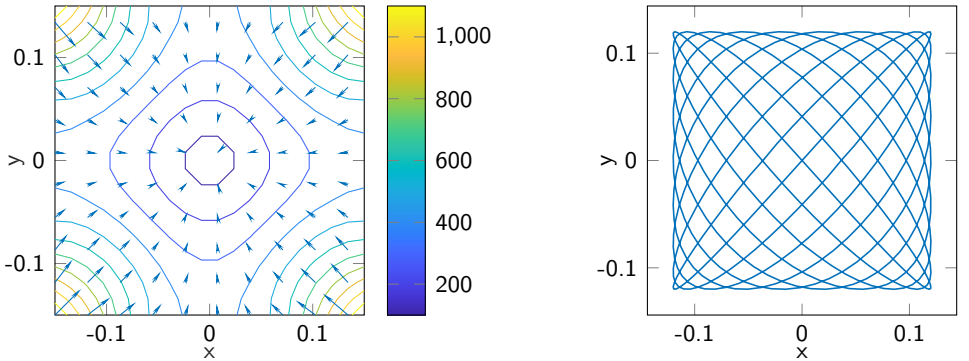

(a) The selection field H_s is a static gradient field with vanishing field strength in the center and linearly increasing field strength to the border of the field of view.

(b) The trajectory of the field-free point forms a Lissajous curve during a single excitation cycle.

Figure 3.4.: Magnetic field setup of an FFP scanner

Additionally to the particle signal that is needed for the reconstruction, the dynamic excitation field also induces a voltage that is dominating the measurement. Fortunately, the parameters of the excitation field are known such that its contribution to the signal can be removed with a bandstop filter.
The setup presented in this section, i.e. FFP scanner with Lissajous trajectory, is the most common scanner setup so far. Nevertheless, there are alternative trajectories e.g. cartesian trajectory for FFP scanners or rotations for the FFL scanner setup. The latter provides Radon data which enables the use of extensive CT-reconstruction theory. In practice however, problems arise as magnetic fields are not ideal but are distorted versions of the ones presented above. As a result, the FFP and FFL are not perfect circles and lines but ellipses and banana-shaped. Spherical harmonics allow to describe ideal magnetic fields with a small set of coefficients [13]. With the help of calibration scans non-ideal fields can be approximated and incorporated in reconstruction schemes [14]. Also the filtering of the measured signal is not perfect in practice and noise is part of every physical

measuring system. However, under the condition that the modeling errors are tolerable, a measured voltage at a certain time can be connected to the particle concentration at a certain location. This process is called image reconstruction and the topic of the following section.

3.2. Image Reconstruction

Image reconstruction requires suitable forward operators, i.e. knowledge of how the measured data is linked to the image to be reconstructed, and reconstruction algorithms. In MPI, reconstruction methods can be classified into model- and measurement-based techniques [34]. In the measurement-based approach, the forward operator, which describes the mapping between the object and the measurement, is determined in a calibration scan [63, 86]. The FOV is subdivided into a finite grid and the signal for a delta sample is measured at each node, which is very time-consuming. For a 3D scan with 64^3 voxels the calibration time takes about three days [34]. While this is the main drawback of this approach, the calibration includes the transfer function of the system. This function provides a mathematical description of (analog) components of the receive chain such as impedance matching, band-stop filters and preamplifiers [48], and may also include system-specific noise and imperfections. Unfortunately, the scan needs to be repeated if settings like resolution, tracer material etc. change. The efficiency and flexibility of the measurement-based approach can be improved with machine learning techniques. The forward operator can be generated from a few sampling points and adapted for different tracer material with the help of deep learning [3]. In the model-based approach particle physics and the measurement process are modeled by physical laws [51] as described in the previous section. While the modeling approach is more flexible to parameter changes, it remains a challenge to balance modeling errors and simplicity of the models allowing for efficient computations. This is an ongoing topic of research and the still large amount of modeling errors are a reason why the measurement-approach still prevails in practice.

3.2.1. Direct MPI Problem

This work deals with model-based reconstruction. The standard model for the direct MPI problem is based on Faraday's law of induction

$$\hat{u}(k) = a_k \cdot \mathcal{F}\Big(-\mu_0 \frac{\mathrm{d}}{\mathrm{d}t} \int_\Omega p_s(r)^\top \big(c(r)\bar{m}(r,t) + H(r,t)\big)\,\mathrm{d}r^3\Big) \tag{3.3}$$

for each frequency component k [48]. It describes the measurement process in frequency space for static tracer distributions. The continuous Fourier transform is denoted by $\mathcal{F} : L^2(\mathbb{R}) \mapsto L^2(\mathbb{R})$, μ_0 is the permeability constant and $p_s : \mathbb{R}^3 \mapsto \mathbb{R}^3$ the sensitivity of the receive coils. A band-stop filter a_k filters the signal to separate the signal generated by the excitation field H from the one originating from the tracer material. Assuming a_k to be a perfect filter the problem can be reformulated to

$$\hat{u}(k) = \int_\Omega \underbrace{-\mu_0\, p_s(r)^\top \mathcal{F}\Big(\frac{\partial \bar{m}}{\partial t}(r,t)\Big)}_{=:\hat{S}(r,k)} c(r)\,\mathrm{d}r^3 \tag{3.4}$$

where $\hat{S}$ is called system function in Fourier domain. As defined in Section 3.1.2 the excitation field is multi-dimensional such that the system function $\hat{S}$ maps to $\mathbb{C}^3$ and $\hat{u} \in \mathbb{C}^3$ is a voltage vector, where each value is measured by a respective receive coil. To simplify the mathematical description in the following, we will refer to a single receive channel while the computations are analogous for all channels.

Discretization Numerical reconstruction methods require discretized models and data. In order to discretize forward problem (3.4), we use a basis $\{\phi_i\}_{i=1,\dots,R} \subset L^2$ of a finite-dimensional subspace $X_R \subset L^2$ and choose piecewise constant basis functions on equisized, pairwise disjoint quadratic or cubic domains. This is a common choice since the basis functions can be interpreted as the pixels or voxels in an image as well as the delta sample used for the calibration scans at different positions in space.
Using the basis functions, we obtain piecewise constant approximations of the

concentration and system function by

$$\tilde{c}(r) = \sum_{i=1}^{R} c_i \phi_i(r) \quad \text{and} \quad \tilde{S}(r,k) = \sum_{i=1}^{R} \hat{S}_{k,i} \phi_i(r) \quad \in X_R \,.$$

Inserting $\tilde{c}$ in (3.4) yields the following discrete forward problem

$$\hat{u}(k) = \sum_{i=1}^{R} \hat{S}_{k,i} c_i \,. \tag{3.5}$$

It can also be written as a matrix vector multiplication of a concentration vector $\mathbf{c}$ and the system matrix $\hat{\mathbf{S}}$

$$\hat{\mathbf{u}} = \hat{\mathbf{S}}\mathbf{c} \quad \text{with } \hat{\mathbf{u}} \in \mathbb{R}^{n_K},\ \hat{\mathbf{S}} \in \mathbb{R}^{n_K \times R},\ \mathbf{c} \in \mathbb{R}^{R}\,, \tag{3.6}$$

with n_K denoting the total number of frequencies. Reconstructing the concentration vector $\mathbf{c}$ from the given measurement vector $\hat{\mathbf{u}}$ is a classic inverse problem.

3.2.2. Inverse MPI Problem

Image reconstruction in MPI means to solve (3.4) for the particle distribution c. It was shown in [46, 57] that the multidimensional MPI reconstruction problem is severely ill-posed. As discussed in Section 2.1.2, there a numerous regularization techniques that can be used to solve such problems. Solving (3.4) can be written as a variational least-squares problem

$$\arg\min_{c \geq 0} \frac{1}{2} \left\| \int_{\Omega} \hat{S}(r,k) c(r) \, \mathrm{d}r - \hat{u}(k) \right\|_2^2 + \gamma \mathcal{R}(c) \,. \tag{3.7}$$

Using the L^2-norm is a typical choice since the measurement noise is Gaussian [76]. In general, image reconstruction problem (3.7) can be solved with many optimization methods. One of the most common reconstruction algorithms in MPI is the Karzmarcz algorithm with Tikhonov regularization [87].

Kaczmarz Reconstruction The Kaczmarz algorithm is an iterative solver proposed in 1937 by Stefan Kaczmarz [42], also known as algebraic reconstruction technique (ART). The Kaczmarz method was used in the first computed tomography reconstructions since it models the discrete CT imaging process quite intuitively [17]. Later it was replaced, in practice, by the filtered back projection due to computational advantages.
The linear system (3.6) has n_K equations and R unknowns. The idea is to start off with a starting value $c^{(0)}$, approximate a voltage $u^{(0)} = Sc^{(0)}$, compute the error to the true measurement u correct the current estimate to obtain $c^{(1)}$ and repeat. This is realized by dividing the R dimensional solution space into n_K hyperplanes, one for each equation. In a sub-iteration, the current estimate $c^{(q)}$ is projected onto the hyperplane defined by the k-th equation. Each sub-iteration

$$c^{(q+1)} = c^{(q)} + \frac{u_k - \langle \bar{s}_k \, , c^{(q)} \rangle}{\|s_k\|_2^2} \bar{s}_k, \qquad q = 1, \ldots, q_{\max} \, ,$$

requires only one matrix row s_k. One sweep through all matrix rows is called one Kaczmarz iteration. It is advantageous if successive rows are nearly orthogonal but in general any sequence of rows can be used e.g. $k = (q \mod n_K) + 1$ or a random order [77]. If the algorithm is not run until convergence, the parameter $q_{\max}$ is a regularization parameter [45]. Further regularization can be added by using ℓ^2-Tikhonov regularization, cf. Equation (2.2). An additional improvement of the convergence and reconstruction quality of the Kaczmarz algorithm can be achieved by adding a diagonal weighting matrix that normalizes the matrix rows with their squared reciprocal energy [50].

Advanced Reconstruction Methods Although the Kaczmarz method is still dominating MPI reconstruction in practice, several alternatives or extensions have been developed in the last years. The ℓ^2-Tikhonov regularization leads to oversmooth edges in the reconstructed images. Regularizers allowing for sharp edges require alternative optimization techniques. Storath et al. propose a reconstruction method called non-negative fused lasso that includes ℓ^1-regularization combined with a total variation penalty and a non-negativity constraint on the concentration c. The inverse problem is solved with a forward-backward scheme

which results in reconstructions with reduced noise while edges are preserved [76]. More approaches using ℓ^1-regularization combined with total variation penalty can be found e.g. in [41] for FFL scanners, in [56] for FFP scanners, both based on the alternating direction method of multipliers or in [54] using an adaptation called non-negative garrote (NNG) thresholding.
Zdun et al. also replace the ℓ^2-regularization used in the regularized Kaczmarz method by non-smooth priors. They propose a stochastic primal-dual hybrid gradient method combined with a data-driven splitting scheme that allow a wider choice of regularizers and data fidelity terms. Additionally, the runtime of their method is absolutely competitive with the Kaczmarz method [89].
Recently, another fast reconstruction method for MPI was proposed by Droigk et al. [20]. They exploit the similarity of the system function to tensor products of Chebychev polynomials of the second kind to create a direct reconstruction method for multi-dimensional MPI. While the reconstruction quality was comparable to model-based Kaczmarz reconstructions, they could show a significant reduction of the runtime for measured 2D phantoms.
There is a variety of other methods that incorporate prior knowledge from other imaging modalities [4], consider ℓ^1-fidelity terms [45] or approaches with different structures like representing the solution by a deep neural network [19] or x-space reconstruction, a direct inversion method for cartesian trajectories [30, 31]. We refer to [49] for an overview.

3.3. Special Measurement Setups

The physics and mathematics described in the preceding sections allow to understand the principles of MPI and how images can be generated from measurements. As discussed there are many assumptions and limitations in the theory. Some applications require settings that remain a technical and theoretical challenge. Two of them, multi-patch and dynamic imaging, which are highly relevant for this work, are presented in the following.

3.3.1. Multi-Patch Measurements

The volume of the field-of-view

$$V_{\mathrm{FOV}} = \frac{2a_x}{g_x}\frac{2a_y}{g_y}\frac{2a_z}{g_z},$$

which is covered by the drive field, depends on the quotients of the drive field amplitudes and the gradient strengths. While magnetism is generally considered to be harmless, there is a risk of tissue heating or peripheral nerve stimulation (PNS) for dynamic magnetic fields. In order to prevent these negative side effects, there are safety limits on the drive field amplitudes which consequently limit the size of the FOV [10, 67, 68]. Considering typical gradient strengths of $[-1, -1, 2]$ $\mathrm{Tm}^{-1}\mu_0^{-1}$, a drive field strength of 5 $\mathrm{mT}\mu_0^{-1}$ results in a FOV of $10 \times 10 \times 5$ mm^3, which is too small for many applications.

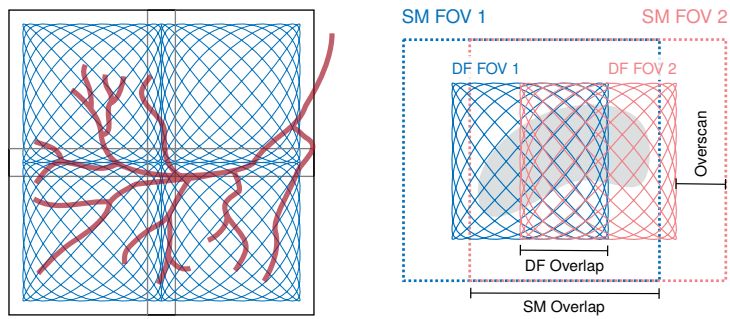

(a) A large vessel can be scanned using a setup with four patches

(b) Illustration of the the terms drive field FOV, system matrix FOV, overscan and overlap

Figure 3.5.: Large objects can be scanned by using multiple patches. The FOVs of the patches might overlap.

One approach to cover a larger volume, is to move the object of interest step-wise through the FOV [78], while the more common method shifts the FOV by low frequency focus fields [29]. The focus field can be shifted continuously [61] or step-wise in between excitation cycles [53]. In the latter case, the total scan-

ning volume is subdivided into several smaller FOVs, called patches, which are scanned sequentially. This scanning routine is called multi-patch scan and an example setup is shown in Figure 3.5a. The figure illustrates how a large vessel tree can be covered by four patches.
In this example, the drive field FOVs do not overlap. The rectangular area covered by the trajectory is called drive field field-of-view (DF FOV). MPI scanners are sensitive to signals slightly off the DF FOV such that particles located outside the region of interest or in neighboring patches generate a signal that cannot be mapped to the correct location. For single patches, these artifacts can be handled by using an overscan, meaning to choose a larger field-of-view for the system matrix (SF FOV) than for the drive field [84]. The larger SM FOV can also be observed in the example setup in Figure 3.5a. Depending on the location of multiple patches, the SM FOVs and DF FOVs might overlap. The terms SM FOV, DF FOV, SM overlap, DF overlap and overscan are illustrated in Figure 3.5b. For multiple patches, overscans can be used as well, but redundant information due to the SM overlap need to be taken into account. An example can be found in [1]. The authors reconstruct overlapping patches and use the redundant data in a post-processing step to compensate the artifacts occurring at the respective edges. An example for a DF overlap can be found in [25].
Another challenge is the distortion of the magnetic fields which becomes stronger with the distance from the center of the scanner. Consequently, a measurement-based multi-patch reconstruction requires more calibration scans. The authors of [53] present a joint reconstruction method for static measurement-based multi-patch sequences, where a dedicated system matrix is used for each patch. Measuring and storing several system matrices causes a long calibration time and high memory consumption. A performance upgrade is made by Szwargulski et al. by using shifted versions of the same central system matrix for all patches at the cost of artifacts for non-ideal magnetic fields [81]. The authors of [80] and [9] compromise between these two approaches by either exploiting symmetries and generating neighboring system matrices by mirroring in the former case and by using the same system matrices for clusters of patches based on an error metric depending on the magnetic fields in the latter case. Boberg et al. discovered another method which reuses calibration measurements from the center and warps

them according to the patch location thus saving time for additional calibration scans [8].

3.3.2. Dynamic Measurements

A common challenge in many imaging modalities is motion during the measurement process. Section 2.2 gives an overview of dynamic inverse problems. One of the main fields of application of MPI is physiological diagnostics. The MNPs form a liquid tracer which flows through the patient's body, spreading, accumulating or dissipating according to the processes in the body. Thus, the dynamics of the tracer concentration over time are of high diagnostic value. Further typical sources of dynamics are cardiac and respiratory motion.
The MPI theory we have discussed so far assumes (quasi) static tracer distributions during signal acquisition. Regardless of whether we consider measurement- or model-based reconstruction, the presented methods are not designed to account for tracer dynamics. The concentration c in (3.3) depends only on the spatial variable r and the delta probe is static during each cycle of the calibration scan. Image sequences of objects with slow dynamics can be generated by reconstructing a time-series of MPI scans with the methods known from static reconstruction. This is intuitive and due to the speed of MPI a realistic approach which was used in [37, 76]. In the last years, dynamic reconstruction has gained more interest in MPI research. In [26], motion in single-patch MPI measurements is detected and compensated for the special case of periodic motion. The authors assume a limited velocity and group the measured data into virtual frames to reconstruct images with the measurement-based approach. An extension to multi-patch sequences is presented in [25]. Ehrhardt et al. deal with dynamic non-periodic multi-patch reconstruction. They use polyrigid image registration for joint reconstruction of the object and its motion to compensate e.g. respiratory motion [23]. A more general approach for dynamic non-periodic MPI reconstruction for single and multiple patches is the topic of Chapter 5.

4. Forward Models for Dynamic Tracer Distributions

In the preceding chapter we presented the standard MPI forward problem and discussed its shortcomings when it comes to the reconstruction of dynamic tracer distributions. We begin with incorporating dynamic behavior in the forward model in Section 4.1, extend it to multi-patch MPI in Section 4.2 and continue with studying the components and their influence on the measurement in Section 4.3. The models from Section 4.2 have already been published in [11] as well as parts of the analyses in Section 4.3. The models from Section 4.2 have been introduced in [12].

4.1. Dynamic Single-Patch Models

Independently of the explicit magnetization model, the magnetization function (3.2) is modified such that it contains a time-dependent concentration

$$M(r,t) = c(r,t)\bar{m}(r,t)\,, \qquad c \in H^1(\Omega \times \mathbb{R}^+), \quad M, \bar{m} \in H^1(\Omega \times \mathbb{R}^+)\,. \tag{4.1}$$

This changes the model (3.3) to

$$u(t) = -\mu_0 \frac{\mathrm{d}}{\mathrm{d}t} \int_\Omega p_s(r)^\top \big(c(r,t)\bar{m}(r,t) + H(r,t)\big)\,\mathrm{d}r\,.$$

We assume that the signal generated by the excitation field is removed by a filter and that the coil sensitivity p_s is constant such that it can be summarized in $\eta := -\mu_0 p_s \in \mathbb{R}$ together with the permeability constant. This yields the dynamic forward model

$$u(t) = \eta \frac{\mathrm{d}}{\mathrm{d}t} \int_\Omega c(r,t)\bar{m}(r,t)\,\mathrm{d}r \tag{4.2}$$

$$= \eta \int_\Omega \underbrace{\frac{\partial \bar{m}}{\partial t}(r,t)}_{=:S_1(r,t)} c(r,t) + \underbrace{\bar{m}(r,t)}_{=:S_2(r,t)} \frac{\partial c}{\partial t}(r,t)\,\mathrm{d}r\,, \tag{4.3}$$

Dynamic model

$$u(t) = \eta \int_\Omega S_1(r,t)c(r,t) + S_2(r,t)\frac{\partial c}{\partial t}(r,t)\,\mathrm{d}r\,, \tag{4.4}$$

$$c, S_2 \in H^1(\Omega \times \mathbb{R}^+)\,,$$

describing a measurement $u : \mathbb{R}^+ \mapsto \mathbb{R}^3$ in time domain. It contains a sum of two system functions $S_1, S_2 : \Omega \times \mathbb{R}^+ \mapsto \mathbb{R}^3$ multiplied with the tracer concentration $c : \Omega \times \mathbb{R}^+ \mapsto \mathbb{R}^+$ and its time derivative. Since the concentration c and $S_2 = \bar{m}$ are in the Sobolev space $H^1(\Omega \times \mathbb{R}^+)$, the derivatives $\frac{\partial c}{\partial t}$, $S_1 = \frac{\partial \bar{m}}{\partial t}$ and the measurement u are L^2-functions.

Dynamic forward model in frequency domain In practice, MPI measurements are either measured in or transferred to frequency domain for preprocessing steps like frequency selection or spectral leakage correction. The freqency domain model

$$\hat{u}(k) = \eta \int_\Omega c(r)\mathcal{F}\Big\{\frac{\partial \bar{m}}{\partial t}\Big\}(r,k)\,\mathrm{d}r$$

corresponding to (3.3) changes to

$$\hat{u}(k) = \eta \int_\Omega \mathcal{F}\{c\}(r,k) * \mathcal{F}\Big\{\frac{\partial \bar{m}}{\partial t}\Big\}(r,k) + \mathcal{F}\Big\{\frac{\partial c}{\partial t}\Big\}(r,k) * \mathcal{F}\{\bar{m}\}(r,k)\,\mathrm{d}r\,, \tag{4.5}$$

Dynamic model in frequency domain

$$\hat{u}(k) = \eta \int_\Omega \hat{c}(r,k) * \hat{S}_1(r,k) + \widehat{\frac{\partial c}{\partial t}}(r,k) * \hat{S}_2(r,k)\,\mathrm{d}r\,, \qquad (4.6)$$
$$\hat{c}\,, \hat{S}_2 \in H^1(\Omega \times \mathbb{R}^+)\,.$$

The measurement in frequency space $\hat{u} : \mathbb{R}^+ \mapsto \mathbb{C}^3$ and the derivatives $\widehat{\frac{\partial c}{\partial t}} : \Omega \times \mathbb{R}^+ \mapsto \mathbb{C}$, $\hat{S}_1 : \Omega \times \mathbb{R}^+ \mapsto \mathbb{C}^3$ are L^2-functions because $\hat{c}\,, \hat{S}_2 \in H^1(\Omega \times \mathbb{R}^+)$. Due to the time dependence of the concentration, the dynamic forward model in frequency domain contains convolutions which are only applied to the frequency components.

Discretization The dynamic model can be discretized analogously to the static model with the pixel-basis $\{\phi_i\}_{i=1,\dots,R} \subset L^2$ used in Section 3.2.1. We get the representation

$$\tilde{c}(r,t) = \sum_{i=1}^{R} c_i(t)\phi_i(r) \qquad \in X_R$$

of a piecewise constant dynamic concentration and the derivative $\frac{\partial c}{\partial t}$ and system functions S_1 and S_2 analogously. Using these function and the time sampling points $\{t_j\}_{j=1,\dots,n_T}$ from Section 3.2.1, yields the discretized dynamic forward problem

Discrete dynamic model

$$u(t_j) = \eta \sum_{i=1}^{R} S_{1,i}(t_j)c_i(t_j) + S_{2,i}(t_j)\Big(\frac{\partial c}{\partial t}\Big)_i(t_j)\,, \qquad j = 1,\dots,n_T\,. \quad (4.7)$$

In practice, scan protocols often take multiple cycles. For measurements with $l \geq 1$ cycles, the time sampling for the measurement and concentration changes to $\{\tau_j\}_{j=1,\dots,ln_T}$ with $\tau_j = (j-1)lT_c/(ln_T - 1)$ while the system functions are evaluated at $t_{j \bmod n_T}$. Equation (4.7) can no longer be interpreted as a matrix-

vector multiplication as in (3.6) but a sum of element-wise multiplied matrices

$$\mathbf{u} = \eta\big[\mathbf{S}_1 \odot \mathbf{c} + \mathbf{S}_2 \odot \mathbf{D}_c\big] \cdot 1_R$$

with $\mathbf{u} \in \mathbb{R}^{n_T},\ \mathbf{c}, \mathbf{D}_c \in \mathbb{R}^{n_T \times R},\ \mathbf{S}_1, \mathbf{S}_2 \in \mathbb{R}^{n_T \times R},\ 1_R = [1, \dots, 1]^\top \in \mathbb{N}^R$ and $\odot$ being an element-wise matrix multiplication, e.g. $\mathbf{A} \odot \mathbf{B} = [a_{ij} b_{ij}]_{i=1,\dots,n}^{j=1,\dots,m}$, with matrices $\mathbf{A}, \mathbf{B} \in \mathbb{R}^{n \times m}$.
The dynamic model in frequency space can be discretized analogously resulting in the following discrete forward problem

$$\hat{\mathbf{u}} = \eta\big[\hat{\mathbf{S}}_1 * \hat{\mathbf{c}} + \hat{\mathbf{S}}_2 * \hat{\mathbf{D}}_c\big] \cdot 1_R$$

with $\hat{\mathbf{u}} \in \mathbb{C}^{n_K}, \hat{\mathbf{c}}, \hat{\mathbf{D}}_c \in \mathbb{C}^{n_K \times R}, \hat{\mathbf{S}}_1, \hat{\mathbf{S}}_2 \in \mathbb{C}^{n_K \times R}, 1_R = [1, \dots, 1]^\top \in \mathbb{N}^R$. Again the convolution is only applied to the frequency components, i.e. the respective matrix columns. Note that in contrast to the static case a frequency domain reconstruction computes $\hat{c}$. To see the behavior of the concentration in time, the inverse Fourier transform needs to be applied.
Another alteration is that frequency domain reconstruction becomes a deconvolution problem. The standard approach for solving this ill-posed inverse problem is to make use of the convolution theorem of the Fourier transform which in this case results in time domain reconstruction. Thus, at least in the case simulated data where time domain measurements are easily available, reconstruction in time domain is more intuitive and computationally attractive.
The dynamic model (4.3) has already been introduced in [25] but prior knowledge of periodicity and velocity limits allows the authors to neglect the second summand. However, the models proposed in this work are valid for a broad range of dynamics, e.g. rapid changes or non-periodic behavior. For our derivations we assume the concentration and magnetization function to be in H^1 and the dynamic concentration model in Section 5.1 describes tracer distributions which are differentiable in time and integrable in space.

4.2. Dynamic Multi-Patch Models

The dynamic model 4.4 can be adapted to the

Dynamic multi-patch model

$$u^p(t) = \eta \int_\Omega S_1(r,t)c^p(r,t) + S_2(r,t)\frac{\partial c^p}{\partial t}(r,t)\,\mathrm{d}r\,, \qquad p = 1,\dots,P\,, \quad (4.8)$$

for P patches. Assuming ideal magnetic fields the same system matrices can be used for all patches. As discussed in Section 3.3, system matrices are not shift-invariant in practice and magnetic fields are distorted. This affects especially measurements of off-center patches. Patch specific system matrices can be generated e.g. by additional calibration scans or by transforming a system matrix according to the current patch location [8]. The model can be easily adapted to patch-specific system matrices by using S_1^p and S_2^p, while generating or loading a new system matrix for each patch will increase the computational costs.

Discretization Also the dynamic multi-patch model can be discretized analogously to the static model with the pixel-basis $\{\phi_i\}_{i=1,\dots,R} \subset L^2$ used in Section 3.2.1. This yields the representations

$$\tilde{c}^p(r,t) = \sum_{i=1}^{R} c_i^p(t)\phi_i(r) \qquad \in X_R$$

of the piecewise constant dynamic concentration for each patch $p = 1,\dots,P$ and the derivative $\frac{\partial c^p}{\partial t}$ and system functions S_1 and S_2 analogously. Here, we choose equidistant sampling points

$$\{t_j\}_{j=1,\dots,FlPn_T} \text{ with } t_j = (j-1)FPlT_c/(FPn_T - 1)$$

for a measurement with F frames, P patches, l cycles per patch and T_c being the time of one excitation cycle. This yields the

Discrete dynamic multi-patch model

$$u^p(t_j) = \eta \sum_{i=1}^{R} S_{1,i}(t_j)c_i^p(t_j) + S_{2,i}(t_j)\Big(\frac{\partial c^p}{\partial t}\Big)_i(t_j)\,, \qquad p = 1,\dots,P\,, \quad (4.9)$$

in time-domain with periodic system functions, i.e. $S_i(t_j) = S_i(t_{j \bmod n_T})$. For all the forward models presented in this section holds that solving them for the tracer concentration c poses an ill-posed inverse problem.

4.3. Relevance of Dynamic Models for Different Velocities

In the beginning of this chapter, we presented MPI forward models for dynamic tracer distributions. In practice however, the concentration is still assumed to be constant during single scanning cycles. This corresponds to a time derivative of the concentration that is nearly zero, so that the second addend of the dynamic model (4.4) becomes negligibly small. In order to determine the influence of the second summand, we investigate the structure of S_2 in comparison to S_1. A set of simulated dynamic concentrations is used to identify cases where neglecting the second summand of (4.4) is reasonable.
The two system matrices are simulated according to the Langevin model on a $19 \times 19 \times 1$ grid with 1632 sampling points in time and the parameters listed in Table B.1. The dynamic forward model in frequency domain (4.6) forms a sum of two convolutions. In the first summand the time derivative of the magnetization function $\hat{S}_1$ is convolved with the concentration and in the second summand the magnetization function $\hat{S}_2$ is convolved with the time derivative of the concentration.
First, we are interested in the shape of the convolution kernels $\hat{S}_1$ and $\hat{S}_2$. Therefore, we compute

$$\max_{r \in \Omega} \{|\hat{S}_\omega(r,k)|\}, \qquad \omega \in \{1,2\}$$

which are shown in Figure 4.1 together with an approximation of their convex hulls. The approximation of the convex hull was calculated by determining and connecting the maximum values within the next 15 frequency steps to include all peaks of the function. The structure of the curves is very similar. Both exhibit multiple peaks with a distance of ca. 15 frequency steps. While the convex hulls show the same full-width-at-half-maximum (FWHM) of about 33 frequency steps,

the maximum of the second system matrix $\hat{S}_2$ is 10^4 smaller than the maximum of the first system matrix $\hat{S}_1$. This first experiment makes a case for neglecting the second term in the dynamic model.

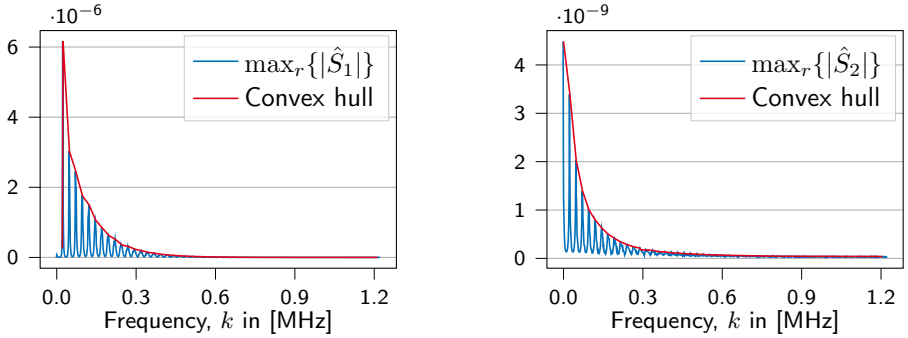

(a) Shape of system matrix 1 in Fourier space

(b) Shape of system matrix 2 in Fourier space

Figure 4.1.: Comparing the influence of the two system matrices by analyzing the maximum over all voxels of the absolute values of the matrices in Fourier space. The orange line is an approximation of the convex hull.

Second, we surveyed four types of dynamic concentrations together with their time derivatives and the respective Fourier transforms, visible in Figure 4.3. The dynamics occur during one scanning cycle in all four examples.
Example concentration 1 is depicted in Figure 4.3a which shows one peak at the beginning of the scan. The tracer is flowing through the voxel for a short period of time. This could be a small tracer bolus moving fast through the volume of the voxel. Example 2 is a periodic version of the first example. Figure 4.3b shows two peaks within the scan time. The tracer flows two times through the voxel with a high velocity. This represents a small bolus with fast periodic motion. In the third example, shown in Figure 4.3c, the concentration increases strongly in the beginning, remains constant for a short period of time and decreases again. This could be a larger tracer bolus with a high velocity. Example 4, shown in Figure 4.3d, shows a slow increase and decrease of the concentration. This represents bolus with low velocity.

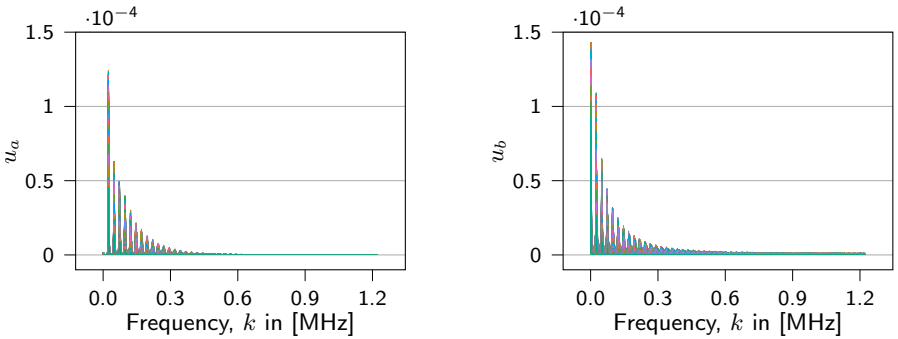

(a) $u_a = \hat{S}_1(r_i, k_j) * \hat{c}(r_i, k_j)$

(b) $u_b = \hat{S}_2(r_i, k_j) * \widehat{\frac{\partial c}{\partial t}}(r_i, k_j)$

Figure 4.2.: Absolute values of the convolution of the system matrices with example concentration 4 and its derivative. Each curve shows the frequency amplitudes for one of the 19^2 voxels.

It can be observed that the maximal absolute values of the Fourier transformed concentrations $\hat{c}$ are about 10^4 smaller than the maximal absolute values of the Fourier transformed time derivatives $\widehat{\frac{dc}{dt}}$. The imaging process in Fourier space is a convolution of the Fourier transformed system matrices with the Fourier transformed concentration and its time derivative. Thus, the concentration is smoothed by the system matrix. The kernels S_1 and S_2 have the same width meaning that the concentration and its derivative are smoothed equally. For the given dynamic concentrations, the different magnitudes are compensated such that the order of magnitude of the two summands is the same.
Third, we split up the discrete forward model such that the signal

$$\begin{aligned}\hat{u}(k_j) &= \eta \sum_{i=1}^{R} \underbrace{\hat{S}_1(r_i, k_j) * \hat{c}(r_i, k_j)}_{=:u_a(i,j)} + \eta \sum_{i=1}^{R} \underbrace{\hat{S}_2(r_i, k_j) * \widehat{\frac{\partial c}{\partial t}}(r_i, k_j)}_{=:u_b(i,j)} \\ &= \underbrace{\eta \sum_{i=1}^{R} a(i,j)}_{=:u_A(k_j)} + \underbrace{\eta \sum_{i=1}^{R} b(i,j)}_{=:u_B(k_j)}, \qquad j = 1, \ldots, n_K,\end{aligned}$$

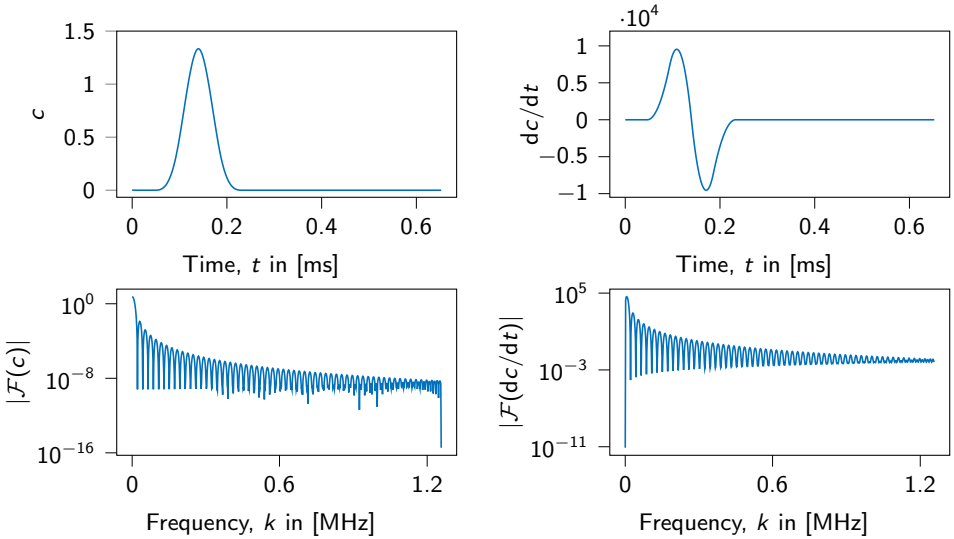

(a) Example 1: A small bolus moves through the voxel with a high velocity

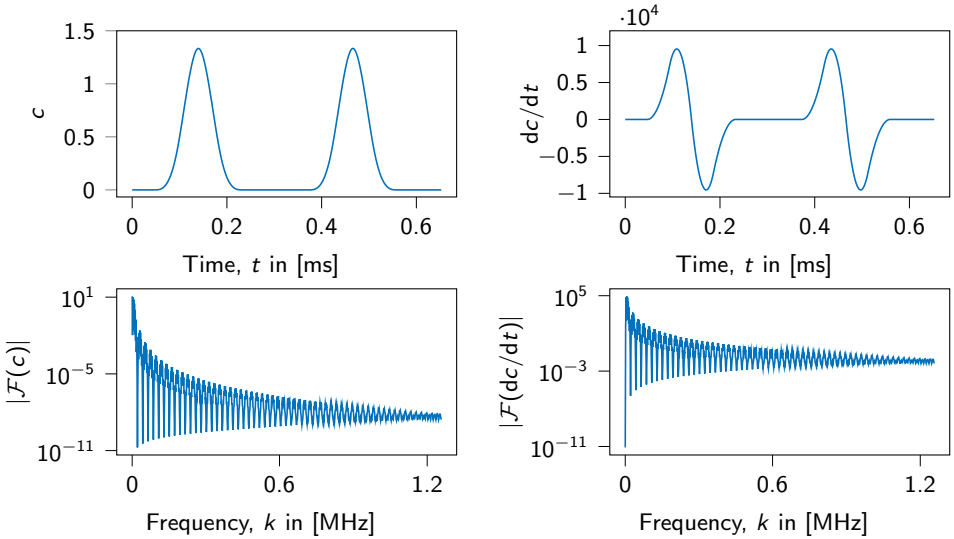

(b) Example 2: A small bolus moves through the voxel with a high velocity twice

Figure 4.3.: (Continued on the next page)

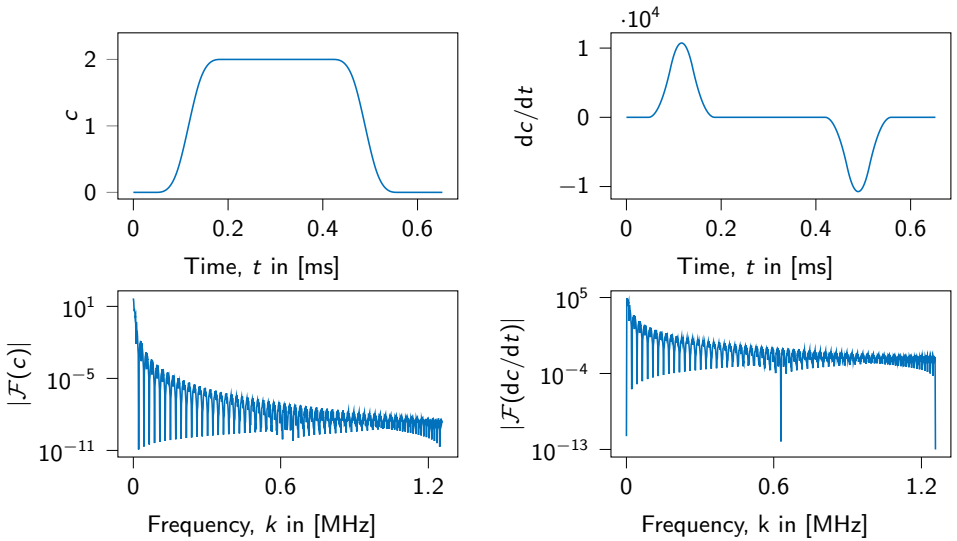

(c) Example 3: A larger tracer bolus moves through the voxel with a high velocity

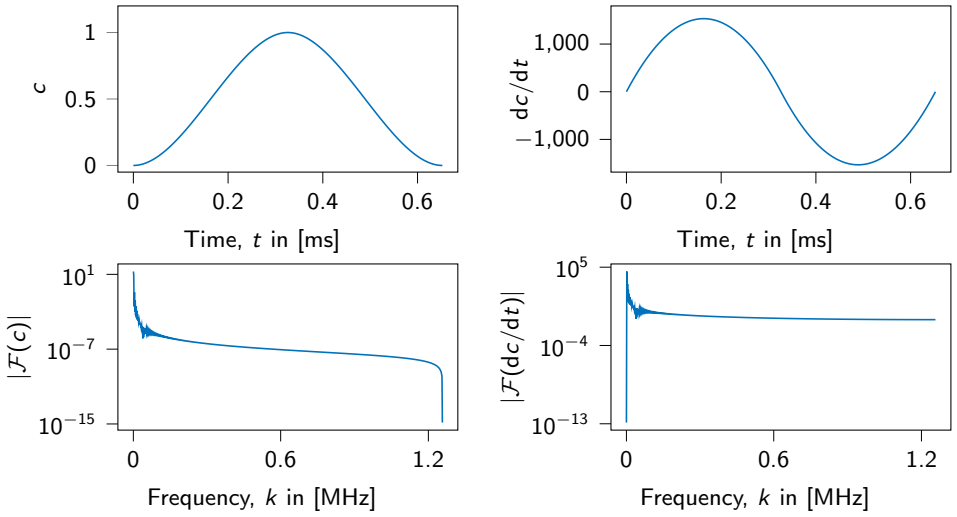

(d) Example 4: A bolus moves through the voxel with a slow velocity

Figure 4.3.: Example concentrations and their time derivatives in time and frequency domain. The dynamics appear within one scanning cycle.

is now the sum of u_A and u_B, where u_A denotes the signal component generated by the first system matrix S_1 and u_B the signal component generated by the second system matrix S_2. The convolution of the frequency components of system matrix 1 and the tracer distribution is named u_a and the convolution of system matrix 2 with the derivative of the concentration is named u_b.
The slower the dynamics the smaller is its time derivative and the higher the probability that the dynamic term, the second summand, is negligible. Using a concentration where each voxel behaves like example concentration 4 (see Figure 4.3d), Figure 4.2 shows u_a and u_b for each voxel. As expected, one can see that the shape and the maximum values of both terms are similar. Both plots show maximum values of about $1.2 \cdot 10^{-4}$.

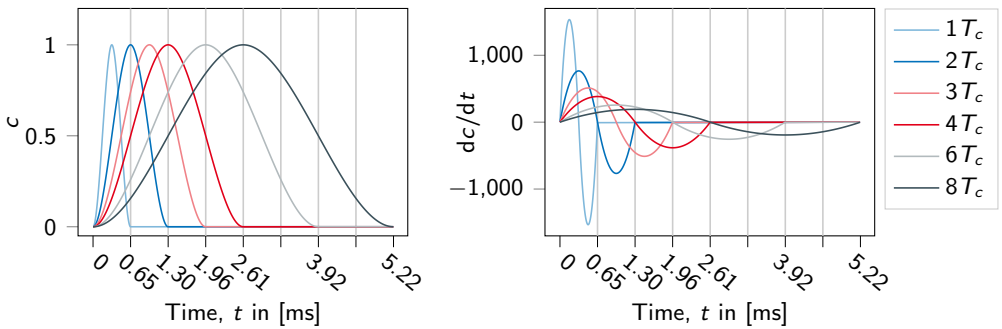

(a) Concentrations

(b) Change rates

Figure 4.4.: Concentrations with different velocities

All four example concentrations exhibit dynamics within one scanning cycle which is very fast. Example concentration 4 is non-zero in the interval $[0, T_c]$. In order to find examples with negligible dynamic term, five variants of concentration 4 are introduced. Figure 4.4a shows six concentrations with low velocities over time. The respective derivatives are illustrated in Figure 4.4b. The concentrations are smooth, symmetric, have a peak with value 1 and span a time interval of 1, 2, 3, 4, 6 and 8 times T_c with $T_c = 0.6528$ ms being the time of one 2D-Lissajous cycle. Variant $1T_c$ corresponds to example concentration 4.
To see the strength of the dynamics in the context of flow velocities, we relate

these values to a $2 \times 2 \times 2$ mm^3 bolus with constant concentration $c_{max} = 1$ moving through a $2 \times 2 \times 2$ mm^3 voxel with a constant velocity v (see Figure 4.5). The average change rate yields a bolus velocity of $v_{av} = 2 \cdot 10^{-3}/(0.5w)$ m/s with $w \in \{1T_c, 2T_c, 3T_c, 4T_c, 6T_c, 8T_c\}$. The velocities are listed in Table 4.1.

Table 4.1.: Phantom velocities

Width w	**Velocity** v_{av}
$1T_c$	6.13 m/s
$2T_c$	3.06 m/s
$3T_c$	2.04 m/s
$4T_c$	1.53 m/s
$6T_c$	1.02 m/s
$8T_c$	0.77 m/s

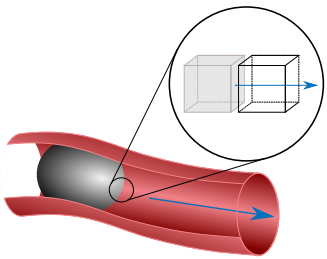

Figure 4.5.: Simplified bolus moving through a voxel.

Signal part u_A and u_B are computed for all six concentrations using spectral leakage correction since the concentrations are not periodic over multiple scanning cycles. Figure 4.6 shows the results for the frequencies $k \in [0.08, 1.25]$ MHz. u_A and u_B are of order of magnitude 10^{-5} for all six examples. In each cycle, u_A shows about three peaks for low frequencies below 0.2 MHz and nearly zero for higher frequencies while for u_B high amplitudes can be observed in the whole frequency range. The height of the peaks in u_B decreases with the velocity. For $1T_c$ and $2T_c$ the peaks of u_A and u_B have the same magnitude. Thus, in these cases the influence of the second addend on the signal is significant. For the slower concentrations, its influence depends on the respective cycle. The amplitude of the main peaks in u_A mimics the concentration curve (see Figure 4.4a) while the amplitude of the peaks in u_B depends on the concentration derivative (see Figure 4.4b).

Considering phantom $4T_c$, the absolute value of the change rate lies in the range of 0% and 50% of $\dot{c}_{max}$, with $\dot{c}_{max} = 1533$, in cycle 1 to 4. At the same time, the concentration shows values within 0% and 50% of c_{max} in cycle 1 and 4 and values within 50% and 100% of c_{max} in cycle 2 and 3. So the influence of the second summand is large in cycles with strong dynamics and low concentration values. This can be observed e.g. in the first and last cycle of $3T_c$ to $8T_c$. As the

first and last cycle represent respectively 66% and 50% of the signal of $3T_c$ and $4T_c$, and respectively 33% and 25% of the signal of $6T_c$ and $8T_c$, we can conclude that the second addend contributes significantly to the signal of $1T_c$ and $2T_c$, less but depending on the cycle to the signal of $3T_c$ and $4T_c$ and weakly to $6T_c$ and $8T_c$.

This experiment is not complex enough for a general statement but points out that the proportion of concentration to dynamics is relevant as well as the total velocity. We state a preliminary threshold velocity of $v^* = 1.53$ m/s for 2D trajectories. For tracer distributions with slower dynamics than v^*, the second summand in Equation (4.6) is negligible.

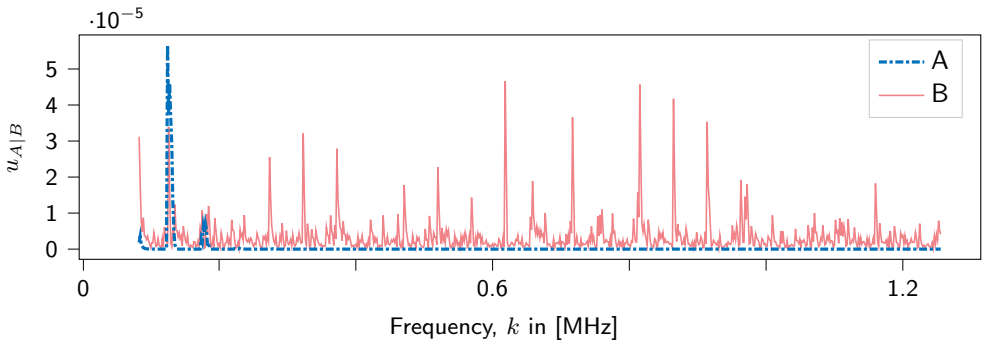

(a) $1T_c$

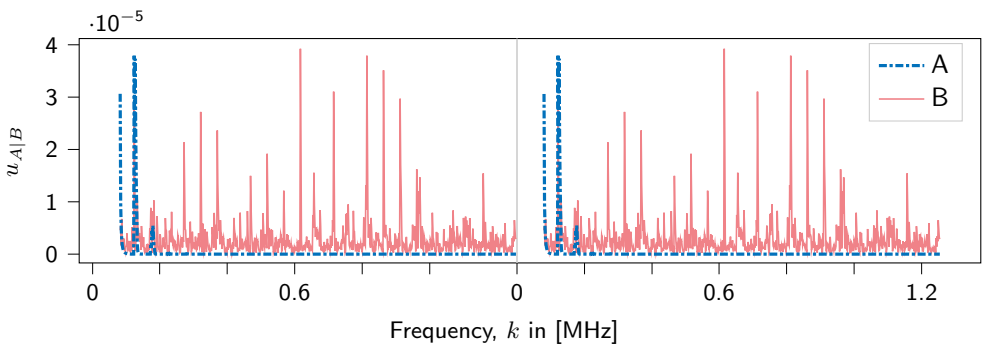

(b) $2T_c$

Figure 4.6.: (Continued on the next page)

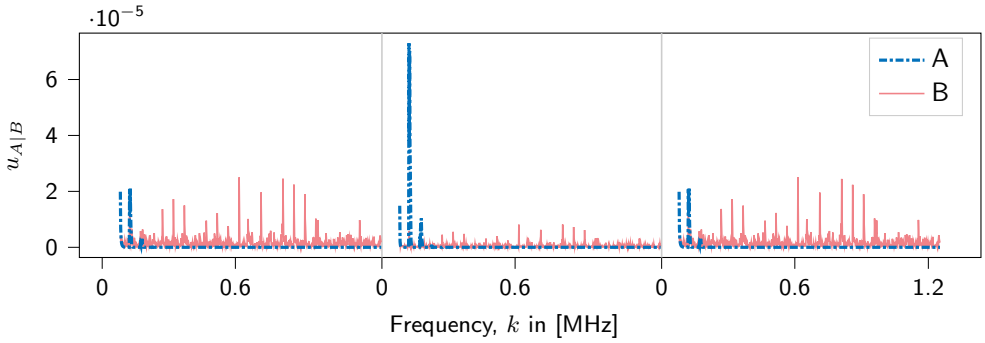

(c) $3T_c$

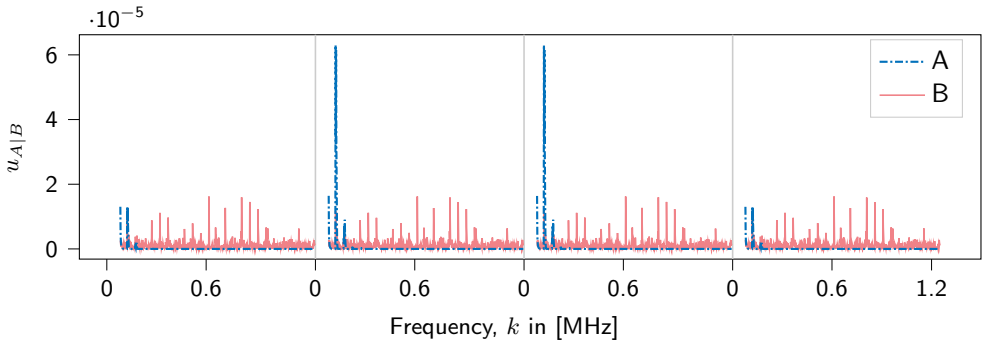

(d) $4T_c$

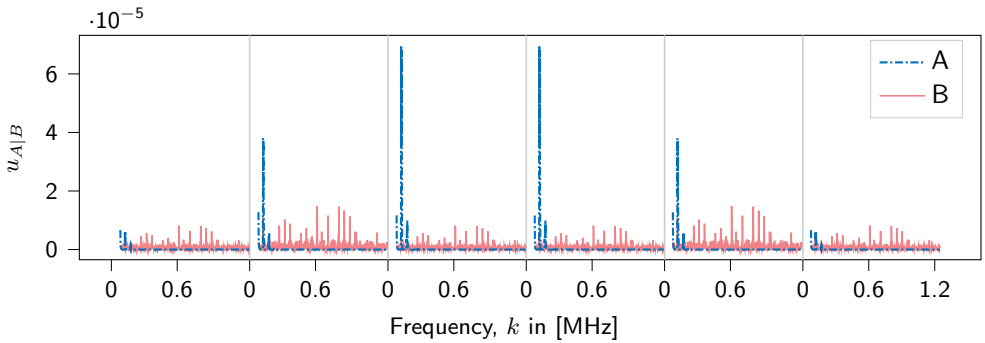

(e) $6T_c$

Figure 4.6.: (Continued on the next page)

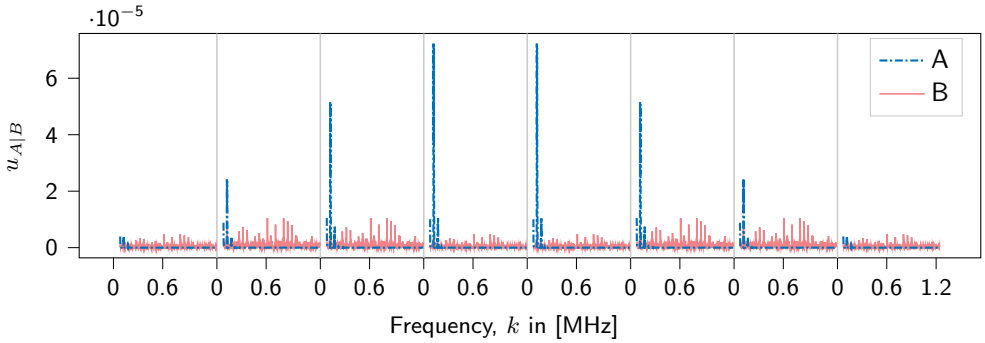

(f) $8T_c$

Figure 4.6.: u_A and u_B for different velocities. The phantoms' dynamics cover 1, 2, 3, 4, 6 and 8 cycles. In order to visualize u_A and u_B, the Fourier transform, spectral leakage correction and frequency selection are applied to each cycle separately. Thus, the frequency axis is a concatenation of several axes depending on the phantom.

5. Reconstruction of Dynamic Tracer Distributions

In the preceding chapters we have discussed the need for dynamic reconstruction methods in magnetic particle imaging. Furthermore, we have introduced a dynamic forward model including dynamic tracer concentrations and evaluated the relevance of the extended model. Reconstruction, however, remains a challenge, the increased degrees of freedom intensify the problem of ill-posedness even further. We remark that much of the material presented in this chapter has been published in [12].

5.1. Data Structure in Dynamic Multi-Patch Scans

In MPI literature the term frame often refers to one measured cycle. In this work however, the term is used in analogy to video processing. A video is a time-series of frames showing the full spatial range. Consequently in the MPI context, one frame covers P patches each scanned for l cycles, see Figure 5.1a.
Multi-patch sequences introduce additional challenges to dynamic MPI reconstruction. In practice, patches are usually scanned multiple times to increase the signal-to-noise ratio by averaging. The voltage measured in a multi-patch imaging sequence with $F = 2$ frames, $P = 2$ patches and $l = 3$ excitation cycles per patch is outlined in Figure 5.2. The focus shift takes Δ_f seconds and the repetition time of one cycle is denoted by T_c. Thus, the scanning time of one patch takes $T_P = lT_c + \Delta_f$ seconds, $T_F = PT_P$ is the scanning time of one frame and $T = FT_f$ is the total scanning time. The scheme shows that the voltage signal u is a concatenation of the measurements of each patch and each frame. For each patch there are F gaps of length $(P-1)T_P$ where no voltage is measured. Hence,

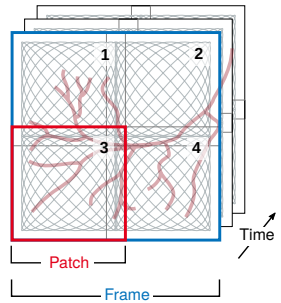

(a) Definition of components in dynamic MPI reconstruction.

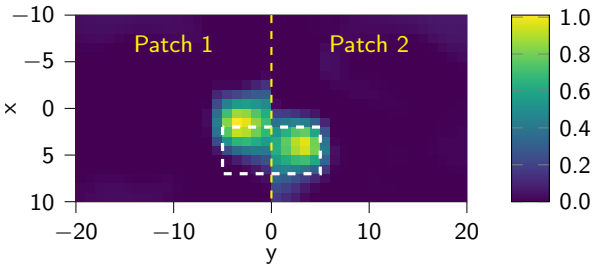

(b) Displacement artifact in a dynamic multi-patch reconstruction caused by strong dynamics. The dashed white box shows the outlines of the phantom at this point of time.

Figure 5.1.: Dynamic multi-patch MPI

the temporal resolution decreases proportional to the number of patches and repetitions per patch. The data from focus shift intervals is not used in this work. Although reconstruction of the focus shift is possible [60, 79], this data cannot be related to one specific patch.

Moreover, the scheme in Figure 5.2 illustrates that patches belonging to the same frame are not measured at the same time point. This temporal displacement in the measurement results in spatial displacements in the reconstruction. Objects covering the patch border can be distorted or objects with parallel motion might appear at different positions if they are covered by different patches. An example of these displacement or multi-patch artifacts is depicted in Figure 5.1b. The figure shows a Kaczmarz reconstruction of a phantom with a linearly moving box with high velocity which is scanned in a two-patch sequence. The left half of the box located in the first patch is shifted with respect to the right half located in the second patch. The second patch was scanned at a later time point when the box had already moved forward. An increasing number of patches or repetitions per patch implies a reduction in temporal resolution and an extension of the data gaps and thus an increase of multi-patch artifacts. In the remainder of this work, we will assume $l = 1$ and $\Delta_f = 0$ so that $T_c = T_P$.

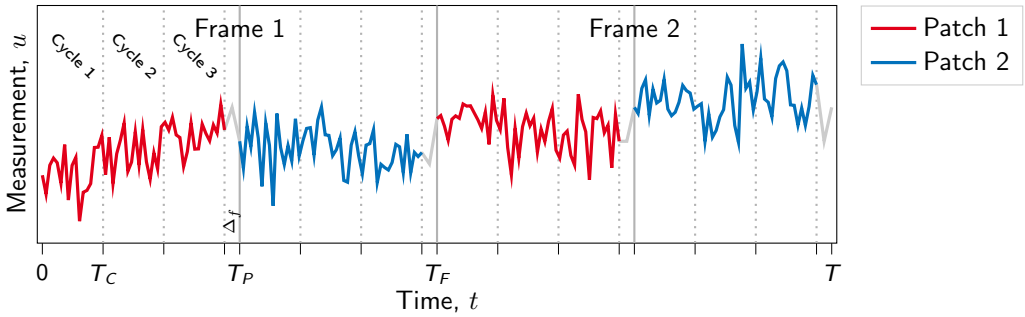

Figure 5.2.: Visualization of a multi-patch imaging sequence for $F = 2$ frames, $P = 2$ patches and $l = 3$ excitation cycles per patch. The measured voltage is a concatenation of the measurements of each patch and each frame. The focus shift to move the FFP to the starting point of the next patch takes Δ_f seconds. T_c denotes the repetition time of the trajectory. $T_P = lT_c + \Delta_f$ is the scanning time of one patch, $T_F = PT_P$ is the scanning time of one frame and $T = FT_f$ is the total scanning time.

5.2. Modelling of Dynamic Tracer Distributions for Multi-Patch Scans

Using a parameterized model for the dynamic tracer distribution allows to include prior knowledge in the reconstruction process and reduces the degrees of freedom. To find a feasible model, relevant characteristics of the tracer distribution need to be identified. The tracer is located in vessels or organs with strict boundaries. In order to represent these cases of high spatial gradients correctly, the concentration c may be discontinuous in space. Another property of the tracer is that it does not appear instantaneously, but accumulates, is dissipated or flows through the volume covered by one voxel. As a consequence, concentration c should be continuously differentiable in time.

In [33] spline curves are used to reconstruct dynamic concentrations from gated cardiac SPECT data. For each voxel and gate, a time activity curve of the radioactive tracer is modeled by a cubic B-spline curve. This allows for a representation of the smooth accumulation and radioactive decay in time and strong

spatial gradients, e.g. at organ boundaries, in space while using only few parameters. The method presented in this chapter builds on this idea to approach the challenges of dynamic multi-patch MPI reconstruction. We start with the main concept of the proposed reconstruction method, which is followed by a brief introduction to splines in Section 5.3 and presentation of a suitable spline setup for modeling dynamic concentrations in Section 5.4.
A dynamic tracer distribution in voxel $r_i \in \Omega \subset \mathbb{R}^3$ of patch p and its time-derivative can be modeled by the spline curves

$$c^p(r_i,t) = \sum_{m\in M_p} b_{m,i} B_m(t) \quad \text{and} \quad \frac{\partial c^p}{\partial t}(r_i,t) = \sum_{m\in M_p} b_{m,i} \frac{\mathrm{d}}{\mathrm{d}t} B_m(t) \tag{5.1}$$

for $t \in [0,T]$. Here, $B_m(t)$ denotes the m-th cubic B-spline and $b_{m,i}$ one of the m_p coefficients or control points for each voxel. There is a separate set of coefficients and splines for each patch. To reduce the amount of multiple indices, we define the index set

$$M_p = \{m \,|\, m = \tilde{m} + \sum_{\tilde{p}<p} m_{\tilde{p}},\ \tilde{m} = 1,\dots,m_p\}$$

containing the indices of coefficients and B-splines of patch p.
These spline curves c^p are defined on the total scanning interval $[0,T]$ and allow to describe twice continuously differentiable tracer distributions in time and discontinuities in space. The concentration is now a parameterized curve $\mathbf{c}(\Lambda_B, t)$ depending on parameter

$$\Lambda_B = \{b_{m,i} \mid b_{m,i} \geq 0,\ p = 1,\dots,P,\ m \in M_p,\ i = 1,\dots,R\}$$

which is the set of all coefficients. In contrast to [33] where the time activity curves model relatively simple decay processes requiring only few basis splines, here the spline curve approximates more complex dynamics. So the reduction of parameters is less than in [33]. Nevertheless, this model reduces the degrees of freedom and imposes an implicit regularization. Furthermore, it is able to compensate the problem of data gaps by approximating the data during the scanning time of the remaining patches.

The dynamic concentration model is plugged into the multi-patch model (4.9) to state the minimization problem

Dynamic reconstruction in time domain

$$\min_{b\in\Lambda_B} \sum_{p=1}^{P} \frac{1}{2} \Bigg\| \Big[\sum_{i=1}^{R} S_1(r_i,t_j) \sum_{m\in M_p} b_{m,i} B_m(t_j) + S_2(r_i,t_j) \sum_{m\in M_p} b_{m,i} \frac{\mathrm{d}}{\mathrm{d}t} B_m(t_j) \Big]_{j=1}^{Fn_T} - u^p \Bigg\|_2^2 + \gamma \mathcal{R}(\Lambda_B) \quad (5.2)$$

for dynamic multi-patch reconstruction with $r_i \in \Omega$ and $t_j \in I_p \subset [0,T]$. It is minimized with respect to the set of all control points Λ_B. While measurement data u^p is only available in the intervals

$$I_p = \bigcup_{f=1}^{F} [(p-1)T_P + (f-1)T_F,\ pT_P + (f-1)T_F],$$

the parameterized concentration curves c^p can be computed on the total scanning interval $[0,T]$.
Alternatively, we can formulate the dynamic multi-patch reconstruction problem in Fourier domain. This minimization problem

Dynamic reconstruction in frequency domain

$$\min_{b\in\Lambda_B} \sum_{p=1}^{P} \frac{1}{2} \Bigg\| \frac{1}{\sqrt{n_T}} \Big[\sum_{i=1}^{R} \hat{S}_1(r_i,k_j) * \hat{c}^p(r_i,k_j) + \hat{S}_2(r_i,k_j) * \widehat{\frac{\partial c^p}{\partial t}}(r_i,k_j) \Big]_{j=1}^{Fn_K} - \hat{u}^p \Bigg\|_2^2 + \gamma \mathcal{R}(\Lambda_B) \quad (5.3)$$

contains convolutions of the system matrices and the Fourier transform of the

concentration modeled by splines

$$\hat{c}^p(r_i, k_j) = \sum_{m \in M_p} b_{m,i} \hat{B}_m(k_j)\,, \qquad \widehat{\frac{\partial c^p}{\partial t}}(r_i, k_j) = \sum_{m \in M_p} b_{m,i} \widehat{\frac{\mathrm{d}}{\mathrm{d}t} B_m}(k_j)\,.$$

The number of sampled frequencies is denoted by n_K while $\mathcal{R} \in L^2(\Omega)$ and $\gamma \in \mathbb{R}$ in (5.2) and (5.3) denote an optional regularization term and parameter. The convolution is only applied to the frequency components.
Note that in time as well as in frequency domain the set of control points is reconstructed. Thus, a given spline basis yields the tracer distribution in time domain while the computation of its time derivative and Fourier transform is cheap.
Since measured data is oftentimes given in frequency domain and processing steps like frequency selection or spectral leakage correction are applied on frequency data, reconstruction is usually realized in frequency space. The additional deconvolution problem and the handling of complex numbers makes this approach computationally more costly and reconstruction in time domain more interesting. The minimization problems above can be solved with various minimization methods, e.g. gradient descent, or extended with further regularization terms. The computation of the gradient dominates the computational complexity in gradient-based methods. Reconstructing a sequence of FPn_T images of P patches with the dynamic approach, one gradient computation costs $\mathcal{O}(FPn_TR^2M^2)$ with $M = \max\{m_p, p = 1, \ldots, P\}$. As one Kaczmarz iteration costs $\mathcal{O}(n_TR)$ [48], the corresponding iteration for a frame-by-frame Kaczmarz reconstruction of F images and P patches has a complexity of $\mathcal{O}(FPn_TR)$.

5.3. Fundamentals of Splines

B-splines are an important tool in the fields of approximation geometric modeling and computer graphics. This section introduces the fundamentals of B-spline theory required for the setup which will be presented in Section 5.4. For a more comprehensive treatment of B-splines we refer to [40]. A Spline curve is a linear combination of B-spline basis functions which are defined via a so-called knot vector.

Definition 5.1 (Knot vector)**.** *A vector* $\mathbf{t} = [\tau_j]_{j=1}^{\nu+d+1} \in \mathbb{R}^{\nu+d+1}$ *with* $\tau_j \leq \tau_{j+1}$ *for* $j = 1, \ldots, \nu + d$ *is called a knot vector.*
A knot vector is called $d+1$*-extended if*

1. $\nu \geq d + 1$,
2. $\tau_{d+1} < \tau_{d+2}$ *and* $\tau_\nu < \tau_{\nu+1}$,
3. $\tau_j < \tau_{j+d+1}$ *for* $j = 1, \ldots, \nu$.

A $d+1$*-extended knot vector is called* $d+1$*-regular if* $\tau_1 = \tau_{d+1}$ *and* $\tau_{\nu+1} = \tau_{\nu+d+1}$.

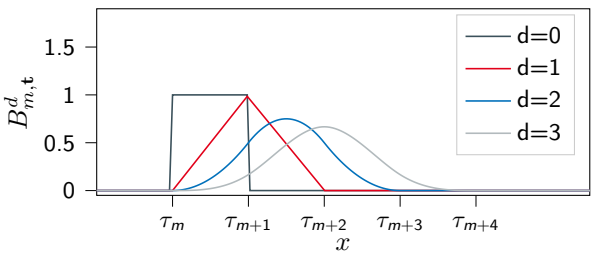

(a) The support of a B-spline depends on its degree and knot vector

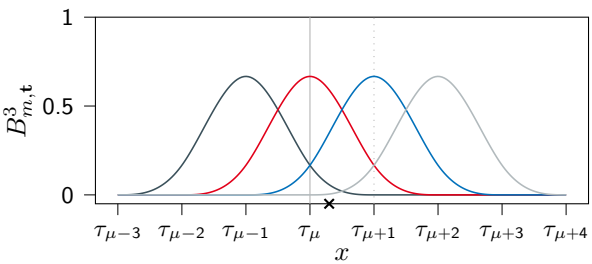

(b) Computing $f(x)$ with $x \in [\tau_\mu, \tau_{\mu+1})$ requires only $d+1$ basis splines, here $d = 3$.

Figure 5.3.: B-splines of different degrees with finite support.

Definition 5.2 (B-Spline). *Given a knot vector* $\mathbf{t}$*, the B-splines* $B^d_{m,\mathbf{t}}$ *of degree* d *are defined by the recursion*

$$B^d_{m,\mathbf{t}} = \alpha^d_{m,\mathbf{t}} B^{d-1}_{m,\mathbf{t}} + (1 - \alpha^d_{m+1,\mathbf{t}}) B^{d-1}_{m+1,\mathbf{t}}, \qquad \alpha^d_{m,\mathbf{t}}(x) = \frac{x - \tau_m}{\tau_{m+d} - \tau_m},$$

starting from the characteristic functions

$$B^0_{m,\mathbf{t}} = \begin{cases} 1 & x \in [\tau_m, \tau_{m+1}), \\ 0 & \textit{otherwise.} \end{cases}$$

If the degree and knot vector are fixed we can write $B_m = B^d_{m,\mathbf{t}}$.

Figure 5.3a shows B-splines with different degrees for a knot vector with equally spaced knots.

Definition 5.3 (Spline). *Let* $\mathbf{t} = [\tau_j]_{j=1,\dots,\nu+d+1}$ *be a knot vector for* ν *B-splines of degree* d*. The linear space of all linear combinations of these B-splines is the spline space* $\mathbb{S}_{d,\mathbf{t}}$ *defined by*

$$\begin{aligned} \mathbb{S}_{d,\mathbf{t}} &= span\{B_{1,d}, \dots, B_{\nu,d}\} \\ &= \left\{ f(x) = \sum_{m=1}^{\nu} b_m B_m(x) \,\middle|\, b_m \in \mathbb{R} \text{ for } 1 \le m \le \nu \right\}. \end{aligned} \tag{5.4}$$

An element $f \in \mathbb{S}_{d,\mathbf{t}}$ *is called a spline function, or just a spline, of degree* d *with knots* $\mathbf{t}$*, and* $[b_m]_{m=1}^{\nu}$ *are called the B-spline coefficients of* f.

Spline curves have a few interesting properties. B-splines have finite support. Thus, computing the function value of a spline curve within a knot interval, only $d + 1$ B-splines are required. Moreover smoothness of spline curve is determined by the setup of the knot vector.

Lemma 5.4. *Let* $\mathbf{t} = [\tau_j]_{j=1,\dots,\nu+d+1}$ *be a knot vector for splines of degree* d *with* $\nu \geq d+1$ *and let*

$$f(x) = \sum_{m=1}^{\nu} b_m B_m(x) \qquad \in \mathbb{S}_{d,\mathbf{t}}.$$

Then the spline f *has the following properties:*

1. *If* x *is in the interval* $[\tau_\mu, \tau_{\mu+1})$ *for some* μ *in the range* $d+1 \leq \mu \leq \nu$ *then*

$$f(x) = \sum_{m=\mu-d}^{\mu} b_m B_m(x).$$

2. *If* $z = \tau_{j+1} = \cdots = \tau_{j+d} < \tau_{j+d+1}$ *for some* j *in the range* $1 \leq j \leq \nu$ *then* $f(z) = b_m$.

3. *If* z *occurs* q *times in* $\mathbf{t}$ *then* f *has continuous derivatives of order* $0, \dots, d-q$ *at* z.

A proof can be found in [40, p. 64].

Property 1 in Lemma 5.4 is highlighted in Figure 5.3b. The geometric interpretation of the coefficients are the y-coordinates of the so-called control polygon.

Definition 5.5 (Control polygon)**.** *Let* $f(x) = \sum_{m=1}^{\nu} b_m B_m^d(x)$ *be a spline in* $\mathbb{S}_{d,\mathbf{t}}$. *The control points of* f *are the points with coordinates* (τ_m^*, b_m) *for* $m = 1, \dots, \nu$, *where*

$$\tau_m^* = \frac{\tau_{m+1} + \cdots + \tau_{m+d}}{d}$$

are the knot averages of $\mathbf{t}$. *The control polygon of* f *is the piecewise linear function obtained by connecting neighboring control points by straight lines.*

An example of a control polygon can bee seen in Figure 5.5.

5.4. Spline Setup for Dynamic Concentration Models

In the preceding section we discussed characteristics of the tracer material which should be incorporated in the dynamic concentration model and proposed the usage of spline curves (5.1). The exact properties of a spline curve depend on the B-spline space they are contained in. B-splines are a used extensively in approximation, geometric modeling or computer graphics due to their efficiency and flexibility. Spline curves are defined via their degree, control points and knot vector. We refer to Appendix 5.3 for theoretical details.

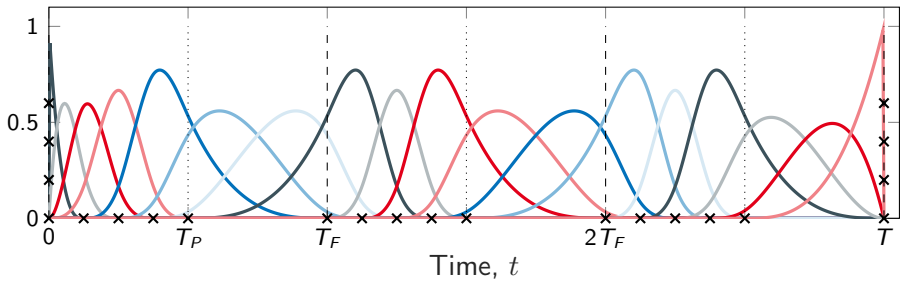

(a) Set of cubic B-splines $B_{m,\mathbf{t}^1}(t)$ with $m \in M_1$ which spans spline space $\mathbb{S}_{3,\mathbf{t}^1} \ni c^1$.

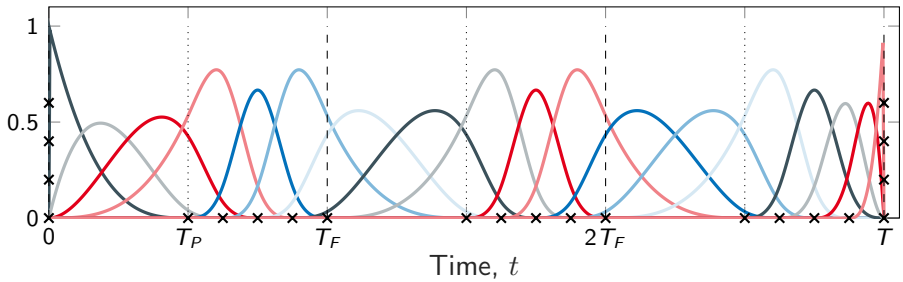

(b) Set of cubic B-splines $B_{m,\mathbf{t}^2}(t)$ with $m \in M_2$ which spans spline space $\mathbb{S}_{3,\mathbf{t}^2} \ni c^2$.

Figure 5.4.: Knots and cubic B-spline basis for $P = 2$ patches and $F = 3$ frames. In each scanning interval of the patch are $M_0 = 5$ uniformly distributed knots. Additional knots at 0 and T have multiplicity 4.

The basis splines B_m are defined via the degree and the knot vector. In order to satisfy the required features from Section 5.2, feasible spline parameters need to be determined.

a) A twice continuously differentiable tracer distribution in the scan time $(0, T)$ is guaranteed by B-splines of degree $d = 3$ with $d + 1$-regular knot vectors $\mathbf{t}^p = [\tau_j]_{j=1}^{m_p+d+1}$ with $\tau_j < \tau_{j+1}$ for $j = d + 1, \ldots, m_p$ and $p = 1, \ldots, P$.

b) In a single-patch setting, it is ensured that the spline curve is defined on $[0, T]$ and coincides with the control points in 0 and T if $M_0 F$ knots are uniformly distributed in $[0, T]$ and the multiplicity of the knots in 0 and T is increased to 4.

c) In a multi-patch setting, we do have gaps in the measurement data, as discussed in Section 5.2. To ensure that the spline curve is defined on $[0, T]$ and coincides with the control points in 0 and T in this case, M_0 knots are uniformly distributed in each scanning interval of the patch in each frame. Additional knots with multiplicity 4 are added at 0 and T.

With this setup the knot vector $\mathbf{t}^p$ for the first and last patch p has $M_0 F + 2d + 1$ elements ($M_0 F + 2d + 2$ for other patches) and the concentration curve c^p lies in the spline space $\mathbb{S}_{d,\mathbf{t}^p}$ (cf. (5.4)) spanned by $m_p = M_0 F + d$ B-splines ($m_p = M_0 F + d + 1$ for other patches) of degree d.
Figure 5.4 shows the cubic B-spline basis and knots with this setup for $P = 2$ patches, $F = 3$ frames and $M_0 = 5$ while an example concentration curve for a multi-patch sequence using this knot vector and spline basis is shown in Figure 5.5.

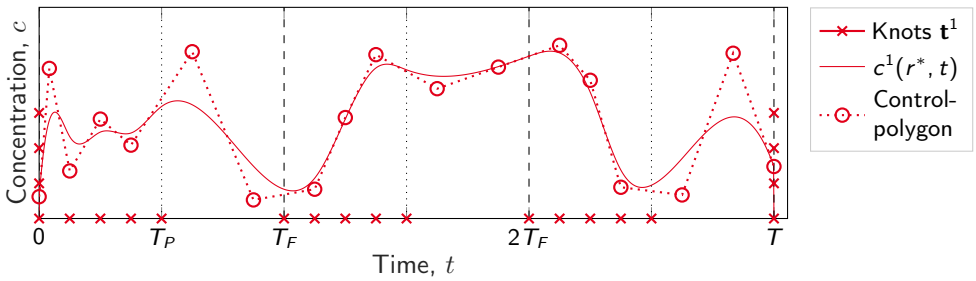

(a) The concentration in patch 1.

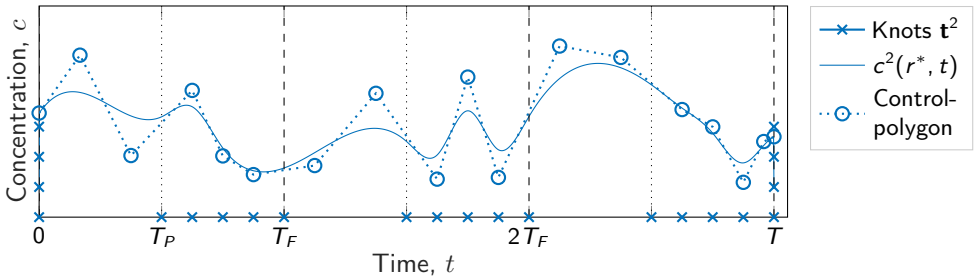

(b) The concentration in patch 2.

Figure 5.5.: Time development of a random spline concentration curve in an arbitrary fixed voxel r^* scanned with $P = 2$ patches and $F = 3$ frames. In each scanning interval of the patch, there are $M_0 = 5$ uniformly distributed knots. The first an last knots have multiplicity 4.

6. Experiments

To evaluate the dynamic forward model presented in Chapter 4 and the dynamic reconstruction method presented in Chapter 5.1, a simulation and reconstruction framework for magnetic particle imaging was implemented in Julia. Its structure is depicted in Figure 6.1. The system matrices are modeled according to the assumptions made in Chapters 3.1 and 4, Lissajous trajectory, ideal magnetic fields and the equilibrium model.

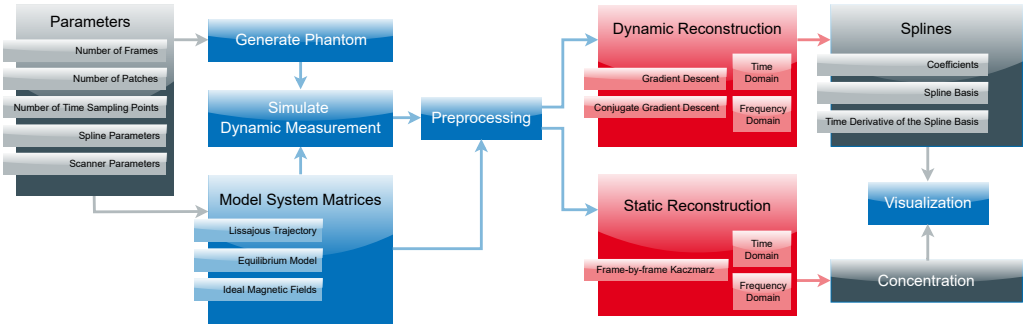

Figure 6.1.: Simulation framework for computational phantom simulations

We begin with simulated measurements from very small dynamic single-patch phantoms in Section 6.1 in order to investigate the effect of the concentration derivative on the reconstructions in Section 6.1.1 and the influence of noise on the quality of these reconstructions in Section 6.1.2. Furthermore, a dynamic measurement is reconstructed under the assumption of static behavior during each excitation cycle with a dynamic and the Kaczmarz method in Section 6.1.3 to include a case where the state-of-the-art is compatible. In Section 6.2 larger dynamic phantoms with single and multiple patches are reconstructed with dynamic and static reconstruction methods.

6.1. Computational Phantom Studies with Small Single-Patch Phantoms

The dynamic inverse problem (4.7) has many degrees of freedom. Since we focus on dynamics, we limit the spatial resolution of the phantoms. Two phantoms with a minimalist setup with a grid of $3 \times 3 \times 1$ voxels are generated. The *one-peak phantom* is used in Sections 6.1.1 and 6.1.2 and the *three-peak phantom* in Section 6.1.3. Their spatial setup can be seen in Figure 6.2. We point out that the experiments and results presented in Section 6.1.1 and the noise-free case in Section 6.1.3 have already been published in [11].

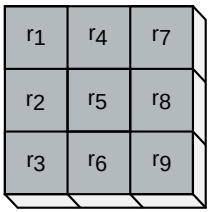

Figure 6.2.: Spatial setup of the one- and three-peak phantom. They consist of $3 \times 3 \times 1$ voxels indexed from 1 to 9.

6.1.1. Influence of the Concentration Derivative on Dynamic Reconstructions

The tracer concentration of the one-peak phantom is described by a cubic B-spline curve

$$c(r_i, t) = \sum_{m=1}^{M} b_{m,i} B_m(t) = \mathbf{c}(\Lambda_B^*, t) \qquad \in L^2(\mathbb{R}^3) \times C^2(\mathbb{R}) \tag{6.1}$$

for $i = 1, \ldots, 9$, with cubic B-splines B_m and parameter set

$$\Lambda_B^* = \{b_{m,i} \mid b_{m,5} \geq 0,\ b_{m,i} = 0,\ i \in \{1, \ldots, 9\} \setminus 5,\ m = 1, \ldots, M\}\,.$$

We design three variants of the one-peak phantom, 1F, 2F and 4F that vary only in $c(r_5, t)$, $t \in [0, T]$. The concentration of version 1F is non-zero within the scan time of one frame. The development of the tracer distribution for the total scan time is shown in Figure 6.3a where each curve describes the concentration within one voxel. There is one concentrations peak at $t = 0.41$ ms with a value of 2.67 for voxel r_5. Versions 2F and 4F differ in the width of the concentration peak. The concentration peak for r_5 lasts for the scan time of 2 frames in version 2F and 4 frames in version 4F (see Figure 6.3b).

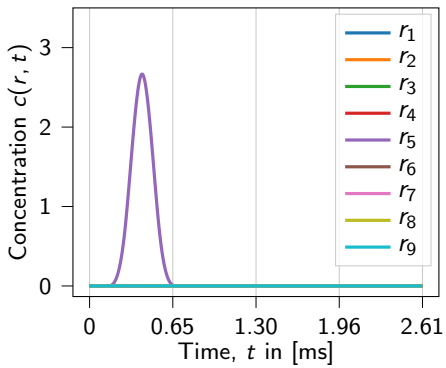

(a) The tracer distribution of the central voxel r_5 of one-peak phantom 1F changes during the scan of the first frame. The remaining voxels have a constant tracer concentration of zero.

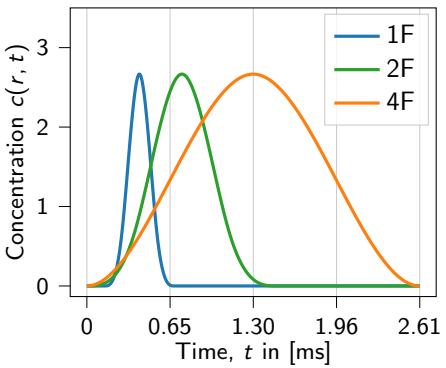

(b) The tracer distribution of the central voxel r_5 of the three versions of the one-peak phantom.

Figure 6.3.: The three versions of the one-peak phantom only differ in the width of the concentration peak of voxel r_5, while the remaining voxels have a constant tracer concentration of zero.

We simulate a measurement with 4 frames which are each sampled at 408 time points using the discrete dynamic forward model (4.7) with modeled system matrices $S_1 = \frac{\partial \bar{m}}{\partial t}$ and $S_2 = \bar{m}$. Table B.1 lists the physical and scanner parameters and the phantom specific parameters for the simulations can be found in Table B.2. The concentration curves are reconstructed with two different settings. In the first experiment, the inverse problem of determining parameter Λ_B from

given u and (4.7) with both matrices is solved by minimizing

$$\arg\min_{\Lambda_B} \left\| \left[\sum_{i=1}^{R} S_1(r_i, t_j)\mathbf{c}(\Lambda_B, t_j) + S_2(r_i, t_j)\frac{\partial \mathbf{c}}{\partial t}(\Lambda_B, t_j) \right]_{j=1}^{Fn_T} - \mathbf{u} \right\|_2^2 \tag{6.2}$$

with $\mathbf{u} \in \mathbb{R}^{Fn_T}$ and $R = 9$. Thus, the resulting tracer distribution is again a cubic spline curve and an implicit regularization is included since the solution set is restricted to parametric spline curves in $L^2(\mathbb{R}^3) \times C^2(\mathbb{R})$. Therefore, we forgo further regularization and minimize Problem (6.2) with 200 iterations of a conjugate gradient descent [27].

The average of reconstructions of the x- and y-channel of one-peak phantom 1F are shown in Figure 6.4a. The peak for voxel r_5 is located at $t = 0.44$ ms with a concentration of 2.96 which is very close to ground truth. In the same period of time also the concentration of the remaining voxels is non-zero. The peaks of the voxels with even indices have concentration values of about 0.9 and the peaks of the voxels with odd indices have even smaller values of about 0.4. Even though these voxels have a non-zero concentration, it is significantly lower than the value of r_5, so that we can expect sufficient contrast in the reconstructed images. The observation of higher values for the off-diagonal voxels (voxels with even indices, cf. Figure 6.2) than the ones on the diagonal can be explained by the averaging of two channels. The x-channel reconstruction locates the concentration correctly in x and the y-channel reconstruction locates the concentration correctly in y. Thus, the off-diagonal voxels are masked by the high concentration in the central voxel. In the next experiment the same measurement is reconstructed only with S_1 which corresponds to minimizing

$$\arg\min_{\Lambda_B} \left\| \left[\sum_{i=1}^{R} S_1(r_i, t_j)\mathbf{c}(\Lambda_B, t_j) \right]_{j=1}^{Fn_T} - \mathbf{u} \right\|_2^2 \tag{6.3}$$

with $\mathbf{u} \in \mathbb{R}^{Fn_T}$ and $R = 9$. Figure 6.4b depicts the average of x- and y-channel reconstructions from 200 conjugate gradient iterations. The concentration peak for voxel r_5 is located at $t = 0.38$ ms which is close to the ground truth but with a significantly smaller concentration of 0.85. Again there are concentration peaks

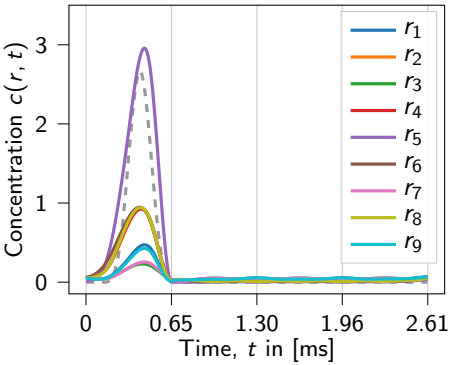

(a) Reconstruction of 1F with the dynamic model using S_1 and S_2.

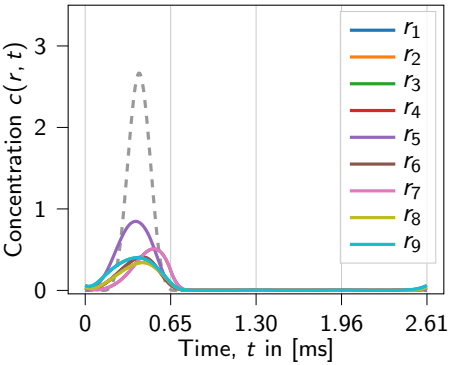

(b) Reconstruction of 1F using only S_1.

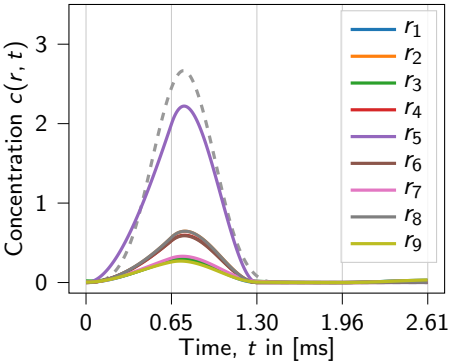

(c) Reconstruction of 2F with the dynamic model using S_1 and S_2.

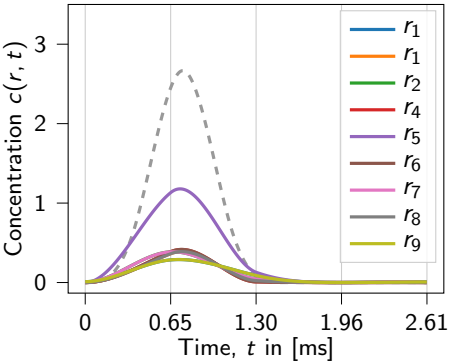

(d) Reconstruction of 2F using only S_1.

Figure 6.4.: (Continued on the next page)

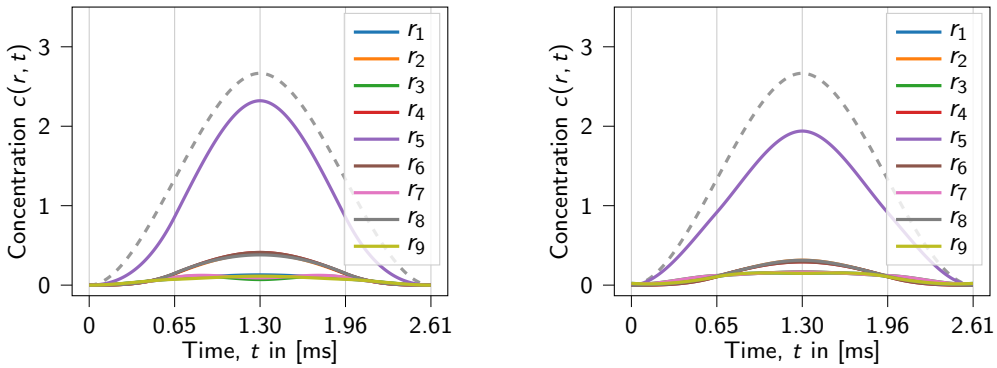

(e) Reconstruction of 4F with the dynamic model using S_1 and S_2.

(f) Reconstruction of 4F using only S_1.

Figure 6.4.: Measurements of the dynamic one-peak phantoms 1F, 2F and 4F are simulated with the dynamic forward model (4.7). They are reconstructed with either both S_1 and S_2 (left) or only S_1 (right). All plots show averages of x- and y-channel reconstructions. The dashed lines outline the true concentration in voxel r_5 and the vertical grid lines mark the start and end of frames.

in the same time interval for the remaining voxels with values of about 0.4. As a consequence, the reconstructed images will exhibit reduced contrast while the true concentration is underestimated.

The more intuitive way to judge the reconstruction quality of dynamic images, is to examine single frames. One frame of the phantom and the two reconstructed time-series at the time point of the maximum concentration ($t = 0.41$ ms) is shown in Figure 6.5. As expected, the reconstruction with both system matrices in Figure 6.5b exhibits high contrast and slightly higher concentration values for the off-diagonal voxels. Figure 6.5c shows the frame from the second experiment using only the first system matrix. The concentration is significantly lower compared to the phantom in Figure 6.5a and exhibits poor contrast.

In the next experiment, version 2F and 4F of the one-peak phantom are reconstructed analogously to version 1F. The reconstruction with both matrices (solution of 6.2) of version 2F is depicted in Figure 6.4c. It shows that the peaks

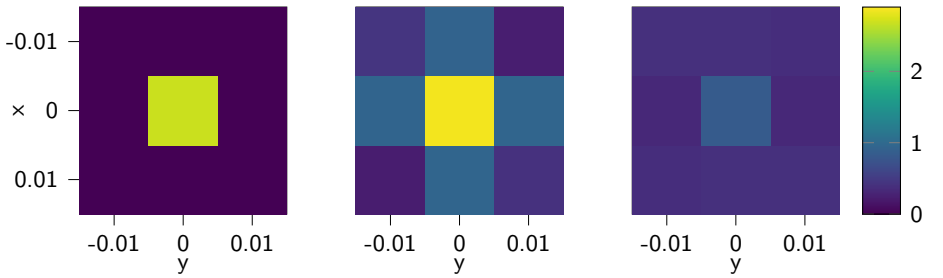

(a) Phantom (b) Reconstruction using S_1 and S_2 (c) Reconstruction using only S_1

Figure 6.5.: Reconstructions of the one-peak phantom 1F at the time point of the concentration peak $t = 0.41$ ms

are again located correctly and the amplitude of the main peak is 83% of the ground truth. Also here, the remaining voxels have low non-zero concentrations which are higher for the off-diagonal voxels. For the reconstruction using only S_1 (solution of 6.3), visible in Figure 6.4d, the main peak is less than 50% compared to the phantom. The amplitude of the peaks of the remaining voxels reaches 35% of the main peak. Thus, also for version 2F the reconstruction will exhibit poor contrast. Figure 6.4e and 6.4f show reconstructions with and without S_2 of version 4F. Again, the temporal location of the peaks is correct, while the amplitude of the peak for r_5 reaches 87% of the ground truth for the reconstruction with both matrices and 73% for using only S_1. The concentrations for the remaining voxels are sufficiently low in both cases. Figure 6.6 shows a frame of one-peak phantom 4F and the two reconstructed time-series at the time point of the maximum concentration ($t = 1.30$ ms). Looking at the reconstruction without S_2 (see Figure 6.6c) an improved contrast compared to version 1F can be observed. The reconstruction quality is similar to the reconstruction using S_1 and S_2 (see Figure 6.6b).

To get an impression on the strength of the dynamics in one-peak phantom 4F, as in Section 4.3, the concentration change rate of a phantom was related to the flow velocity of a $2 \times 2 \times 2$ mm^3 bolus with constant concentration c_{max} moved through a $2 \times 2 \times 2$ mm^3 voxel with a constant velocity v (see Figure 4.5). The

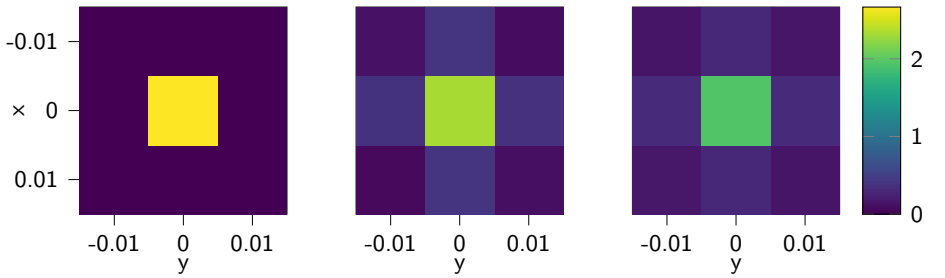

(a) Phantom (b) Reconstruction using S_1 and S_2 (c) Reconstruction using only S_1

Figure 6.6.: Reconstructions of one-peak phantom 4F at the time point of the concentration peak $t = 1.30$ ms

average change rate depends on the voxel size in flow direction (x=2 mm) and the time spent until the concentration reaches its maximum $c_{max} = 2.67$, for phantom 4F it is $\Delta_t = 2T_c$ s. The average change rate yields a bolus velocity of $v_{av} = 2 \cdot 10^{-3}/(2 \cdot T_c) = 1.53$ m/s for 2D trajectories with $T_c^{2D} = 0.6528$ ms. For 3D trajectories, which are mostly used in practice, $T_c^{3D} = 21.54$ ms leads to $v_{av} = 4.64$ cm/s, which is a velocity that is reached e.g. in human arterioles (cf. Table 6.2).

6.1.2. Noise Sensitivity

The initial experiments with the one-peak phantom in the preceding section use simulated measurements without noise. Since this is not a realistic setting, we examine the effects of different noise levels on the reconstruction with and without the second system matrix in this section. Again, we use the three variants of the one-peak phantom. Noisy measurements are simulated with

$$u^{\delta}(t_j) = u(t_j) + \delta \max_{l=1,\dots,Fn_T} \{|u(t_l)|\} N_j \,, \qquad j = 1, \dots, Fn_T \,, \tag{6.4}$$

with $N_j \sim \mathcal{N}(0,1)$ i.i.d. and noise level δ. This model has previously been used to model measurement noise in magnetic particle imaging in [57, 76]. We repeat

the experiments from Section 6.1.1 for noise levels $\delta \in \{10, 20, 30, 50\}\%$ while the results are shown in Figures 6.7 to 6.10.

10 percent (Figure 6.7) For 10%, noise the reconstruction results are very similar to the noiseless reconstructions. For all reconstructions except the one with both matrices of version 1F, the height of the peaks is slightly reduced. For phantom 1F and 2F, the concentration in interval $[0.65, 2.61]$ s and $[1.30, 2.61]$ s is no longer zero but still low.

20 percent (Figure 6.8) The reconstruction of 1F with both matrices still shows a significant peak for the central voxel. The noise affects mainly the concentration of the off-center voxels, whose peaks increased and show non-zero values in the whole scanning interval. The contrast will be reduced but the dynamics in voxel r_5 will still be clearly recognizable. In contrast to this, the reconstruction with S_1 does not show any specific peaks anymore and is completely dominated by noise. For version 2F, the main peaks are slightly decreased while the peaks for the off-center voxels increase which results in reduced contrast for both reconstruction methods.
For version 3F, the main peaks have the same amplitude as for 10% noise. The noise mainly influences the off-center voxels. For the reconstruction with both matrices there is no longer a difference in between the voxels off and on the diagonal.

30 percent (Figure 6.9) For 30%, the effects observed for 20% noise are amplified. For 4F both reconstruction methods yield similar results while for 1F and 2F the reconstructions with S_1 are useless while the main peak is still clearly distinguishable in the reconstructions with both matrices.

50 percent (Figure 6.10) For the extremely high noise level of 50%, also the reconstruction with both matrices of 1F becomes useless. The main peaks in all other reconstructions decreased further. The reconstructions with both matrices show distinguishable main peaks while the reconstruction without S_2 of version 4F exhibits a false side peak for voxel r_5.

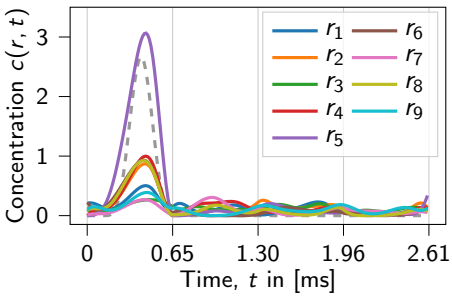

(a) Reconstruction of 1F with the dynamic model using S_1 and S_2.

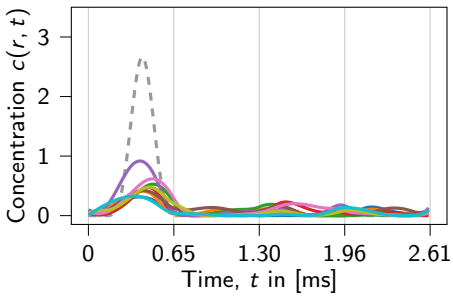

(b) Reconstruction of 1F using only S_1.

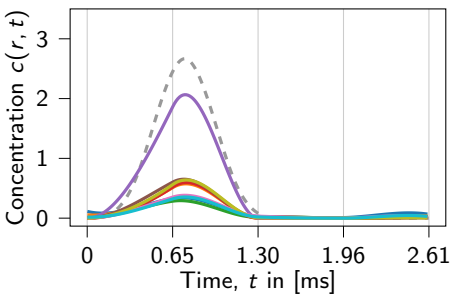

(c) Reconstruction of 2F with the dynamic model using S_1 and S_2.

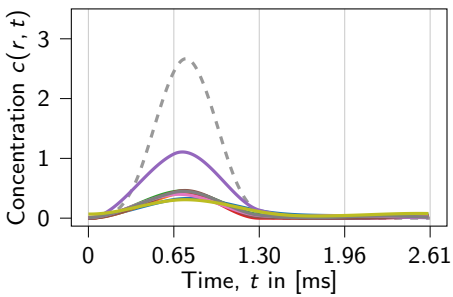

(d) Reconstruction of 2F using only S_1.

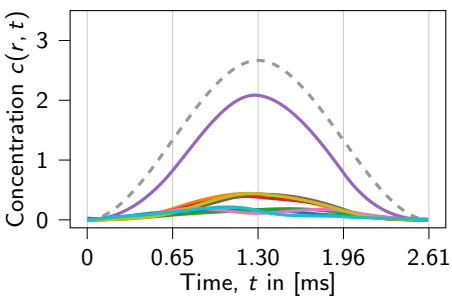

(e) Reconstruction of 4F with the dynamic model using S_1 and S_2.

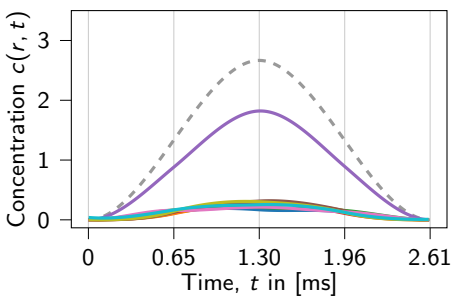

(f) Reconstruction of 4F using only S_1.

Figure 6.7.: Measurements of the dynamic one-peak phantom with 10% noise reconstructed with and without S_2.

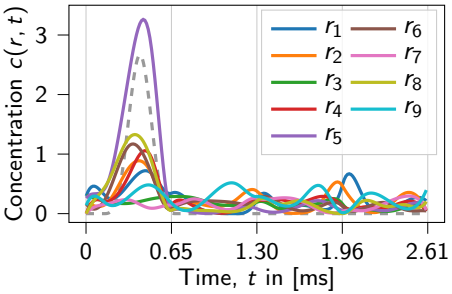

(a) Reconstruction of 1F with the dynamic model using S_1 and S_2.

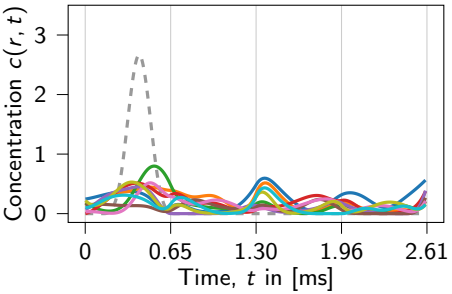

(b) Reconstruction of 1F using only S_1.

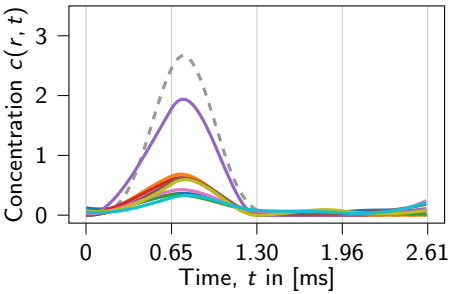

(c) Reconstruction of 2F with the dynamic model using S_1 and S_2.

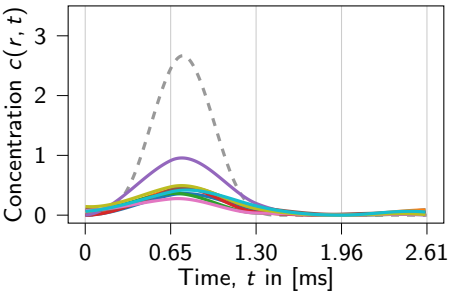

(d) Reconstruction of 2F using only S_1.

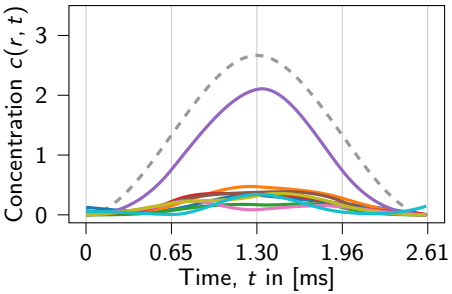

(e) Reconstruction of 4F with the dynamic model using S_1 and S_2.

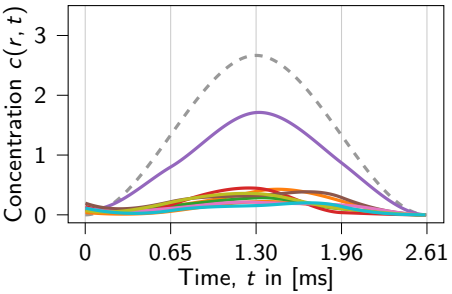

(f) Reconstruction of 4F using only S_1.

Figure 6.8.: Measurements of the dynamic one-peak phantom with 20% noise reconstructed with and without S_2.

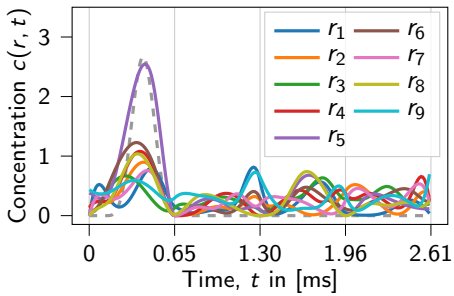

(a) Reconstruction of 1F with the dynamic model using S_1 and S_2.

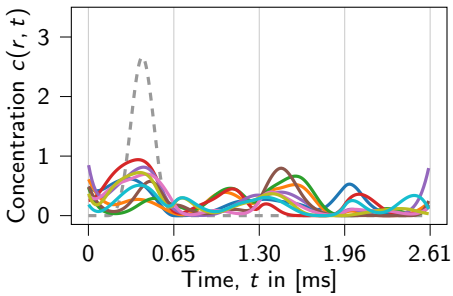

(b) Reconstruction of 1F using only S_1.

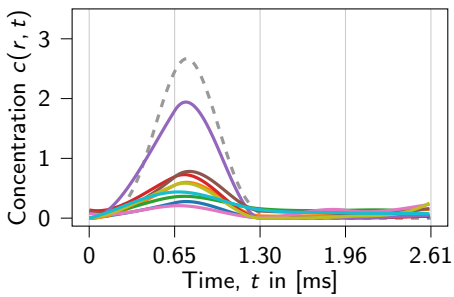

(c) Reconstruction of 2F with the dynamic model using S_1 and S_2.

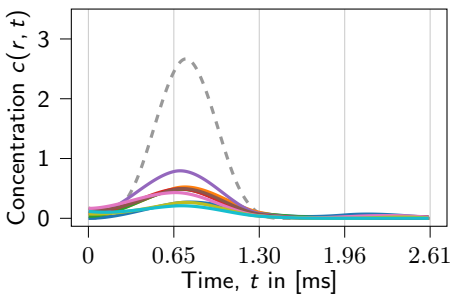

(d) Reconstruction of 2F using only S_1.

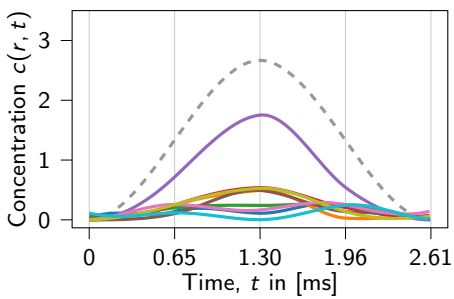

(e) Reconstruction of 4F with the dynamic model using S_1 and S_2.

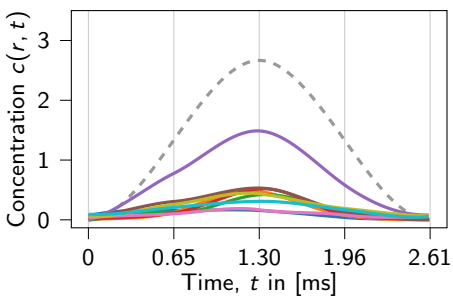

(f) Reconstruction of 4F using only S_1.

Figure 6.9.: Measurements of the dynamic one-peak phantom with 30% noise reconstructed with and without S_2.

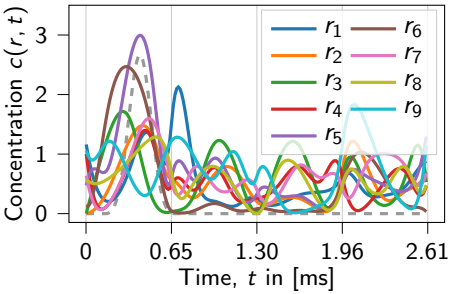

(a) Reconstruction of 1F with the dynamic model using S_1 and S_2.

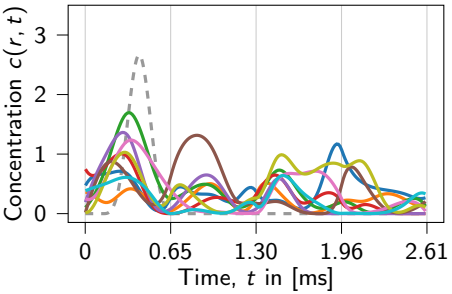

(b) Reconstruction of 1F using only S_1.

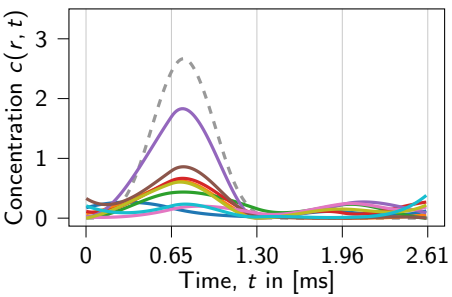

(c) Reconstruction of 2F with the dynamic model using S_1 and S_2.

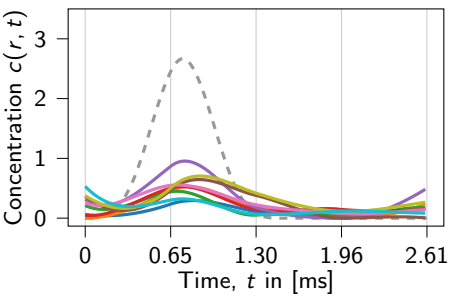

(d) Reconstruction of 2F using only S_1.

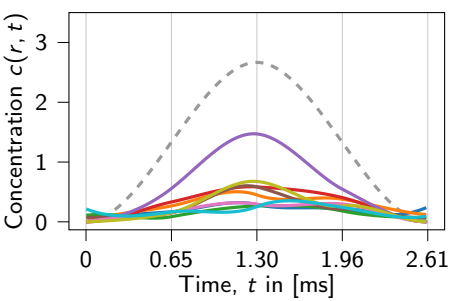

(e) Reconstruction of 4F with the dynamic model using S_1 and S_2.

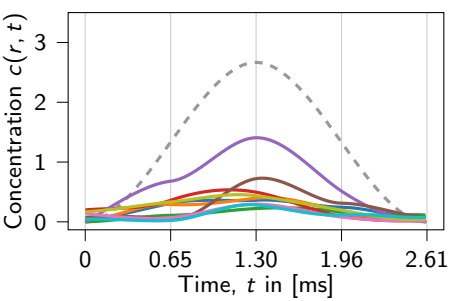

(f) Reconstruction of 4F using only S_1.

Figure 6.10.: Measurements of the dynamic one-peak phantom with 50% noise reconstructed with and without S_2.

Discussion The noise-free experiments in Section 6.1.1 show that including the second system matrix and the concentration derivative into the reconstruction process leads to superior reconstruction quality for velocities below 4.64 cm/s in a 3D setting. As the simulations use the dynamic forward model (4.7) with both matrices, it can be expected that the respective least-squares solution (6.2) performs superior to the solution of (6.3) using only S_1. Until now, the effects of actually using S_2 and $\frac{\partial \mathbf{c}}{\partial t}$ have never been investigated.
The extension of the experiments to simulated measurements with noise emphasize the initial findings. The solution of (6.3) deteriorates much faster with increasing noise levels than the solution of (6.2), while these effects are strongest for the faster phantoms with velocities over 4.64 cm/s.

6.1.3. Dynamic Frame-by-Frame Reconstruction and Noise Sensitivity

In the preceding sections, the impact of the second summand in (4.7) on reconstructions was investigated with the dynamic spline-based reconstruction method. The current state-of-the-art reconstruction method for dynamic non-periodic MPI measurements is a frame-by-frame Kaczmarz reconstruction assuming static tracer distributions within each scanning cycle. In this section, we investigate the reconstruction quality of the state-of-the-art method compared to methods based on a dynamic forward model and assumption of static concentrations within single excitation cycles.
Adapting (4.7) to concentrations which are static within one frame, yields

$$\mathbf{u}^f = \mathbf{S}_1 \mathbf{c}^f + \mathbf{S}_2 \frac{\mathbf{c}^f - \mathbf{c}^{f-1}}{\Delta t}, \qquad f = 1, \dots, F, \tag{6.5}$$

with $\mathbf{u}^f \in \mathbb{R}^{n_T}$, $\mathbf{c}^f \in \mathbb{R}^R$, $\mathbf{S}_1, \mathbf{S}_2 \in \mathbb{R}^{n_T \times R}$. Analogous to the previous experiment, we are solving (6.5) for $\mathbf{c}^f$ once with both matrices and once with the first summand only. The latter corresponds to a frame-by-frame Kaczmarz reconstruction. A dynamic single-patch phantom called *three-peak phantom* is used to simulate a dynamic measurement with different noise levels. Since the reconstruction methods in this section assume static behavior during single excitation cycles, the

dynamics of a feasible phantom are required to cover several frames. Like the one-peak phantom, the tracer distribution of the three-peak phantom is described by a cubic B-spline curve (6.1) with parameter set

$$\Lambda_B^* = \{b_{m,i} \mid b_{m,l} \geq 0,\ l \in \{4,5,6\},\ b_{m,i} = 0,\ i \in \{1,2,3,7,8,9\},\ m = 1,\ldots,M\}$$

while its spatial setup can be found in Figure 6.2. Figure 6.11a depicts the tracer distribution during the total scan time. Each curve describes the concentration within one voxel. There are three temporally shifted concentration peaks of 6.67 for voxel r_4, r_5 and r_6. Considering the location of the voxels in Figure 6.2, this dynamic can be interpreted as an object or tracer bolus moving from voxel r_4 to voxel r_6. The peaks are located in the scan time of frame 3, 4 and 5 and have a temporal width of about 4 frames. The experiments in Sections 4.3 and 6.1.1 indicate that for dynamics over at least four frames the second summand becomes less important. Thus, a comparable performance of both reconstruction methods is conjectured.

A dynamic measurement with with $F = 10$ frames, each sampled at 408 time points, is simulated according to the dynamic forward model (4.7) with S_1 and S_2. The general physical and scanner parameters are listed in Table B.1 and the phantom specific parameters can be found in Table B.2.

The dynamic tracer distribution is reconstructed with two different methods both assuming a constant tracer distribution during a scanning cycle. The first one uses information about the tracer dynamics from the reconstructions of previous frames and the second one reconstructs each frame independently. The reconstructions are piecewise constant functions over time. For better comparison the results depicted in Figure 6.11 show linear interpolations of the piecewise constant reconstructions.

In the first experiment both matrices are used for the reconstruction of each frame while the time derivative $\partial\mathbf{c}/\partial t = (\mathbf{c}^f - \mathbf{c}^{f-1})/\Delta t$ is the divided difference of the concentration vector of the current and the preceding frame. This corresponds to minimizing

$$\min_{\mathbf{c}^f} \left\| \left(\mathbf{S}_1\mathbf{c}^f + \mathbf{S}_2 \frac{\mathbf{c}^f - \mathbf{c}^{f-1}}{\Delta t} \right) - \mathbf{u}^f \right\|_2^2, \qquad f = 1,\ldots,F\,, \tag{6.6}$$

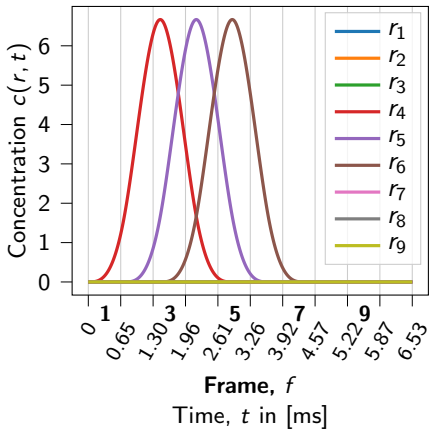

(a) The concentration of the three-peak phantom changes in time only in voxel r_4, r_5 and r_6. In the remaining voxels the concentration is zero. The time-shifted concentration peaks form a motion from r_4 to r_6.

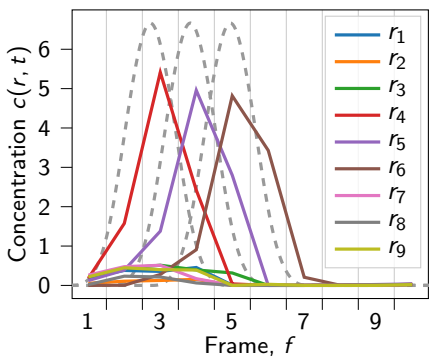

(b) Average of x- and y-channel frame-by-frame reconstructions with the dynamic model using $\mathbf{S}_1$, $\mathbf{S}_2$ without noise.

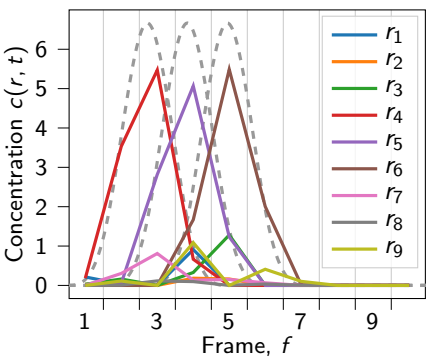

(c) Average of x- and y-channel frame-by-frame reconstructions with the static model using only $\mathbf{S}_1$ without noise.

Figure 6.11.: (Continued on the next page)

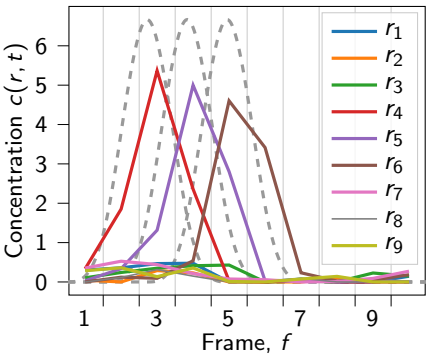

(d) Average of x- and y-channel frame-by-frame reconstructions with the dynamic model using $\mathbf{S}_1$, $\mathbf{S}_2$ with 10% noise.

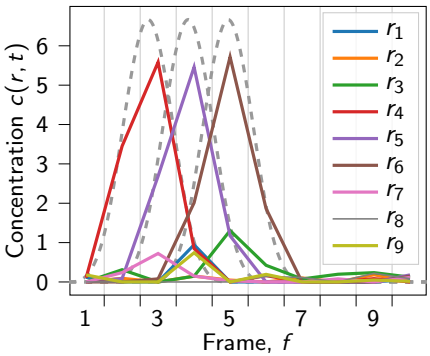

(e) Average of x- and y-channel frame-by-frame reconstructions with the static model using only $\mathbf{S}_1$ with 10% noise.

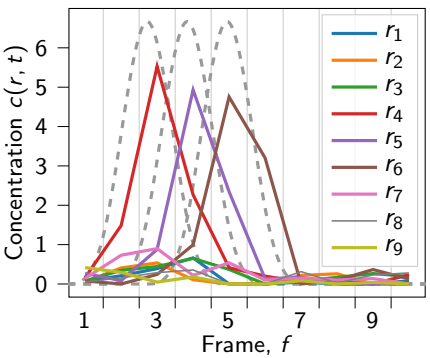

(f) Average of x- and y-channel frame-by-frame reconstructions with the dynamic model using $\mathbf{S}_1$, $\mathbf{S}_2$ with 20% noise.

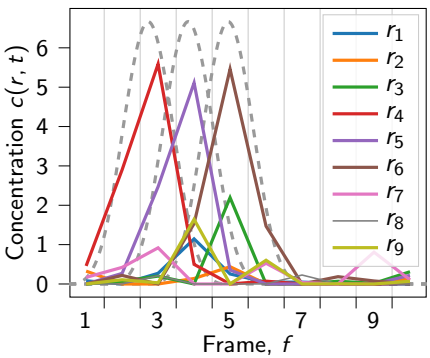

(g) Average of x- and y-channel frame-by-frame reconstructions with the static model using only $\mathbf{S}_1$ with 20% noise.

Figure 6.11.: (Continued on the next page)

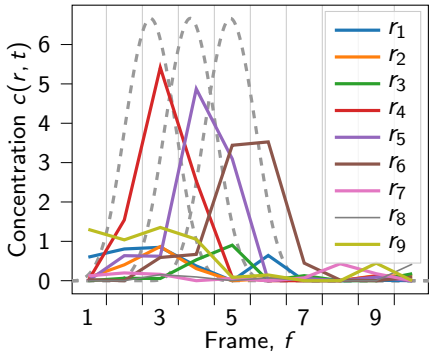

(h) Average of x- and y-channel frame-by-frame reconstructions with the dynamic model using $\mathbf{S}_1$, $\mathbf{S}_2$ with 30% noise.

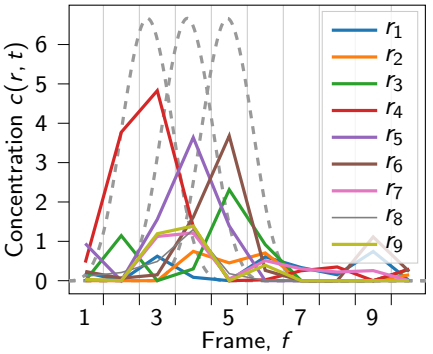

(i) Average of x- and y-channel frame-by-frame reconstructions with the static model using only $\mathbf{S}_1$ with 30% noise.

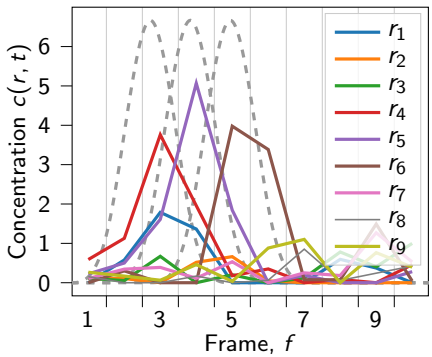

(j) Average of x- and y-channel frame-by-frame reconstructions with the dynamic model using $\mathbf{S}_1$, $\mathbf{S}_2$ with 50% noise.

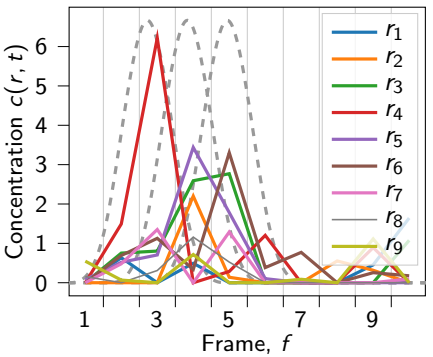

(k) Average of x- and y-channel frame-by-frame reconstructions with the static model using only $\mathbf{S}_1$ with 50% noise.

Figure 6.11.: A measurement of the dynamic three-peak phantom is simulated with the dynamic forward model (4.7) and different noise levels. Each frame is reconstructed separately assuming a static tracer distribution within each frame. The frames are reconstructed with the dynamic and the static model.

with $\mathbf{u}^f \in \mathbb{R}^{n_T}$, $\mathbf{c}^f \in \mathbb{R}^R$, $\mathbf{S}_1, \mathbf{S}_2 \in \mathbb{R}^{n_T \times R}$. Alternatively forward or central divided differences could be used while the backward differences are the easiest to implement. Figure 6.11b shows the average of x- and y-channel reconstructions which were reconstructed in time domain with 100 iterations of a gradient descent algorithm [27] and no further regularization. It can be observed that the peaks are correctly located in frame 3, 4 and 5. The amplitude of the peaks is slightly lower than the ground truth and decreasing, 5.41 for r_4, 4.96 for r_5 and 4.82 for r_6. There is a non-zero concentration for the remaining voxels in the first 5 frames of less than 0.5. So the reconstructed images will exhibit sufficient contrast.
In the second experiment the same dynamic measurement is reconstructed using only S_1, i.e. minimizing

$$\min_{\mathbf{c}^f} \left\| \mathbf{S}_1 \mathbf{c}^f - \mathbf{u}^f \right\|_2^2, \qquad f = 1, \ldots, F, \tag{6.7}$$

with $\mathbf{u}^f \in \mathbb{R}^{n_T}$, $\mathbf{c}^f \in \mathbb{R}^R$, $\mathbf{S}_1 \in \mathbb{R}^{n_T \times R}$ in time domain with 100 iterations of a gradient descent algorithm and no further regularization. This is the same minimization problem that is solved by a frame-by-frame Kaczmarz reconstruction. The result is shown in Figure 6.11c. Again, the peaks are located correctly in frame 3, 4 and 5. The amplitudes 5.47 for r_4, 5.07 for r_5 and 5.49 for r_6 are also slightly lower than in the phantom and differ less than in the first experiment. The remaining voxels show non-zero concentrations up to 1.2 being more than twice as high as for the first experiment.
In a third experiment, the two reconstruction methods were applied to noisy data simulated with noise model (6.4) and noise level $\delta \in \{10, 20, 30, 50\}\%$. The results can be found in Figures 6.11d to 6.11k. The reconstructions for 10% and 20% noise are very good for both methods. The main peaks do not change significantly by increasing the noise level. Only the concentration for the remaining voxels begins to differ more from zero for 20% noise. For the high noise levels 30% and 50%, the main peaks become smaller, the three peaks differ more in their height and the concentration of the remaining voxels increases further. Thus, the contrast will decrease and the correct motion will not be recognizable anymore.

Discussion As suspected, the two methods perform equally well on a phantom with motion covering 4 frames. They yield reconstructions of similar quality and are both robust to low noise levels. This confirms that under the assumption of slow velocities, the second term in (4.4) can indeed be neglected (e.g. in [25]) and a frame-by-frame Kaczmarz reconstruction suffices.

6.2. Computational Phantom Studies with Single- and Multi-Patch Phantoms

In this section, we validate our dynamic reconstruction method using computational phantoms. The experiments in the beginning of this chapter used phantoms with minimal spatial resolution to keep the computational costs low and focus on the temporal development. Now, the spatial resolution and the number of affected voxels are increased to get closer to real life applications. Dynamic measurements from two phantoms with fast non-periodic motion are simulated and reconstructed with the dynamic multi-patch reconstruction method (5.2) and the Kaczmarz algorithm. The first phantom discussed in Section 6.2.1 shows one moving object and is scanned in a single-patch scan. The second phantom, covered in in Section 6.2.2, is scanned in a multi-patch sequence and shows two objects moving in parallel each within one patch. The parameters of the reconstruction algorithms

Table 6.1.: Reconstruction algorithm parameters

Phantom	**Single-patch**		**Multi-patch**	
Reconstruction	dynamic	static	dynamic	static
Algorithm	CG	Kaczmarz	CG	Kaczmarz
Number of iterations	20	50	20	50
γ	0.15	0.1	0.3	0.1
M_0	5	-	5	-

applied in this section are listed in Table 6.1, while all regularization parameters were determined by visual inspection. We point out that experiments with the same setup as in Section 6.2.1 as well as the experiments and results in Sec-

tion 6.2.2 have already been published in [12].
Compared to mean blood flow velocities in the human body, the velocities of the phantoms in this section might appear very high. This can be explained by the simulation setup using only one repetition per patch and a switching time of zero seconds. The phantoms are designed to show an object that moves through its patch within the total scan time of four frames and the respective number of patches. Assuming a realistic scenario, a 3D scan might require six repetitions per patch and a switching time of four cycles to shift the focus field. In the case of $F = 4$ frames, $P \in \{1, 2\}$ patches with a FOV size of $24 \times 24 \times 1$ mm^3, using

$$v_P = \frac{\Delta x}{PF(6+4) \cdot T_c^{3D}} \qquad \text{with } T_c^{3D} = 21.54 \text{ ms} \tag{6.8}$$

yields speeds of $v_1 = 2.8$ cm/s and $v_2 = 1.4$ cm/s. Considering the blood flow velocities listed in Table 6.2 it becomes clear that these velocities are in fact already reached in human arterioles and venules.

Table 6.2.: Velocities in human vessels [24]

Vessel	**Diameter [cm]**	**Mean velocity [cm/s]**
Aorta	3	12
Vena cavae	3	14
Arteries	10^{-1}	45
Veins	$1.8 \cdot 10^{-1}$	10
Arterioles	$5 \cdot 10^{-3}$	5
Venules	10^{-2}	2
Capillaries	$8 \cdot 10^{-4}$	0.1

6.2.1. Dynamic Single-Patch Reconstruction

The *dynamic single-patch phantom* is a computational phantom which is shown at eight time points in the left column of Figure 6.13. It exhibits a box of size $6 \times 12 \times 1$ mm^3 with a non-zero concentration. It moves linearly in x with a velocity of 7.28 m/s. The temporal concentration development is described by a cubic spline curve. So, the concentration increases and decreases smoothly with

a maximum of 3. Figure 6.12a shows the concentration over time with each line describing the concentration of one voxel.
A dynamic single-patch scan over $F = 4$ frames is simulated using model (4.7) and the parameters enumerated in Tables B.1 and B.3. We reconstruct the data with dynamic and static methods. In the first experiment, problem (5.2) with regularization term

$$\mathcal{R}(\Lambda_B) = \frac{1}{2} \sum_{p=1}^{P} \sum_{m \in M_p} \sum_{i=1}^{R} b_{m,i}^2 \tag{6.9}$$

and parameter $\gamma = 0.15$ is minimized with 20 iterations of a conjugate gradient algorithm. We use the spline setup from Section 5.4 with $M_0 = 5$ to achieve the same spline basis as in the phantom. While the phantoms in the preceding sections could be reconstructed without spatial regularization due to their extremely low number of voxels, we now add a penalty term on the spline coefficients. Thus, the problem is regularized by Tikhonov regularization and implicitly by the dynamic concentration model. Figure 6.12c shows the reconstructed concentration curves for each voxel. In the second experiment a static frame-by-frame method is used. Each frame of the simulated dynamic measurement is reconstructed is reconstructed as a static image with 50 Kaczmarz iterations and Tikhonov regularization with $\gamma = 0.1$. As early abortion of the iteration introduces an additional regularization, the number of Kaczmarz iterations is chosen unusually high [45]. A linear interpolation of the reconstructed concentration curves for each voxel is shown in Figure 6.12e.
Since the overlay of 100 curves is challenging to interpret, we show the concentration curves for the phantom and both reconstructions for a selection of voxels in Figures 6.12b, 6.12d and 6.12f. The selected voxels are located on the line at $y = -3$ mm and are marked by the red x-es in the first image in Figure 6.13. The color coding in the concentration curves is the same so that curves with the same color represent the same position in all three plots. It can be observed that the location of the peaks is approximately correct in both reconstructions, while their height is slightly underestimated in the dynamic reconstruction and overestimated in the static reconstruction. The frame-by-frame reconstruction obviously suffers

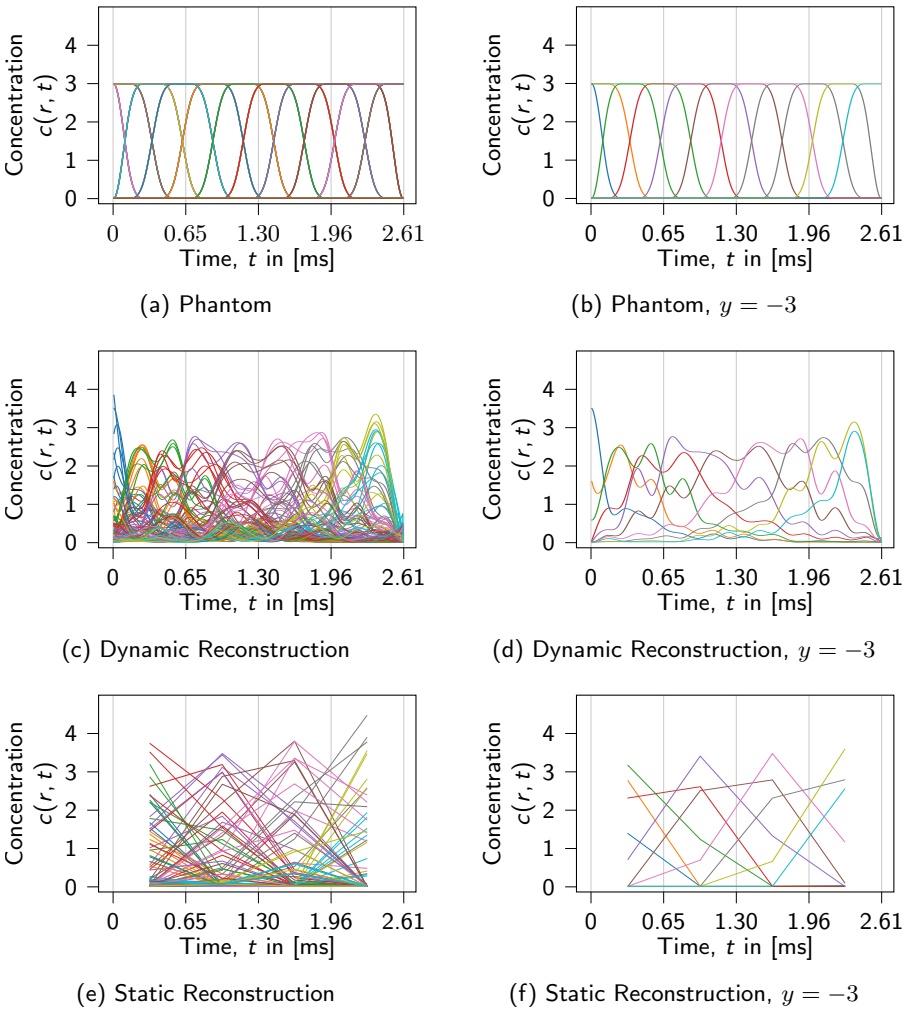

(a) Phantom

(b) Phantom, $y = -3$

(c) Dynamic Reconstruction

(d) Dynamic Reconstruction, $y = -3$

(e) Static Reconstruction

(f) Static Reconstruction, $y = -3$

Figure 6.12.: Dynamic single-patch simulation. The tracer concentration over time for each voxel is shown for the phantom, the dynamic reconstruction and a linear interpolation of the static reconstruction. The grid lines mark the end of the scanning interval of a frame. Figures 6.12a, 6.12c and 6.12e show the concentration for all voxels, while Figures 6.12b, 6.12d and 6.12f show the concentration for the voxels at $y = -3$ mm marked by the red x-es in Figure 6.13.

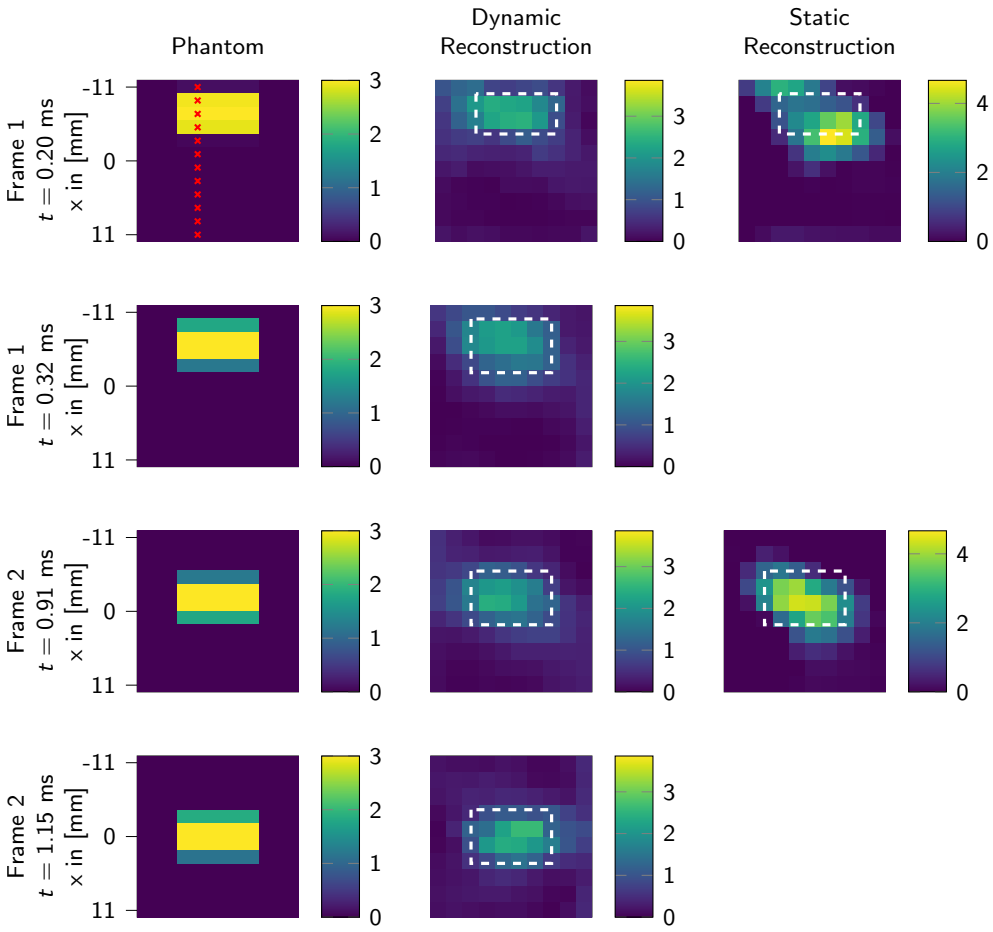

Figure 6.13.: (Continued on the next page)

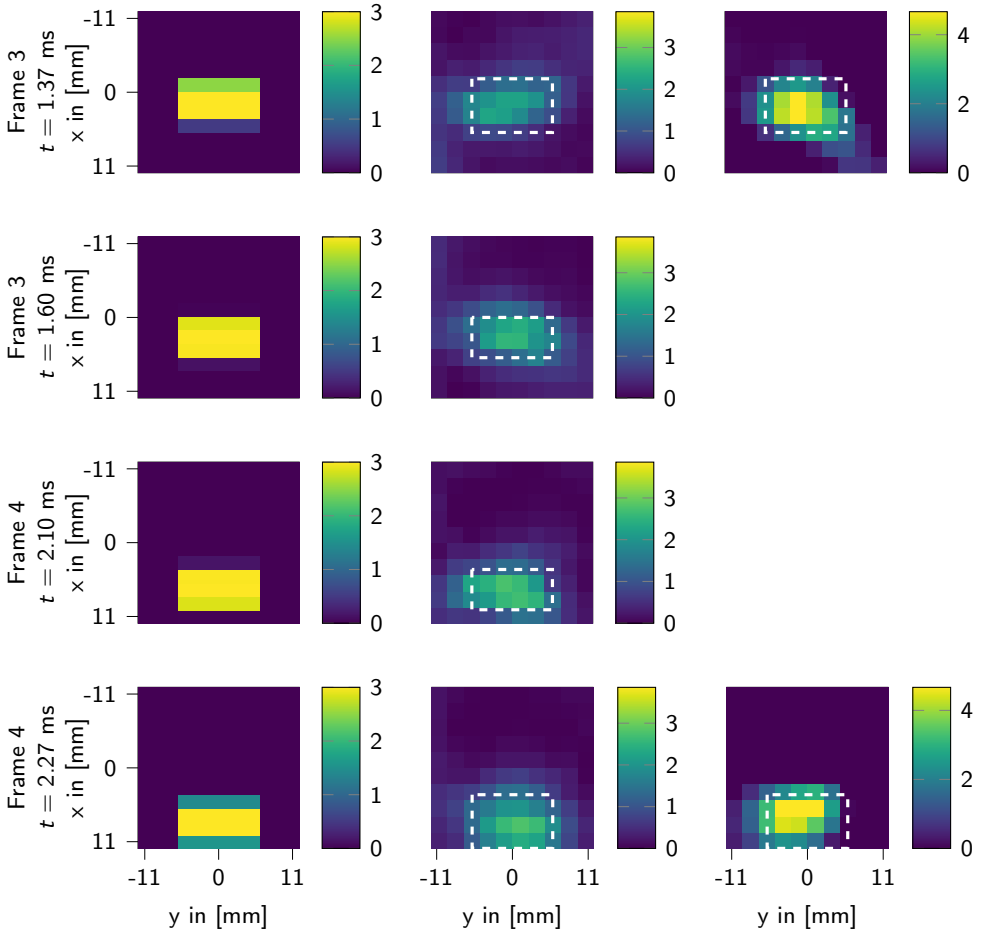

Figure 6.13.: Dynamic single-patch simulation. The continuous tracer distribution of the phantom (left column) and the dynamic reconstruction (central column) is shown at 2 time points of each of the 4 frames. The 4 frames reconstructed with the static frame-by-frame method are shown in the right column. The dashed white box shows the outlines of the phantom at the respective point of time. The red x-es mark the set of voxels studied in Figures 6.12b, 6.12d and 6.12f.

from its lower temporal resolution.
A more intuitive visual inspection of the reconstruction quality can be made by comparison of selected frames shown in Figure 6.13. It depicts the dynamic reconstruction at 8 time points and the 4 frames of the static reconstruction. A slightly lower intensity of the box compared to the phantom can be observed in the dynamic reconstruction. While the outline of the box is blurred, it is located correctly in all frames. In accordance with the concentration curves, the static reconstruction yields boxes with higher concentration values compared to the phantom. While the box is located almost correctly in x-position, it shows severe motion artifacts in form of diagonal smearing. The boxes have sharper edges and better contrast than in the dynamic reconstruction but the rectangular outlines are vanished.
For a more objective assessment of the reconstruction quality, we computed the mean squared error (MSE)

$$\mathrm{MSE}(t) = \frac{1}{R}\sum_{i=1}^{R}\left(c^{\mathrm{phant}}(r_i,t) - c^{\mathrm{reco}}(r_i,t)\right)^2 \tag{6.10}$$

for each time point for the dynamic and static reconstruction, visible in Figure 6.19a. The mean and variance values of the MSE are listed in Table 6.3. The MSE of the dynamic reconstruction oscillates around its mean MSE of 0.049 with a relatively small variance of $2.25 \cdot 10^{-5}$. The mean MSE for the static reconstruction is 0.058 and thus slightly higher, while showing a significantly larger variance of $1.23 \cdot 10^{-4}$. The error shows a wave structure with local minima in each frame. This can be explained with the fact that at some point in the scanning cycle of each frame, the static reconstruction is close to the true position of the box. In the middle of frame two and three the error is even lower than for the dynamic reconstruction.
A benefit of the spline-based reconstruction method is that the reconstruction of the B-spline coefficients allows to jointly reconstruct the concentration and its temporal derivative. The change rates of the phantom concentration and the dynamic reconstruction are illustrated in Figure 6.14 for the selection of voxels. As the color coding of the curves is the same, one can observe that e.g. for the

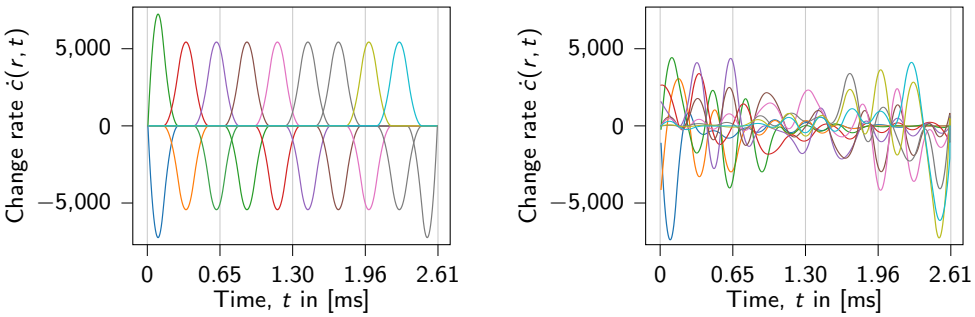

(a) Phantom (b) Dynamic Reconstruction

Figure 6.14.: Change rates of the concentration for the voxels at $y = -3$ mm

dark blue line the curve is reconstructed correctly while many others show false oscillations. For a more intuitive illustration, derivative images at time point $t = 0.32$ ms are depicted in Figure 6.15 for the phantom and the reconstruction. The corresponding concentration images can be found in the second row of Figure 6.13. In this frame the derivative is reconstructed quite well. There is a thin rectangular region with large negative change rates of about -3000 and a nearly rectangular region with large positive change rates of about 4000. The values in the phantom are ± 5000. While the strength of the concentration change is underestimated, the region of strong changes is located very well.

Discussion Visual inspection of the concentration curves and the frames does not clearly show a superior reconstruction quality of the new method. The static reconstruction shows better contrast while the dynamic reconstruction is able to follow the movement of the box more precisely due to its high temporal resolution. This is also supported by the analysis of the reconstruction error which is lower for the dynamic reconstruction on average but not for all time points. The strength of the new approach in this example lies above all in the high temporal resolution and the reduced motion artifacts compared to the static approach.
Additionally, the dynamic reconstruction method jointly reconstructs the time derivative of the concentration which is an interesting feature for applications like blood flow analysis. In accordance with the reconstructed concentration,

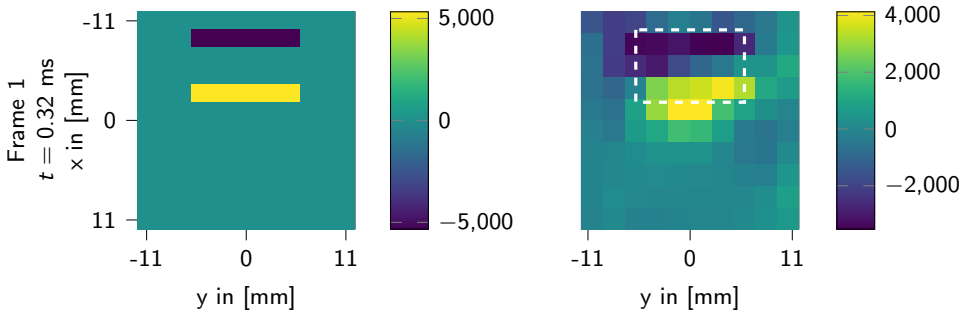

(a) Phantom

(b) Dynamic reconstruction

Figure 6.15.: Concentration change rates at time point $t = 0.32$ ms shown as 2D images. The dynamic reconstruction method jointly reconstructs the temporal derivative of the concentration.

the reconstruction quality of the derivative is not optimal but the localization of regions with strong change rates is satisfactory. The underestimation of the strength of the change rate corresponds to the absence of sharp edges in the reconstructed concentration, as a blurred moving box causes minor concentration changes over time.

6.2.2. Dynamic Multi-Patch Reconstruction

In this section, we use the *dynamic multi-patch phantom* that consists of two boxes of size $4.5 \times 9 \times 0.75$ mm^3 with a non-zero concentration which move linearly in x with a velocity of 6.36 m/s. The FOV covers two patches aligned in y. Each box is located in the central y position of one of the patches. Eight time points of the phantom are shown in the left column of Figure 6.17. Just as with the dynamic single-patch phantom, the maximum concentration in a voxel is 3 and the temporal behavior of the concentration is described by a cubic spline curve such that there is a smooth increase and decrease of the concentration. The concentration for a selection of voxels in patch 1 over time where each line describes the concentration of one voxel can be seen in Figure 6.16a. Since the movement is the same in both patches, the curves for patch 2 look identical. The selected

voxels lie on the line at $y = -2$ mm and are marked by red x-es in the first image in Figure 6.17.
A dynamic multi-patch measurement with $F = 4$ frames is simulated using model (4.7) and the parameters enumerated in Tables B.1 and B.3. An overscan [84] is omitted to simplify the imaging sequence.

Again we run two experiments, a dynamic and a static frame-wise reconstruction. First, we minimize problem (5.2) with regularization (6.9) and parameter $\gamma = 0.3$ with 20 iterations of a conjugate gradient descent algorithm. The spline setup presented in Section 5.3 is used with $M_0 = 5$ in order to obtain a good approximation of the velocities in the phantom. Choosing a lower value would increase the distance of the knots resulting in basis splines with larger support. Hence, the maximum speed that can be reconstructed would be limited. Figure 6.16b shows the reconstructed concentration over time for the selected voxels with $y = -2$ mm.
Second, we reconstruct the dynamic multi-patch measurement with the static frame-by-frame method. Each patch of the four frames is reconstructed under the assumption of static behavior with 50 Kaczmarz iterations and Tikhonov regularization with $\gamma = 0.1$. Linearly interpolated concentration curves for the voxels with $y = -2$ mm are shown in Figure 6.16c. The curves in the three plots have the same color coding so that curves with the same color represent the same voxel in all three plots.
The maxima in the dynamic reconstruction exhibit values of $2 - 3$. Especially the orange and blue lines are close to ground truth. As expected, the static reconstruction suffers from a low temporal resolution. Nevertheless, the peaks of the purple, light green and light blue lines are located correctly in time and reach values of about 3. The blue and orange line, however, are showing significantly lower concentration values compared to the phantom.
For further analysis of the reconstruction quality, we show the the phantom and the dynamic reconstruction at 8 time points in Figure 6.17 and the 4 frames of the static reconstruction in Figure 6.18. With values of about $2 - 3.5$, the concentration values in the dynamic reconstruction are close to ground truth. As in the single-patch reconstructions in the previous section, the outlines of the boxes are blurred. The boxes are located correctly not only in y but also in x.

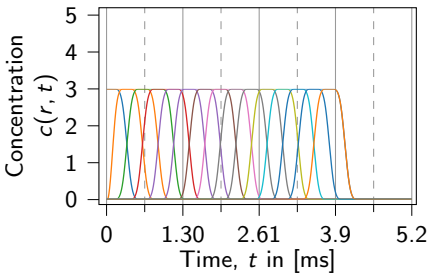

(a) Phantom

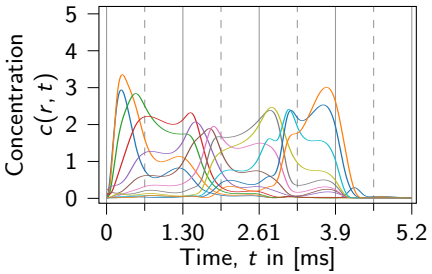

(b) Dynamic Reconstruction

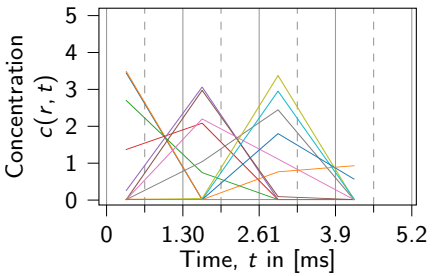

(c) Static Reconstruction

Figure 6.16.: Dynamic multi-patch simulation. The tracer concentration over time is shown for the phantom, the dynamic and static reconstruction. Each curve shows the concentration in a voxel at $y = -2$ mm marked by the red x-es in Figure 6.17. Figure 6.16c shows a linear interpolation of the 4 statically reconstructed frames.The dashed grid lines mark the end of a scanning interval of a patch and the solid lines mark the end of a scanning interval of a frame.

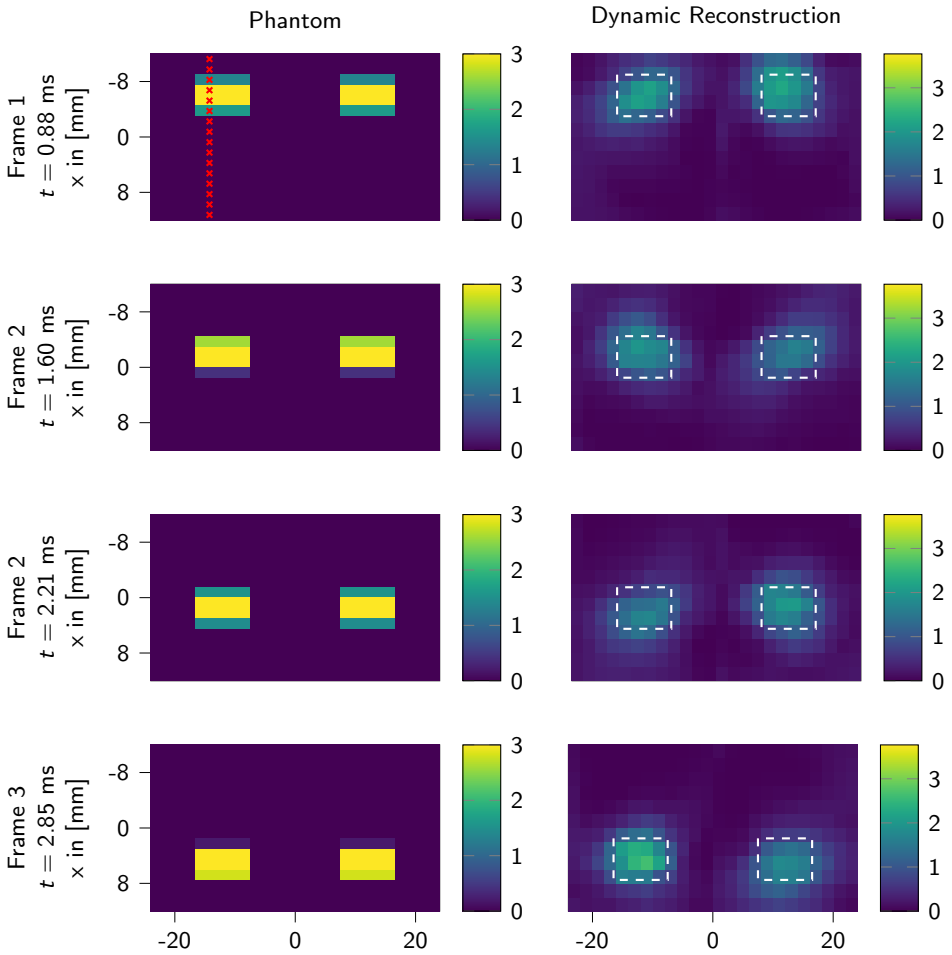

Figure 6.17.: (Continued on the next page)

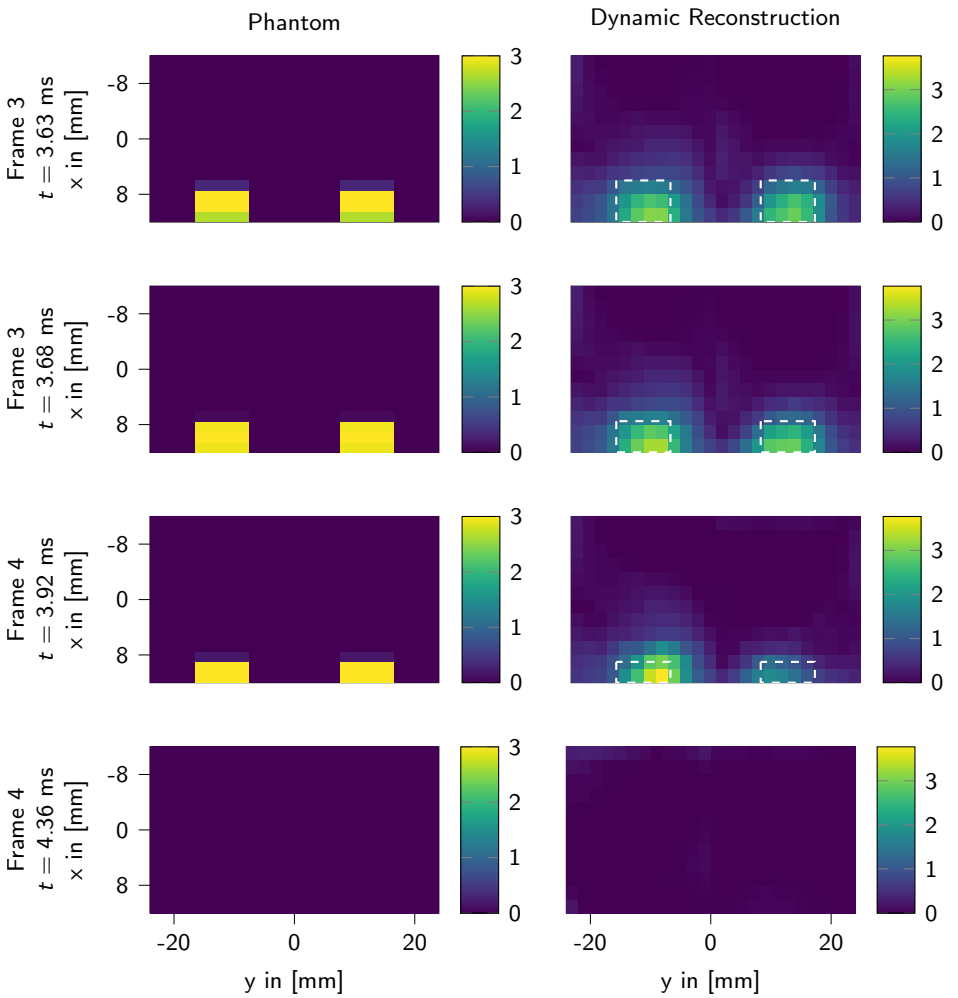

Figure 6.17.: Dynamic multi-patch simulation. The continuous tracer distribution of the phantom (left column) and the dynamic reconstruction (central column) is shown at 8 time points. The dashed white boxes show the outlines of the phantom at the respective point of time. The red x-es mark the set of voxels studied in Figure 6.16.

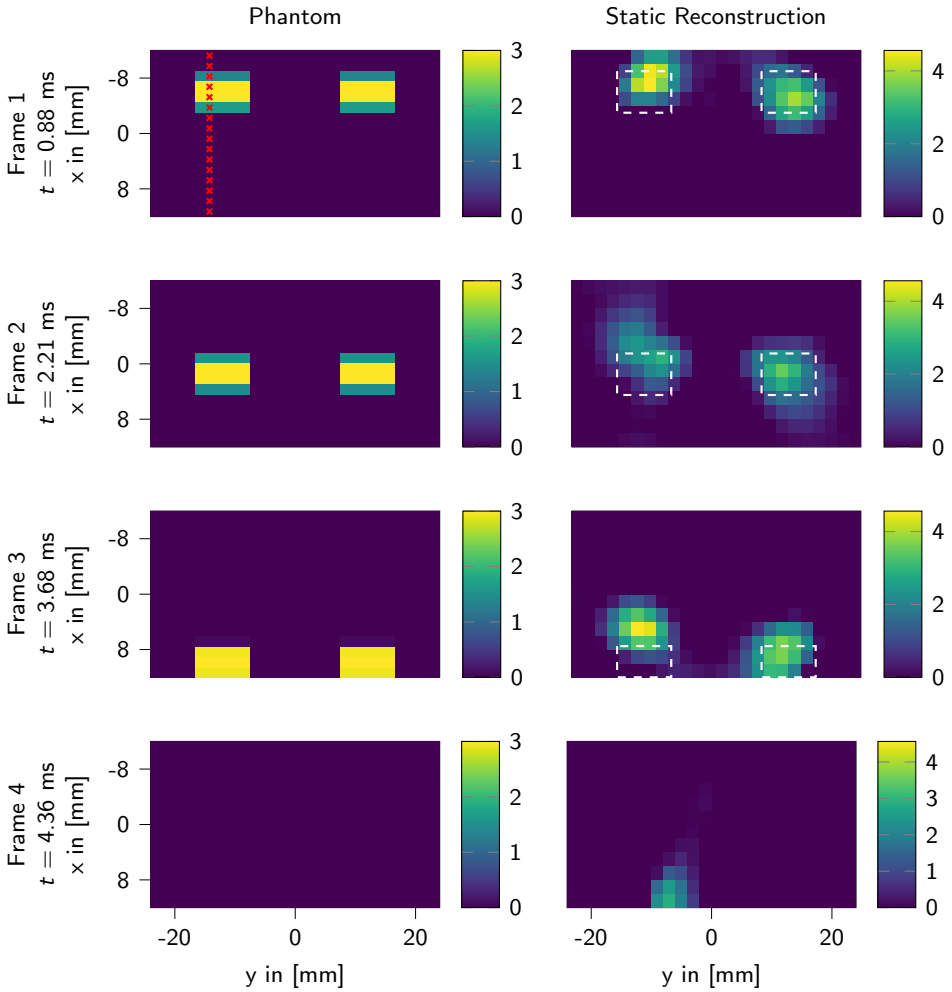

Figure 6.18.: Dynamic multi-patch simulation. The tracer distribution of the phantom is shown at 4 time points in the left column and the corresponding 4 frames reconstructed with the static frame-by-frame method in the right column. The dashed white boxes show the outlines of the phantom at the respective point of time. The red x-es mark the set of voxels studied in Figure 6.16.

The algorithm is indeed able to reconstruct the boxes' parallel movement. In the static reconstruction, the boxes show concentration values of 4 which is slightly higher than in the phantom. The boxes show slightly better contrast than in the dynamic reconstruction but exhibit motion artifacts in form of diagonal smearing. Additionally, multi-patch artifacts can be observed. The location of the boxes is shifted in x due to the different time points of the scans of the individual patches, which was expected and discussed in Section 5.1.
In addition to the visual inspection of reconstructed frames and concentration curves, we analyze the mean squared error (6.10) for each time point for the dynamic and static reconstruction which is plotted in Figure 6.19b. The mean and variance values of the MSE are listed in Table 6.3. The MSE of the dynamic reconstruction is lower for all time points and its mean MSE of 0.019 is 32% smaller than in the static case.
As the boxes disappear from the FOV in the last frame, which is captured correctly in both experiments, a significant drop of the MSE can be observed. Thus, we focus on the variance within the first three frames. The MSE of the dynamic reconstruction oscillates around its mean with a small variance of $1.97 \cdot 10^{-6}$. The MSE of the static reconstruction exhibits a wave shape with local minima at the transitions from the first patch to the second. With $2.18 \cdot 10^{-5}$, the variance is an order of magnitude larger than in the dynamic case. The pattern corresponds to the trade-off that the error in each patch increases with the temporal distance to its scan time. While one patch is scanned and can be reconstructed with a low MSE, motion in the other patch has not yet been included in the reconstruction and causes a larger MSE. These effects are balanced at the transition between the patches.

Discussion While the dynamic reconstruction is affected by blurring, the advantages of this new method become evident. Displacement artifacts are compensated and motion artifacts reduced compared to the static reconstruction. The visual impression is confirmed by the error metric. To be a valid alternative in practice, the blurring should be reduced by further regularization. Furthermore, the high temporal resolution comes at the cost of a high computational complexity. This might be alleviated by finding more efficient minimization methods.

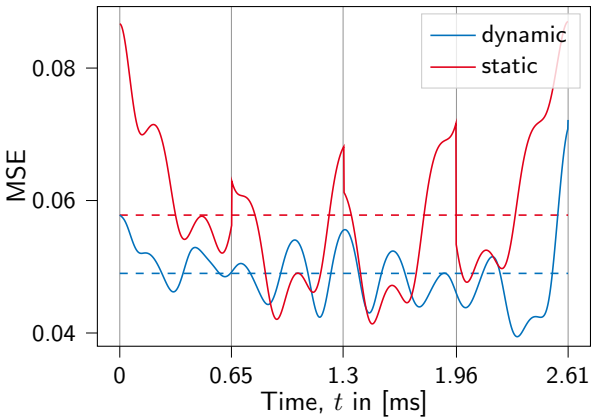

(a) MSE of the dynamic single-patch phantom and its mean (dotted line).

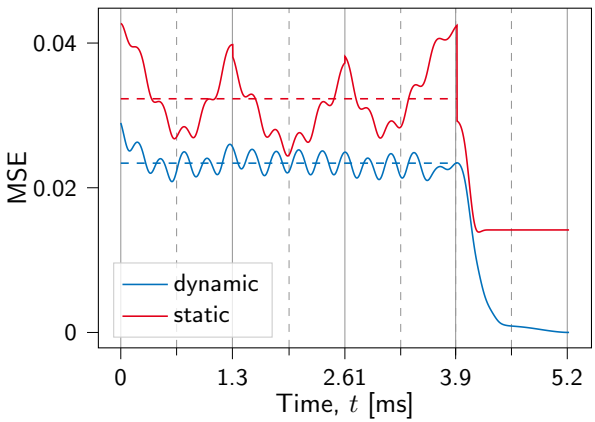

(b) MSE of the dynamic multi-patch phantom and its mean over the first three frames (dotted line).

Figure 6.19.: Reconstruction error over time.

Table 6.3.: Mean and variance of the MSE (within the first three frames)

Reconstruction	**Single-patch phantom**	**Multi-patch phantom**
Mean of MSE		
Dynamic	0.049	0.019 (0.023)
Static	0.058	0.028 (0.032)
Variance of MSE		
Dynamic	$0.225 \cdot 10^{-4}$	$8.108 \cdot 10^{-5}$ $(0.197 \cdot 10^{-5})$
Static	$1.227 \cdot 10^{-4}$	$7.222 \cdot 10^{-5}$ $(2.177 \cdot 10^{-5})$

7. Conclusion

7.1. Summary

In the beginning of this thesis, we gave an introduction to inverse problems and the principles of magnetic particle imaging where we discussed the current state of research and the challenges in solving dynamic inverse problems as well as the issues specific to magnetic particle imaging in the single and multi-patch case. Especially the high number of degrees of freedom and the data gaps in multi-patch scans due to sequential scanning were highlighted.
Since the standard model does not account for dynamic tracer distributions, we proceeded with an extended forward model for dynamic tracer distributions. The evaluation of the influence of the newly introduced second summand with the second system matrix showed that for low concentration values and fast change rates the order of magnitude of the two summands is the same.
In order to find an alternative reconstruction method to static frame-by-frame approaches that is not limited to low velocities or specific motion patterns, we investigated the data structure of dynamic multi-patch measurements. As a consequence, a new dynamic reconstruction approach based on a spline model for the concentration and the new forward model was introduced.
Finally, a set of experiments was conducted to highlight the relevance of the new method. First, measurements from synthetic dynamic concentrations were simulated with the dynamic model and then reconstructed once with both system matrices and once using only S_1. Three simple phantoms with different change rates were examined. For one-peak 4F, the phantom with the lowest change rates, the static approach using only one system matrix provided an acceptable reconstruction quality. For the phantoms with higher change rates, one-peak phantom 2F and 1F, the static approach resulted in reconstructions with low contrast and

significantly lower amplitudes than ground truth while the dynamic approach performed well on all three phantoms. These reconstructions were obtained with the spline-based method.
Second, a dynamic measurement from another phantom, the three-peak phantom, was simulated. The change rates were slower and more frames were scanned to enable a frame-by-frame reconstruction with one and two system matrices. Due to the low change rates the frame-by-frame approach was able to deliver compatible results.
Third, the experiments with one-peak phantom 1F, 2F, 4F and the three peak phantom were repeated with noisy measurements with different noise levels. With increasing noise the reconstruction quality degraded for both methods but the dynamic method with S_1 and S_2 was much more robust to noise. Even for 30% noise its performance on the one-peak phantoms was very good.
Fourth, the dynamic reconstruction method was evaluated on more complex dynamics. A single and a multi-patch phantom with linearly moving boxes were used for synthetic measurements and reconstructed with the dynamic reconstruction method and a frame-by-frame Kaczmarz reconstruction. The latter reconstructed 4 frames exhibiting motion artifacts and in the multi-patch case additional displacement artifacts. The dynamic reconstruction method resulted in slightly blurred boxes with few motion artifacts and reduced displacement artifacts compared to the static approach. It produced a dynamic concentration sampled at $408 \cdot 4$ in the single and $408 \cdot 2 \cdot 4$ time points in the multi-patch case.

7.2. Discussion

We have shown that for certain velocities and concentrations levels the proposed dynamic reconstruction method performs superior to the standard method. Its general formulation does not limit it to applications with specific motion patterns or low velocities. Moreover, more sophisticated magnetization models can be included alternatively to the equilibrium model used in this thesis. The dynamic concentration model limits the degrees of freedom such that the dynamic reconstruction method already includes an implicit regularization which can be extended with additional spatial or temporal regularization, like sparsity in time

and space. Furthermore, the method allows for joint reconstructions of the particle concentration and its time derivative, a beneficial feature for blood-flow analyses. The experiments with small dynamic phantoms and different noise levels show a higher robustness against noise for the dynamic reconstruction methods which becomes even more evident with increasing velocities. We point out that in the experiment with the one-peak phantom reconstructions with the true forward operator are compared with reconstructions with a simplified forward operator, the one using only S_2. Thus, a better performance of the former was expected. Nevertheless, the experiments with the one- and three-peak phantom show that for velocities over 4.64 cm/s, the dynamic model should be considered. For slower movements, a frame-wise Kaczmarz reconstruction will suffice.
The simulation studies with larger dynamic phantoms show that both the static and the dynamic method are able to reconstruct dynamic tracer distributions with high velocities from single and multi-patch data. While the boxes in the dynamic reconstructions are blurred, motion artifacts are reduced compared to the static frame-by-frame reconstructions for both phantoms. In the multi-patch case, the dynamic reconstruction approach compensates displacement artifacts that can be clearly observed in the frame-wise Kaczmarz reconstruction. Correspondingly, the MSE of the dynamic reconstruction is below the the MSE of the static reconstruction for all time points. In the single-patch case, the superiority of the dynamic method is less obvious by visual inspection and is confirmed by the MSE. The mean squared error of the dynamic reconstruction is lower than for the static reconstruction on average and for most time points. The error metric indicates that the advantages of the dynamic reconstruction method become more evident in the case of fast dynamics during multi-patch sequences than in the single-patch case. Another benefit of the new reconstruction method is its high temporal resolution. Due to the cubic spline model the reconstructed tracer distributions are temporally smooth.
The price for the named benefits is a higher complexity and thus a longer computation time. At this stage of development, the method has not yet been optimized in terms of speed and memory consumption. A temporal splitting as in existing real-time methods might be an option. Making use of the finite support of the basis splines, the data can be split in time. The intervals can then be reconstruc-

ted sequentially with the associated set of B-splines (see Lemma 5.4).
Another useful extension, which was neglected in this thesis, would be the inclusion of overscans. Magnetic nanoparticles that are outside the FOV but close to a drive field trajectory can cause a signal which cannot to be assigned to a unique location. These artifacts can be reduced by choosing a larger FOV for the system matrix. In multi-patch sequences overlapping drive field FOVs can be used to achieve consistent reconstructions along the patch borders. The above-named artifacts affect mostly particles close to the patch borders. As this thesis focuses on the artifacts from different scanning intervals of the patches, we ensured the absence of these border artifacts in the simulations. Including the respective compensation strategies into the simulation and reconstruction framework is possible and remains future work.
We tried to evaluate our reconstruction method on experimental data. As dynamic multi-patch reconstruction is still an emerging field of research, suitable data sets have been very rare. We acquired dynamic multi-patch data sets with the preclinical Bruker MPI system at UKE. Unfortunately, the planned measurement setup could not be realized due to the system protocols such that the measured data set became quite large. Until the completion of this thesis, we were not able to produce acceptable dynamic reconstructions from these data sets.
The choice of options and parameters to determine when reconstructing experimental data is vast. One option already discussed in Chapter 4, is whether to reconstruct in time or frequency domain. On the one hand, most processing steps to improve the signal-to-noise ratio are done in frequency domain. So it seems natural to accept the increased computational costs due to the convolutions and memory requirements caused by a frequency space reconstruction. On the other hand, the convolution theorem of the Fourier transform is used in fast convolution methods anyway. Thus, transforming the processed data back to time domain poses a valid alternative.

7.3. Conclusion and Outlook

The new dynamic reconstruction method together with the dynamic forward model successfully reduces displacement and motion artifacts in dynamic non-

periodic multi-patch MPI reconstructions. Nevertheless, there are still many directions of potential improvement and the general formulation of the method allows for numerous extensions. The experiments to determine the influence of the second summand in relation to the level of dynamics should be extended to a quantitative study of phantoms with different velocities. This might allow for a proposition about when the dynamic model is necessary based on the level of dynamics and the desired reconstruction quality. A more theoretical research direction of interest is the analysis of the ill-posedness of the dynamic reconstruction problem including the concentration model. The method should be evaluated on more complex synthetic phantoms of realistic size as well as on physical phantoms. This motivates the search for faster reconstruction techniques for large 4D-volumes. In the case of reconstructions from experimental data, possible combinations of measured and modeled system matrices can be evaluated. E.g. system matrix S_1 can be used together with a modeled and transfer function corrected system matrix S_2 or might be determined from S_1 with machine learning methods. The blurring observed in the reconstructions in Section 6.2 despite the use of regularization methods is not yet fully understood and needs to be investigated in detail. Additionally, further regularization e.g. in space or with different norms, should be tested. While currently the spatial patch arrangement is completely arbitrary, the knowledge of the patch positions and the inclusion of overlapping patches will improve the reconstruction quality in practice. Moreover, replacing the equilibrium model by more advanced magnetization models will be very interesting direction of research. Also the replacement of splines by other basis functions like wavelets or shearlets is a promising extension of this work.
All in all, the presented method must be subjected to further studies to gain impact in clinical applications. The field of dynamic inverse problems and dynamic MPI reconstruction has gained more attention in the last years and will stay a popular research topic. Our approach to approximate the missing data in multi-patch sequences will gain importance with increasing number of patches or repetitions per patch which can be expected in clinical applications.

Bibliography

[1] M. Ahlborg, C. Kaethner, T. Knopp, P. Szwargulski, and T. M. Buzug. Using data redundancy gained by patch overlaps to reduce truncation artifacts in magnetic particle imaging. *Physics in Medicine & Biology*, 61(12):4583, 2016.

[2] A. C. Bakenecker, A. von Gladiss, H. Schwenke, A. Behrends, T. Friedrich, K. Lüdtke-Buzug, A. Neumann, J. Barkhausen, F. Wegner, and T. M. Buzug. Navigation of a magnetic micro-robot through a cerebral aneurysm phantom with magnetic particle imaging. *Scientific reports*, 11(1):1–12, 2021.

[3] I. M. Baltruschat, P. Szwargulski, F. Griese, M. Grosser, R. Werner, and T. Knopp. 3d-smrnet: Achieving a new quality of MPI system matrix recovery by deep learning. In *International Conference on Medical Image Computing and Computer-Assisted Intervention*, pages 74–82. Springer, 2020.

[4] C. Bathke, T. Kluth, C. Brandt, and P. Maaß. Improved image reconstruction in magnetic particle imaging using structural a priori information. *International Journal on Magnetic Particle Imaging*, 3(1), 2017.

[5] L. M. Bauer, S. F. Situ, M. A. Griswold, and A. C. S. Samia. High-performance iron oxide nanoparticles for magnetic particle imaging–guided hyperthermia (hMPI). *Nanoscale*, 8(24):12162–12169, 2016.

[6] C. P. Bean and J. D. Livingston. Superparamagnetism. *Journal of Applied Physics*, 30(4):S120–S129, 1959.

[7] S. E. Blanke, B. N. Hahn, and A. Wald. Inverse problems with inexact forward operator: iterative regularization and application in dynamic imaging. *Inverse Problems*, 36(12):124001, 2020.

[8] M. Boberg, T. Knopp, and M. Möddel. Reducing displacement artifacts by warping system matrices in efficient joint multi-patch magnetic particle imaging. *International Journal on Magnetic Particle Imaging*, 6(2):1–3, 2020. inproceedings, multi-patch, artifact.

[9] M. Boberg, T. Knopp, P. Szwargulski, and M. Möddel. Generalized MPI multi-patch reconstruction using clusters of similar system matrices. *IEEE Transactions on Medical Imaging*, 39(5):1347–1358, May 2020. article, multi-patch, artifact.

[10] J. Bohnert and O. Dössel. Calculation and evaluation of current densities and thermal heating in the body during MPI. In *Magnetic Nanoparticles: Particle Science, Imaging Technology, and Clinical Applications*, pages 162–168. World Scientific, 2010.

[11] C. Brandt and C. Schmidt. Modeling magnetic particle imaging for dynamic tracer distributions. *Sensing and Imaging*, 22(45), Nov. 2021.

[12] C. Brandt and C. Schmidt. Motion compensation for non-periodic dynamic tracer distributions in multi-patch magnetic particle imaging. *Physics in Medicine & Biology*, 67(8):085005, Apr. 2022.

[13] G. Bringout and T. Buzug. A robust and compact representation for magnetic fields in magnetic particle imaging. *Biomed Tech*, 59:978–1, 2014.

[14] G. Bringout, W. Erb, and J. Frikel. A new 3D model for magnetic particle imaging using realistic magnetic field topologies for algebraic reconstruction. *Inverse Problems*, 36(12):124002, 2020.

[15] T. A. Bubba, M. März, Z. Purisha, M. Lassas, and S. Siltanen. Shearlet-based regularization in sparse dynamic tomography. In *Wavelets and Sparsity XVII*, volume 10394, page 103940Y. International Society for Optics and Photonics, 2017.

[16] M. Burger, H. Dirks, L. Frerking, A. Hauptmann, T. Helin, and S. Siltanen. A variational reconstruction method for undersampled dynamic x-ray tomo-

graphy based on physical motion models. *Inverse Problems*, 33(12):124008, 2017.

[17] T. Buzug. *Computed Tomography: From Photon Statistics to Modern Cone-Beam CT*. Springer, 2008.

[18] Q. Ding, M. Burger, and X. Zhang. Dynamic SPECT reconstruction with temporal edge correlation. *Inverse Problems*, 34(1):014005, 2017.

[19] S. Dittmer, T. Kluth, M. T. R. Henriksen, and P. Maaß. Deep image prior for 3D magnetic particle imaging: A quantitative comparison of regularization techniques on Open MPI dataset. *arXiv preprint arXiv:2007.01593*, 2020.

[20] C. Droigk, M. Maass, and A. Mertins. Direct multi-dimensional chebyshev polynomial based reconstruction for magnetic particle imaging. *Physics in Medicine & Biology*, 2022.

[21] EB. Resovist. Deutsches Ärtzeblatt, Jan. 2002.

[22] D. Eberbeck, C. L. Dennis, N. F. Huls, K. L. Krycka, C. Gruttner, and F. Westphal. Multicore magnetic nanoparticles for magnetic particle imaging. *IEEE Transactions on Magnetics*, 49(1):269–274, 2012.

[23] J. Ehrhardt, M. Ahlborg, H. Uzunova, T. M. Buzug, and H. Handels. Temporal polyrigid registration for patch-based MPI reconstruction of moving objects. *International Journal on Magnetic Particle Imaging*, 5(1-2), 2019.

[24] A. Fasano and A. Sequeira. *Hemomath: The mathematics of blood*, volume 18. Springer, 2017.

[25] N. Gdaniec, M. Boberg, M. Möddel, P. Szwargulski, and T. Knopp. Suppression of motion artifacts caused by temporally recurring tracer distributions in multi-patch magnetic particle imaging. *IEEE Transactions on Medical Imaging*, 39(11):3548–3558, November 2020.

[26] N. Gdaniec, M. Schlüter, M. Hofmann, M. Kaul, K. Krishnan, A. Schlafer, and T. Knopp. Detection and compensation of periodic motion in magnetic particle imaging. *IEEE Transactions on Medical Imaging*, 2017.

[27] C. Geiger and C. Kanzow. *Numerische Verfahren zur Lösung unrestringierter Optimierungsaufgaben*. Springer, 1 edition, 1999.

[28] B. Gleich and J. Weizenecker. Tomographic imaging using the nonlinear response of magnetic particles. *Nature*, 435(7046):1214–1217, 2005.

[29] B. Gleich, J. Weizenecker, H. Timminger, C. Bontus, I. Schmale, J. Rahmer, J. Schmidt, J. Kanzenbach, and J. Borgert. Fast MPI demonstrator with enlarged field of view. In *Proc. ISMRM*, number 218, 2010.

[30] P. W. Goodwill and S. M. Conolly. The X-space formulation of the magnetic particle imaging process: 1-D signal, resolution, bandwidth, SNR, SAR, and magnetostimulation. *IEEE Transactions on Medical Imaging*, 29(11):1851–1859, 2010.

[31] P. W. Goodwill and S. M. Conolly. Multidimensional x-space magnetic particle imaging. *IEEE Transactions on Medical Imaging*, 30(9):1581–1590, 2011.

[32] M. Gräser, F. Thieben, P. Szwargulski, F. Werner, N. Gdaniec, M. Boberg, F. Griese, M. Möddel, P. Ludewig, D. van de Ven, et al. Human-sized magnetic particle imaging for brain applications. *Nature communications*, 10(1):1–9, 2019.

[33] E. Gravier, Y. Yang, and M. Jin. Tomographic reconstruction of dynamic cardiac image sequences. *IEEE Transactions on Image Processing*, 16(4):932–942, 2007.

[34] M. Grüttner, T. Knopp, J. Franke, M. Heidenreich, J. Rahmer, A. Halkola, C. Kaethner, J. Borgert, and T. M. Buzug. On the formulation of the image reconstruction problem in magnetic particle imaging. *Biomedical Engineering/Biomedizinische Technik*, 58(6):583–591, 2013.

[35] J. Hadamard. *Lectures on Cauchy's problem in linear partial differential equations*. Yale University Press, 1932.

[36] J. Haegele, N. Panagiotopoulos, S. Cremers, J. Rahmer, J. Franke, R. L. Duschka, S. Vaalma, M. Heidenreich, J. Borgert, P. Borm, et al. Magnetic particle imaging: A resovist based marking technology for guide wires and catheters for vascular interventions. *IEEE transactions on medical imaging*, 35(10):2312–2318, 2016.

[37] J. Haegele, J. Rahmer, B. Gleich, J. Borgert, H. Wojtczyk, N. Panagiotopoulos, T. M. Buzug, J. Barkhausen, and F. M. Vogt. Magnetic particle imaging: visualization of instruments for cardiovascular intervention. *Radiology*, 265(3):933–938, 2012.

[38] B. N. Hahn. Motion estimation and compensation strategies in dynamic computerized tomography. *Sensing and Imaging*, 18(1):10, 2017.

[39] A. Hauptmann, O. Öktem, and C. Schönlieb. Image reconstruction in dynamic inverse problems with temporal models. In *Handbook of Mathematical Models and Algorithms in Computer Vision and Imaging: Mathematical Imaging and Vision*, pages 1–31. Springer, 2021.

[40] K. Höllig and J. Hörner. *Approximation and modeling with B-splines*. SIAM, 2013.

[41] S. Ilbey, C. B. Top, T. Çukur, E. U. Saritas, and H. E. Güven. Image reconstruction for magnetic particle imaging using an augmented lagrangian method. In *2017 IEEE 14th International Symposium on Biomedical Imaging (ISBI 2017)*, pages 64–67. IEEE, 2017.

[42] S. Kaczmarz. Angenäherte Auflösung von Systemen linearer Gleichungen. *Bull. Int. Acad. Pol. Sci. Lett. Class. Sci. Math. Nat*, pages 355–7, 1937.

[43] M. G. Kaul, J. Salamon, T. Knopp, H. Ittrich, G. Adam, H. Weller, and C. Jung. Magnetic particle imaging for in vivo blood flow velocity measurements in mice. *Physics in Medicine & Biology*, 63(6):064001, 2018.

[44] T. Kluth. Mathematical models for magnetic particle imaging. *Inverse Problems*, 34(8):083001, 2018.

[45] T. Kluth and B. Jin. L1 data fitting for robust reconstruction in magnetic particle imaging: quantitative evaluation on open MPI dataset. *International Journal on Magnetic Particle Imaging*, 6, 2020.

[46] T. Kluth, B. Jin, and G. Li. On the degree of ill-posedness of multi-dimensional magnetic particle imaging. *Inverse Problems*, 34(9):095006, July 2018.

[47] T. Kluth, P. Szwargulski, and T. Knopp. Towards accurate modeling of the multidimensional MPI physics. *International Journal on Magnetic Particle Imaging*, 6(2):1–3, 2020.

[48] T. Knopp and T. Buzug. *Magnetic Particle Imaging: An Introduction to Imaging Principles and Scanner Instrumentation*. Springer Berlin Heidelberg, 2012.

[49] T. Knopp, N. Gdaniec, and M. Möddel. Magnetic particle imaging: from proof of principle to preclinical applications. *Physics in Medicine & Biology*, 62(14):R124–R178, June 2017.

[50] T. Knopp, J. Rahmer, T. F. Sattel, S. Biederer, J. Weizenecker, B. Gleich, J. Borgert, and T. M. Buzug. Weighted iterative reconstruction for magnetic particle imaging. *Physics in Medicine & Biology*, 55(6):1577, 2010.

[51] T. Knopp, T. F. Sattel, S. Biederer, J. Rahmer, J. Weizenecker, B. Gleich, J. Borgert, and T. M. Buzug. Model-based reconstruction for magnetic particle imaging. *IEEE Transactions on Medical Imaging*, 29(1):12–18, 2009.

[52] T. Knopp, P. Szwargulski, F. Griese, and M. Gräser. OpenMPIData: An initiative for freely accessible magnetic particle imaging data. *Data in Brief*, 28:104971, 2020.

[53] T. Knopp, K. Them, M. Kaul, and N. Gdaniec. Joint reconstruction of non-overlapping magnetic particle imaging focus-field data. *Physics in Medicine & Biology*, 60(8):L15, 2015.

[54] F. Lieb and T. Knopp. A sparse row-action algorithm for magnetic particle imaging. *International Journal on Magnetic Particle Imaging*, 6(2 Suppl 1), 2020.

[55] P. Ludewig, N. Gdaniec, J. Sedlacik, N. D. Forkert, P. Szwargulski, M. Graeser, G. Adam, M. G. Kaul, K. M. Krishnan, R. M. Ferguson, et al. Magnetic particle imaging for real-time perfusion imaging in acute stroke. *ACS nano*, 11(10):10480–10488, 2017.

[56] M. Maass, C. Droigk, F. Katzberg, P. Koch, and A. Mertins. A recovery algorithm based on the kaczmarz algorithm and admm splitting with application to convex optimization in magnetic particle imaging. In *2020 28th European Signal Processing Conference (EUSIPCO)*, pages 2135–2139. IEEE, 2021.

[57] T. März and A. Weinmann. Model-based reconstruction for magnetic particle imaging in 2D and 3D. *Inverse Problems & Imaging*, 10(4):1087–1110, 2016.

[58] OpenMPIData. magneticparticleimaging.github.io/openmpidata.jl/latest/index.html. CC BY 4.0.

[59] A. A. Petryk, A. J. Giustini, R. E. Gottesman, B. S. Trembly, and P. J. Hoopes. Comparison of magnetic nanoparticle and microwave hyperthermia cancer treatment methodology and treatment effect in a rodent breast cancer model. *International Journal of Hyperthermia*, 29(8):819–827, 2013.

[60] J. Rahmer, B. Gleich, C. Bontus, J. Schmidt, I. Schmale, J. Borgert, O. Woywode, A. Halkola, and T. M. Buzug. Automated derivation of sub-volume system functions for 3D MPI with fast continuous focus field variation. In *International Workshop on Magnetic Particle Imaging*, page 97, 2014.

[61] J. Rahmer, B. Gleich, J. Weizenecker, A. Halkola, C. Bontus, J. Schmidt, I. Schmale, O. Woywode, T. Buzug, and J. Borgert. Fast continuous motion of the field of view in magnetic particle imaging. In *International Workshop on Magnetic Particle Imaging*, pages 1–1. IEEE, 2013.

[62] J. Rahmer, C. Stehning, and B. Gleich. Remote magnetic actuation using a clinical scale system. *PloS one*, 13(3):e0193546, 2018.

[63] J. Rahmer, J. Weizenecker, B. Gleich, and J. Borgert. Analysis of a 3-D system function measured for magnetic particle imaging. *IEEE Transactions on Medical Imaging*, 31(6):1289–1299, 2012.

[64] J. Rahmer, D. Wirtz, C. Bontus, J. Borgert, and B. Gleich. Interactive magnetic catheter steering with 3-D real-time feedback using multi-color magnetic particle imaging. *IEEE transactions on medical imaging*, 36(7):1449–1456, 2017.

[65] Rama. Laboratory mouse. CC BY-SA 2.0 FR. Wikimedia.

[66] A. Rieder. *Keine Probleme mit inversen Problemen: Eine Einführung in ihre stabile Lösung*. Vieweg+Teubner Verlag, 2003.

[67] E. U. Saritas, P. W. Goodwill, G. Z. Zhang, and S. M. Conolly. Magnetostimulation limits in magnetic particle imaging. *IEEE Transactions on Medical Imaging*, 32(9):1600–1610, 2013.

[68] I. Schmale, B. Gleich, J. Rahmer, C. Bontus, J. Schmidt, and J. Borgert. MPI safety in the view of MRI safety standards. *IEEE Transactions on Magnetics*, 51(2):1–4, 2015.

[69] U. Schmitt and A. Louis. Efficient algorithms for the regularization of dynamic inverse problems: I. theory. *Inverse Problems*, 18(3):645, 2002.

[70] U. Schmitt, A. K. Louis, C. Wolters, and M. Vauhkonen. Efficient algorithms for the regularization of dynamic inverse problems: Ii. applications. *Inverse Problems*, 18(3):659, 2002.

[71] M. Schubert. Superparamagnetische Flüssigkeit. CC BY-SA 3.0 DE. Wikimedia.

[72] T. Schuster, B. Hahn, and M. Burger. Dynamic inverse problems: modelling—regularization—numerics. *Inverse Problems*, 34(4):040301, 2018.

[73] J. Sedlacik, A. Frölich, J. Spallek, N. D. Forkert, T. D. Faizy, F. Werner, T. Knopp, D. Krause, J. Fiehler, and J.-H. Buhk. Magnetic particle imaging for high temporal resolution assessment of aneurysm hemodynamics. *PloS one*, 11(8):e0160097, 2016.

[74] Statistisches Bundesamt (Destatis). 23141 Fallpauschalenbezogene Krankenhausstatistik (DRG). www.govdata.de/dl-de/by-2-0, 2022. 2022-02-27 11:53:19.

[75] Statistisches Bundesamt (Destatis). Gestorbene: Deutschland, Jahre, Todesursachen, Geschlecht, 2020. www.govdata.de/dl-de/by-2-0, 2022. 2022-02-28 15:21:50.

[76] M. Storath, C. Brandt, M. Hofmann, T. Knopp, J. Salamon, A. Weber, and A. Weinmann. Edge preserving and noise reducing reconstruction for magnetic particle imaging. *IEEE Transactions on Medical Imaging*, 36(1):74–85, 2017.

[77] T. Strohmer and R. Vershynin. A randomized kaczmarz algorithm with exponential convergence. *Journal of Fourier Analysis and Applications*, 15(2):262–278, 2009.

[78] P. Szwargulski, N. Gdaniec, M. Graeser, M. Möddel, F. Griese, K. M. Krishnan, T. M. Buzug, and T. Knopp. Moving table magnetic particle imaging: a stepwise approach preserving high spatio-temporal resolution. *Journal of Medical Imaging*, 5(4):046002, 2018.

[79] P. Szwargulski, N. Gdaniec, M. Möddel, M. Graeser, and T. Knopp. Reconstruction of an object moved continuously through the field of view in MPI. In *International Workshop on Magnetic Particle Imaging*, pages 137–138, 2018.

[80] P. Szwargulski and T. Knopp. Determination of 3D system matrices using a mirroring approach based on mixing theory. *International Journal on Magnetic Particle Imaging*, 6(2):1–3, 2020.

[81] P. Szwargulski, M. Möddel, N. Gdaniec, and T. Knopp. Efficient joint image reconstruction of multi-patch data reusing a single system matrix in magnetic particle imaging. *IEEE Transactions on Medical Imaging*, 38(4):932–944, 2018.

[82] A. Tomitaka, H. Arami, S. Gandhi, and K. M. Krishnan. Lactoferrin conjugated iron oxide nanoparticles for targeting brain glioma cells in magnetic particle imaging. *Nanoscale*, 7(40):16890–16898, 2015.

[83] S. Vaalma, J. Rahmer, N. Panagiotopoulos, R. L. Duschka, J. Borgert, J. Barkhausen, F. M. Vogt, and J. Haegele. Magnetic particle imaging (MPI): Experimental quantification of vascular stenosis using stationary stenosis phantoms. *PloS one*, 12(1):e0168902, 2017.

[84] A. Weber, F. Werner, J. Weizenecker, T. M. Buzug, and T. Knopp. Artifact free reconstruction with the system matrix approach by overscanning the field-free-point trajectory in magnetic particle imaging. *Physics in Medicine & Biology*, 61(2):475, 2015.

[85] J. Weizenecker. The Fokker–Planck equation for coupled Brown–Néel-rotation. *Physics in Medicine & Biology*, 63(3):035004, 2018.

[86] J. Weizenecker, J. Borgert, and B. Gleich. A simulation study on the resolution and sensitivity of magnetic particle imaging. *Physics in Medicine & Biology*, 52(21):6363, 2007.

[87] J. Weizenecker, B. Gleich, J. Rahmer, H. Dahnke, and J. Borgert. Three-dimensional real-time in vivo magnetic particle imaging. *Physics in Medicine & Biology*, 54(5):L1, 2009.

[88] E. Y. Yu, P. Chandrasekharan, R. Berzon, Z. W. Tay, X. Y. Zhou, A. P. Khandhar, R. M. Ferguson, S. J. Kemp, B. Zheng, P. W. Goodwill, et al. Magnetic particle imaging for highly sensitive, quantitative, and safe in vivo gut bleed detection in a murine model. *ACS nano*, 11(12):12067–12076, 2017.

[89] L. Zdun and C. Brandt. Fast MPI reconstruction with non-smooth priors by stochastic optimization and data-driven splitting. *Physics in Medicine & Biology*, 66(17):175004, 2021.

Glossary

Abbreviations

ART	Algebraic reconstruction technique
CT	Computed tomography
DF FOV	Drive field field-of-view
FFL	Field-free line
FFP	Field-free point
FOV	Field-of-view
FWHM	Full-width-at-half-maximum
MNP	Magnetic nano particles
MPI	Magnetic particle imaging
MRI	Magnetic resonance imaging
MSE	Mean squared error
PET	Positron emission tomography
PNS	Peripheral nerve stimulation
SM FOV	System matrix field-of-view
SNR	Signal-to-noise ratio
SPECT	Single-photon emission computed tomography
SPION	Superparamagnetic iron oxide nanoparticle
TUHH	Hamburg University of Technology
UKE	University Medical Center Hamburg-Eppendorf

Mathematical Symbols

$*$	Convolution
$\mathrm{dom}(\cdot)$	Domain
$\hat{\cdot}$	Variable in Fourier space
$\mathcal{F}$	Fourier transform

$\mathcal{O}$	Big O notation
$\odot$	Element-wise multiplication
$\mathrm{ran}(\cdot)$	Range
A^+	Moore-Penrose inverse
A^*	Adjoint operator of $A : X \to Y$ with $\langle Ax, y\rangle_Y = \langle x, A^*y\rangle_X$
H^1	Sobolev space

Spline Parameters

Λ_B	Set of all coefficients
$\mathbb{S}_{d,\mathbf{t}}$	Spline space of B-splines with knot vector $\mathbf{t}$ and degree d
$\mathbf{t}$	Knot vector
B	B-Spline with known degree and knot vector
b	Spline coefficient
$B^d_{m,\mathbf{t}}$	B-spline with degree d, knot vector $\mathbf{t}$ and support on knot interval $[\tau_m, \tau_{m+1})$
d	Degree of a B-spline
M_0	Number of equally distributed knots within the scan time of a patch per frame
M_p	Set of indices determining the B-splines and coefficients belonging to patch p

Functions, Variables and Parameters

α	Parameter for the Langevin function
$\bar{m}$	Mean magnetic moment
β	Parameter for the Langevin function
Δ_f	Shifting time to move the focus field
$\dot{c}$	Time derivative of the concentration, $\partial c/\partial t$
η	Summary of constants, $-\mu_0 p_s \in \mathbb{R}$
γ	Regularization parameter
$\hat{u}$	Measured voltage in frequency domain
$\mathbf{D}_c$	Discrete version of $\partial c/\partial t$
$\mathcal{L}$	Langevin function

$\mathcal{R}$	Regularization functional
μ_0	Permeability constant
a_k	Bandstop filter
c	Tracer concentration
H	Magnetic field
H_D	Drive field
H_S	Selection field
k_B	Boltzmann constant
l	Repetitions per patch
M	Magnetization function
M_c	Saturation magnetization of the core material
n_c	Number of channels respectively the dimension of the magnetic field
n_K	Number of frequencies
n_T	Number of time points within one repetition time
P	Number of patches
p_s	Coil sensitivity
R	Number of voxels
S_1	System function 1 or system matrix 1, $\partial\bar{m}/\partial t$
S_2	System function 1 or system matrix 2, $\bar{m}$
T	Total scanning time, FT_F
T_0	Temperature
T_c	Repetition time of the (Lissajous) trajectory
T_F	Time period for the scan of one frame, PT_P
T_P	Time period for the scan of one patch, $lT_c + \Delta_f$
u	Measured voltage in time domain
V_c	Volume of the particle core

List of Figures

List of Tables

A. Proofs

This section lists some proofs of statements in Chapter 2.

Proof of Theorem 2.3. We proof the equivalence with a circular argument.
1) → 2) Assuming there exists a $\varphi \in X$ with $\|Ax - y\|_Y > \|A\varphi - y\|_Y$,

$$\begin{aligned} \|Ax - y\|_Y &> \|A\varphi - y\|_Y \\ \|P_{\overline{\operatorname{ran}(A)}} y - y\|_Y &> \|A\varphi - y\|_Y \\ \min_{u \in \overline{\operatorname{ran}(A)}} \|u - y\|_Y &> \|A\varphi - y\|_Y \\ \Rightarrow A\varphi &\notin \overline{\operatorname{ran}(A)} \end{aligned}$$

which is a contradiction.
2) → 3) Defining the quadratic function $F(\lambda) = \|A(x + \lambda\varphi) - y\|_Y^2$, we consider its derivative

$$F'(\lambda) = 2\lambda\langle A\varphi, Ax\rangle_Y + 2\langle A\varphi, Ax\rangle_Y - 2\langle A\varphi, y\rangle_Y$$

for $\lambda = 0$

$$\begin{aligned} F'(0) &= 2\langle Ax, A\varphi\rangle_Y - 2\langle y, A\varphi\rangle_Y = 0 \\ &\Leftrightarrow \langle A^*Ax, \varphi\rangle_Y - \langle A^*y, A\varphi\rangle_Y = 0 \\ &\Leftrightarrow \langle A^*Ax - A^*y, \varphi\rangle_Y = 0, \qquad \text{for all } \varphi \in X \\ &\Leftrightarrow A^*Ax = A^*y. \end{aligned}$$

3) → 1) In order find the space which contains $Ax - y$, we first consider the

normal equation

$$\begin{aligned} A^*Ax &= A^*y \\ A^*(Ax-y) &= 0 \qquad \Rightarrow Ax-y \in \mathcal{N}(A^*) \\ \langle A^*(Ax-y), \varphi\rangle_X &= 0 \\ \langle Ax-y, A\varphi\rangle_X &= 0 \qquad \text{for all } \varphi \in X \Rightarrow Ax-y \in \operatorname{ran}(A)^\perp. \end{aligned}$$

In a second step we consider the projection. For $y \in Y$ and an orthogonal projection on $\overline{\operatorname{ran}(A)}$ holds

$$\begin{aligned} \|P_{\overline{\operatorname{ran}(A)}}y - y\|_Y &= \operatorname*{arg\,min}_{u\in\overline{\operatorname{ran}(A)}} \|u-y\|_Y \\ &= \operatorname*{arg\,min}_{u\in\overline{\operatorname{ran}(A)}} \left\{ \frac{1}{2}\langle u,u\rangle_Y - \langle y,u\rangle_Y \right\} \end{aligned}$$

which corresponds to solving

$$\begin{aligned} \langle u,w\rangle_Y &= \langle y,w\rangle_Y \qquad w \in \overline{\operatorname{ran}(A)} \\ \langle u-y,w\rangle_Y &= 0 \\ \Leftrightarrow u-y &\in \overline{\operatorname{ran}(A)}^\perp. \end{aligned}$$

This yields

$$Ax = P_{\overline{\operatorname{ran}(A)}}y \Leftrightarrow Ax \in \overline{\operatorname{ran}(A)} \text{ and } Ax-y \in \overline{\operatorname{ran}(A)}^\perp$$

which is fulfilled, as we showed in the first step. □

We provide a Theorem on the properties of the Tikhonov functional.

Theorem A.1. *Let continuous linear maps $A : X \mapsto Y$, $B : X \mapsto Z$, $y \in Y$ and $\gamma \geq 0$. For $x_\gamma \in X$ the following two statements are equivalent:*

1. *x_γ is a solution of the regularized normal equation:*

$$(A^*A + \gamma B^*B)x_\gamma = A^*y \tag{A.1}$$

2. *x_γ minimizes the Tikhonov functional, i.e.*

$$x_\gamma = \arg\min_{x \in X} J_{\gamma,y}(x)\,. \tag{A.2}$$

Proof. Consider the function $F : \mathbb{R} \to \mathbb{R}$,

$$F(t) := J_{\gamma,y}(x_\gamma + tv)\,. \tag{A.3}$$

Then,

$$F(t) = J_{\gamma,y}(x_\gamma) + 2t\,\langle A^*\,(Ax_\gamma - y) + \gamma B^*Bx_\gamma | v\rangle_X + t^2\|Av\|_Y^2 + t^2\gamma\|Bv\|_Z^2\,. \tag{A.4}$$

2) → 1) Let x_γ be a minimizer of the Tikhonov functional $J_{\gamma,y}$. Thus, the directional derivative $\nabla J_{\gamma,y}(x_\gamma)v$ must vanish in every direction v:

$$\begin{aligned}\frac{\mathrm{d}}{\mathrm{d}t}F(t)\bigg|_{t=0} &= \lim_{t\to 0}\frac{F(t)-F(0)}{t}\\ &= 2\langle A^*\,(Ax_\gamma - y) + \gamma B^*Bx_\gamma | v\rangle_X\\ &= 2\left\langle \underbrace{(A^*A + \gamma B^*B)x_\gamma - A^*y}_{\nabla J_{\gamma,y}(x_\gamma)} | v \right\rangle_X\end{aligned}$$

and thus

$$0 \overset{!}{=} 2\,\langle (A^*A + \gamma B^*B)x_\gamma - A^*y | v\rangle_X \qquad \forall v \in X\,.$$

This yields

$$\|(A^*A + \gamma B^*B)x_\gamma - A^*y\|_X^2 = 0\,,$$

which implies that x_γ is a solution of the regularized normal equation

$$(A^*A + \gamma B^*B)x_\gamma = A^*y\,.$$

1)→ 2) Assuming that x_γ is a solution of the regularized normal equation. Let $w \in X$ which can be written as $w = x_\gamma + tv$ with $v = w - x_\gamma$ and $t = 1$. We obtain

$$\begin{aligned} J_{\gamma,y}(w) &= J_{\gamma,y}(x_\gamma + v) \overset{(A.3)}{=} F(1) \\ &\overset{(A.4)}{=} J_{\gamma,y}(x_\gamma) + 2\langle \underbrace{A^*Ax_\gamma + \gamma B^*Bx_\gamma - A^*y}_{=0} | v\rangle_X + \|Av\|Y^2 + \gamma\|Bv\|Z^2 \\ &= J_{\gamma,y}(x_\gamma) + \|Av\|Y^2 + \gamma\|Bv\|Z^2 \\ &\geq J_{\gamma,y}(x_\gamma)\,. \end{aligned}$$

This implies that x_γ minimizes the Tikhonov functional. □

B. Simulation Parameters

In this section we list all parameters used for the simulations in Sections 4.3, 6.1 and 6.2.

Table B.1.: Physical constants and parameters for a simulated MPI scanner

Parameter		**Value**	**cf.**
Constants			
Permeability constant	μ_0	$4\pi \cdot 10^{-7}$ N/A^2	
Boltzmann constant	k_B	$1.38064852 \cdot 10^{-23}$ J/K	
Particles			
Temperature	T_0	310 K	[51]
Saturation magnetization	M_c	$\frac{0.6}{\mu_0}$ T	[51]
Particle core diameter	D	$20 \cdot 10^{-9}$ m	[22]
Particle core volume	V_c	$\frac{1}{6}\pi D^3$ m^3	[51]
Particle magnetic moment	α	$M_C V_C$ Am^2	[51]
Parameter of Langevin function	β	$(k_B T)^{-1}$ N^{-1}m^{-1}	[51]
Scanner			[52]
Excitation frequencies	$[f_x, f_y, f_z]$	$[2.5/102, 2.5/96, 2.5/99]$ MHz	
Excitation amplitudes	$[a_x, a_y, a_z]$	$[12, 12, 0]$ mT	
Excitation phase shifts	$[\varphi_x, \varphi_y, \varphi_z]$	$[\frac{\pi}{2}, \frac{\pi}{2}, \frac{\pi}{2}]$	
Gradient strengths	$[g_x, g_y, g_z]$	$[-1, -1, 2]$ T/m	
Excitation repetition time	T_c	$652.8 \cdot 10^{-6}$ s	

Table B.2.: Simulation parameters for the one-peak and three-peak phantom from Section 6.1

Parameter		**Value**
Number of voxels		$3 \times 3 \times 1$
Voxel size [mm^3]		$10.7 \times 10.7 \times 10.7$
FOV size [mm^3]		$32.0 \times 32.0 \times 10.7$
Time sampling per cycle	n_T	408
Transition time between frames [s]	Δ_f	0
Number of frames for the one-peak phantom	F	4
Number of frames for the three-peak phantom	F	10

Table B.3.: Simulation parameters for the dynamic single and multi-patch phantom from Section 6.2

	Single-patch	**Multi-patch**	
Parameter	**Value**	**Value (patch)**	**Value (total)**
Measurement			
Number of voxels	$12 \times 12 \times 1$	$16 \times 16 \times 1$	$16 \times 32 \times 1$
Voxel size [mm^3]	$2 \times 2 \times 1$	$1.5 \times 1.5 \times 0.75$	
FOV size [mm^3]	$24 \times 24 \times 1$	$24 \times 24 \times 0.75$	$24 \times 48 \times 0.75$
Reconstruction			
Number of voxels	$10 \times 10 \times 1$	$12 \times 12 \times 1$	$12 \times 24 \times 1$
Voxel size [mm^3]	$2.4 \times 2.4 \times 1$	$2 \times 2 \times 0.75$	
FOV size [mm^3]	$24 \times 24 \times 1$	$24 \times 24 \times 0.75$	$24 \times 48 \times 0.75$

Publications derived from this dissertation

Parts of the results of this thesis have been published in

C.Schmidt and C.Brandt. Dynamic concentration reconstruction for magnetic particle imaging using splines. *International Journal on Magnetic Particle Imaging* (2020)

C.Brandt and C.Schmidt. Modeling Magnetic Particle Imaging for Dynamic Tracer Distributions. *Sensing and Imaging* (2021)

C.Brandt and C.Schmidt. Motion Compensation for Non-Periodic Dynamic Tracer Distributions in Multi-Patch Magnetic Particle Imaging. *Physics in Medicine & Biology* (2022).

Eidesstattliche Versicherung / Declaration on oath

Hiermit erkläre ich an Eides statt, dass ich die vorliegende Dissertationsschrift selbst verfasst und keine anderen als die angegebenen Quellen und Hilfsmittel benutzt habe.

I hereby declare upon oath that I have written the present dissertation independently and have not used further resources and aids than those stated.

Ort, Datum | *city, date*

Unterschrift | *signature*

Erklärung zum Eigenanteil bei der Zusammenarbeit

Teile der Kapitel 4.2, 4.3, 6.1.1 sowie die rauschfreien Experimente in Kapitel 6.1.3 basieren auf [11]. Ich habe die erste Fassung von [11] verfasst und war zu großen Teilen an der Idee und deren Umsetzung beteiligt. Darüber hinaus habe ich die Beispiele und Experimente konzipiert und umgesetzt. Darüber hinaus war ich hauptsächlich für die Darstellung und Auswertung der Ergebnisse verantwortlich. Die Anmerkungen von C.Brandt und den Gutachtern des Journals wurden von mir umgesetzt.
Die Modelle in Kapitel 4.2, Teile von Kapitel 4, das Konzept der Experimente in Kapitel 6.2.1 und die Experimente und Ergebnisse in Kapitel 6.2.2 basieren auf [12]. Ich habe die erste Fassung des Textes verfasst und war zu großen Teilen an der Idee und deren Umsetzung beteiligt. Auch die Konzeption und Durchführung der Experimente wurde von mir übernommen. Darüber hinaus war ich hauptsächlich für die Darstellung und Auswertung der Ergebnisse verantwortlich. Die Anmerkungen von C.Brandt und den Gutachtern des Journals wurden von mir umgesetzt.

Ort, Datum | *city, date*

Unterschrift | *signature*